UNIVERSITY OF CAPE TOWN

CONDITION MONITORING OF POLYMER ELECTROLYTE MEMBRANE FUEL CELLS

A Thesis

By

CHRIS DE BEER

Department of Electrical Engineering

Submitted in fulfilment of the requirements

for the degree of

DOCTOR OF PHILOSOPHY

(Electrical Engineering)

University of Cape Town

August 2014

Accepted by the Doctoral Degrees Board

The copyright of this thesis vests in the author. No quotation from it or information derived from it is to be published without full acknowledgement of the source. The thesis is to be used for private study or non-commercial research purposes only.

Published by the University of Cape Town (UCT) in terms of the non-exclusive license granted to UCT by the author.

University of Cape Town

Declaration

This dissertation is submitted to the Department of Electrical Engineering, University of Cape Town, in complete fulfilment of the requirements for the degree of Doctor of Philosophy. It has not been submitted before for any degree or examination at this or any other university. The author confirms that this thesis is based on his own work. Portions of this work have been published in peer reviewed journals and at refereed international conferences.

Acknowledgements

This project would not have been possible without the help and support I received from family, friends and colleagues throughout the course of my research.

To my primary supervisor, Dr. Paul Barendse, I would like to express my utmost gratitude for his endless patience and willingness to make time for our discussions despite his own commitments towards his family and work.

My sincere thanks to my co-supervisor, Prof. Pragasen Pillay for the support, guidance and encouragement he provided.

I would like to thank the researchers from the USA, Dr. Brian Bullecks and Prof. Raghunathan Rengaswamy for their valuable input and expertise. To the research team at HySA Catalysis, I would like to express my most sincere thanks for their assistance.

To my friends and colleagues in the AMES research group at the University of Cape Town I would like to express my gratitude for their support. I am grateful to Mr. Chris Wozniak and Mr. Phillip Titus for their technical assistance.

I would like to thank my family, especially my parents Johan and Maritha de Beer for their endless love and patience with my graduate studies. Lastly, I would like to thank my grandparents, who always believed in me. This thesis is dedicated to them.

"I don't know anything, but I do know that everything is interesting if you go into it deeply enough" - Richard Feynman, Nobel Prize 1965.

Abstract

Condition Monitoring of Polymer Electrolyte Membrane Fuel Cells

by

Chris de Beer

As the global demand for energy continues to grow new technologies and systems must be developed to supply the market. This includes renewable energy generation, storage and conversion systems. The primary storage technology in use today in the portable electronics, the automotive sector and to a lesser extent power networks is battery based systems. To overcome some of the limitations inherent in batteries, fuel cell based power generators and converters have been developed. Fuel cells act as electrochemical energy converters that convert a fuel source such as natural gas directly into electrical power without any secondary phases. For systems running on Hydrogen generated via renewable or natural sources, the input/output cycle becomes completely sustainable. Out of the different fuel cell types available and under development, the Proton Exchange Membrane or Polymer Electrolyte Membrane (PEM) fuel cell has emerged as the technology of choice, and currently owns more than 80% of the commercial fuel cell market. This has spurred further research in the field to increase performance and life expectancy of the cell materials. A promising development in the form of High Temperature PEM (HT-PEM) fuel cells has recently emerged and addresses some of the shortcomings of the low temperature counterparts.

A critical field of research is the condition monitoring strategies and technologies for the electrochemical device that ties in with the power conditioning sub-systems. This thesis presents the development of condition monitoring systems by conducting detailed studies on the fault/degradation mechanisms prevalent in the cell materials for the purpose of detection, classification and implementation of possible mitigation strategies. Specific consideration is given to the detailed analysis of the fault mechanisms in HT-PEM fuel cells that are not yet fully understood and commercialized. In particular, electrochemical equivalent circuit models and reduced order semi-empirical models are developed to facilitate fault detection. Based on these models, mitigation strategies for specific faults are proposed and experimentally verified. New systems and methods are developed for rapid online impedance signature mapping that provide a basis for early fault prediction that can increase system performance and life expectancy.

The findings in this research provide valuable insight into the effect that most prevalent faults have on the internal electrochemistry and the impact on electrical performance. From the experimental results, a semi-empirical electrochemical model is developed to assist with life time estimation and system optimization. The model is integrated with a real time emulator platform that can reproduce single cell

voltage levels at the high output currents and transient characteristics. A detailed analysis is conducted on CO poisoning and the resulting effects on key equivalent circuit parameters that enable quantification of the fault condition. It is shown that the catalyst at the higher operating temperature is still susceptible to a certain degree of semi-permanent degradation. To mitigate these effects, a new active current control strategy is proposed to enforce electro-oxidation of the CO to recover the lost active area that delivered superior results compared to current pulsing strategies.

New rapid online detection strategies are proposed by using small voltage transients in an operational HT-PEM fuel cell. The method makes use of the discrete S-transform that overcomes some of the limits in other signal processing methods used in fuel cell diagnostics. To enable detailed parameter calculation, a population based incremental learning algorithm is implemented in the developed method. A new condition monitoring system is developed that makes use of Optimized Broadband Impedance Spectroscopy. The hardware is designed to accommodate both single cell and stack level implementation. It is shown that the proposed system is able to deliver measurements under extreme non-linear conditions that can occur in PEM fuel cells in a fraction of the time associated with normal EIS based systems.

Contents

List of Tables

List of Figures

Chapter 1

Introduction

1.1 Overview

This thesis evaluates the different degradation and fault mechanisms of PEM fuel cells for the purpose of developing rapid online detection systems and mitigation strategies to increase performance and life expectancy. Various electrochemical diagnostic methodologies and advanced signal processing techniques are implemented to isolate the markers for each fault mechanism. These markers are used to develop models for the fuel cell and possible fault conditions. The developed models are integrated with real time emulator systems that replicate possible fault scenarios in order to optimize system performance.

To realize early fault detection, new systems and methodologies are developed that produce detailed information on key parameters identified during the course of this investigation. The power electronic hardware implemented is designed to control the voltage and current profiles of both the fuel cell and the load to serve as the online diagnostic and mitigation system. The outcomes of this research improves the power generation capability, reduces the time to failure of the fuel cell system while providing detailed information on the interaction of the load on the internal chemical stability and performance of the fuel cell components.

1.2 Research Questions

The main research question that needs to be addressed in this thesis can be posed as follows:

"How can we detect and improve tolerance to fault conditions in fuel cells in order to increase performance and life expectancy?"

The above can be disseminated into the following individual questions that are addressed throughout this project:

- What is currently known about PEM fuel cell fault and degradation mechanisms?
- What can be used to quantify these fault mechanisms?
- How can these fault mechanisms be detected using electrical signal injection into the fuel cell? In particular, can small load perturbations be analyzed using advanced signal processing algorithms to identify fault markers?
- What power conversion topologies are currently being used to regulate fuel cell power and what are the limitations of each?
- Can these be modified to perform online detection and mitigation?
- What further modifications must be made in order to actively control the fuel cell and load voltage and current profiles to reduce the impact of various fault phenomena?
- How can the fuel cell fault mechanisms be mitigated or slowed using the power profiles?

1.3 Research Objectives

The objectives of this thesis will aim to address the above mentioned research questions. This is performed as follows:

- Conduct a detailed literature survey on fuel cells with emphasis on high temperature proton exchange membrane fuel cells and the available classification and detection strategies. The survey will highlight the detrimental effects such systems have on the materials of the membrane electrode assemblies (MEA).

- Test the fuel cell under various operating conditions including fault conditions in order to capture and evaluate electrochemical parameter changes.
- Use the experimental data to develop reduced order models of the fuel cell system that can be used to predict fuel cell behaviour.
- Use the model to facilitate development of a real time emulator system that can estimate performance under extreme operating conditions.
- Determine an optimal load current waveform that will increase system performance and reduce MEA degradation by using current injection and interruption techniques. The highly dynamic load conditions pose a great challenge to decrease the detrimental effect on the fuel cells. This study aims to improve durability and system life cycle by controlling the injected load current trajectory, frequencies and magnitudes.
- Investigate the application of advanced signal processing techniques for the use of fault detection on fuel cell systems. This includes testing on single cells to determine feasibility.
- Develop a new system that can extract electrochemical impedance information within a very short time frame during extreme fault conditions.

It is envisaged that the findings from the research will contribute to the efforts of the South African initiative (HySA Systems) to produce a commercially successful fuel cell system that may be introduced to the mainstream market. The results will also be applied to the up and coming electrical automotive industry and will assist in producing reliable fuel cell electrical vehicles.

1.4 Research Methodology

The methodologies used to complete this project are both analytical and experimental. The fuel cell electrical behaviour is quantified through thorough laboratory testing. The results from the experimental analysis are used to generate semi-empirical electrochemical models. These models are then implemented in mathematical computer simulation packages, and the results are used to identify the critical parameters in a reduced order

electrical model that can be used in online condition monitoring systems. The fault markers identified during the experimental testing of the fuel cell enables the system to estimate the state of health of the fuel cell. Fault mitigation strategies are tested in the laboratory for specific fault conditions that can occur in a commercial system to verify performance.

1.5 Chapter Summaries and Contributions of the Thesis

Chapter 2 presents an overview of the possible fault mechanisms that can occur in PEM fuel cell systems. The two different temperature classes for PEM fuel cells are discussed and the advantages and disadvantages of each presented. A stepwise approach to the global condition monitoring strategy is adopted for further reference in the thesis. The available methods used for each stage of fuel cell condition monitoring are presented and the shortcomings are identified. The current avenues where further research and development is required are discussed and it is shown how the results and proposed methods presented in this thesis attempt to address some of them.

Chapter 3 presents the evaluation of a High Temperature Proton Exchange Membrane (HT-PEM) Fuel Cell for different degradation mechanisms using equivalent circuit analysis. Specific consideration is given to the variation of phosphoric acid content in the polybenzimidazole (PBI) membrane and the effect on the equivalent circuit. The importance of the cell assembly and operating conditions on acid migration are discussed and it is shown how it affects performance both in the short term and the long term operation of the High Temperature PEM cell. A new method is developed whereby acid leaching can be greatly accelerated in order to quantify performance loss. The change in system parameters as a function of MEA acid content is investigated using Electrochemical Impedance Spectroscopy (EIS) and compared to the changes during variation of normal operating parameters of the system, catalyst degradation, CO poisoning and reactant starvation. It is shown, by using the equivalent circuits, that the drop in performance relating to the individual degradation mechanisms in the cell can be investigated and isolated for fault classification in online diagnostic systems.

Chapter 4 presents an approach for modelling fault and degradation mechanisms associated HT-PEM fuel cells for the implementation on real time emulator systems. The three main degradation mechanisms that can reduce long and short term performance in HT-PEM fuel cells are investigated and the specific electrochemical parameters that are affected are identified. A semi-empirical modelling approach based on captured experimental data is used to model the degradation mechanisms in order to reduce complexity. In particular, the effect of ripple current induced by the power electronics that accelerates degradation of the specific model parameters is discussed. Many models exist which account for numerous parameters to predict the behaviour of the fuel cell output voltage and current. These models are, however, computationally intensive and thus not suitable for the integration with a real time emulator. The presented dynamic model delivers acceptable accuracy when compared to an actual fuel cell. The models are integrated with the developed emulator system capable of reproducing the voltage and current behaviour of an actual fuel cell. The addition of the investigated fault conditions in fuel cell emulation introduces a new aspect for the development of mitigation strategies and hardware for the power conditioning subsystems that has been excluded in existing emulator systems.

Chapter 5 presents a detailed study on the impact of CO poisoning on the performance of HT-PEM fuel cells and proposes a new method for mitigating the long term effects by using natural current profiles. A dedicated test setup was constructed to perform both steady state and dynamic analysis on the fuel cell under a wide range of operating conditions and variations in CO content. The drop in performance captured in the polarization curves is modelled using a simple circuit model with a dedicated fault element. The captured impedance spectra from the electrochemical impedance spectroscopy (EIS) tests provide insight to the changes in the electrochemical circuit parameters that can be used to diagnose the extent of CO poisoning. Possible load control strategies that can reverse the CO poisoning is explored and the optimal profile is experimentally determined along with the long term effects.

Chapter 6 presents the variation of cell voltage for small current pulses for a range of operating conditions in order to investigate the effect on the voltage variation. A fault mechanism in the form of CO poisoning is introduced to further the study and evaluate the transients for diagnostic purposes. A new two stage diagnostic method is proposed based on

the transient and the use of the discrete S-transform for fault marker identification and a population based incremental learning (PBIL) algorithm for parameter extraction. The method is evaluated for both the healthy and faulted CO poisoning condition in order to verify performance.

Chapter 7 presents the development of a new rapid online condition monitoring system using **O**ptimized **B**roadband **I**mpedance **S**pectroscopy (OBIS). The hardware was specifically designed to be low cost and scalable to meet the needs of single cell and stack level testing. It is shown how classic electrochemical impedance spectroscopy (EIS) is limited when testing under extreme non-linear conditions. The design process of the broadband signal is tailored for PEM fuel cell diagnostics in order to minimize measurement time and system disturbance while maximizing accuracy. The long measurement time of standard EIS makes it impractical to use for rapid fault diagnosis and it is shown how the OBIS system is able to deliver impedance measurements under conditions where EIS cannot be applied. The proposed system is tested for an array of possible operational phenomena and faults and the results compared to that obtained from a commercial frequency response analyzer to demonstrate performance.

Chapter 8 draws conclusions based on the findings of the thesis and presents final remarks.

Appendix A presents additional work on modelling and emulation of LT-PEM flooding behaviour using a stack level emulator that falls slightly outside the scope of chapter 4. It is shown how water build-up influences the active area of the fuel cell and causes non-linear voltage decay. A purge event is introduced to remove the liquid water and enforce voltage recovery.

1.6 Research Outputs

Parts of the work presented in this thesis were presented at refereed conferences, published in peer reviewed journals and filed as a provisional patent.

Conference Publications:

1. C. de Beer, P.S. Barendse, M.A. Khan and P. Pillay, “Modeling and Emulation of Fuel Cell Flooding Behavior”, *IEEE PowerAfrica*, Johannesburg, South Africa, 2012.

2. C. de Beer, P.S. Barendse, P. Pillay, B. Bullecks and R. Rengaswamy, "Operational Study on Low Temperature and High Temperature PEM Fuel Cells", *South African Universities Power Engineering Conference (SAUPEC)*, Potchefstroom, 2013.
3. C. de Beer, P.S. Barendse, P. Pillay, B. Bullecks and R. Rengaswamy, "Degradation of High Temperature PEM Fuel Cells and the Impact on Electrical Performance", *IEEE International Conference on Industrial Technology (ICIT)*, Cape Town, 2013.
4. C. de Beer, P.S. Barendse, P. Pillay, B. Bullecks and R. Rengaswamy, "Electrical Circuit Analysis of CO Poisoning in High Temperature PEM Fuel Cells for Rapid Fault Diagnostics", *IEEE Energy Conversion Congress and Expo (ECCE'13)*, Denver Colorado, 2013.
5. C. de Beer, P.S. Barendse, P. Pillay, B. Bullecks and R. Rengaswamy, " Online Fault Diagnostics and Impedance Signature Mapping of High Temperature PEM Fuel Cells Using Rapid Small Signal Injection", *IEEE Industrial Electronics Conference (IECON)*, Vienna Austria, 2013.
6. C. de Beer, P.S. Barendse, P. Pillay, B. Bullecks and R. Rengaswamy, "Development of an Integrated Laboratory Test Setup for High Temperature PEM Fuel Cell Performance Studies", *South African Universities Power Engineering Conference (SAUPEC),* Durban, 2014.
7. C. de Beer, P.S. Barendse, P. Pillay, B. Bullecks and R. Rengaswamy, "Derivation of an Equivalent Electrical Circuit Model for Degradation Mechanisms in High Temperature PEM Fuel Cells in Performance Estimation", *IEEE Energy Conversion Congress and Expo (ECCE'14)*, Accepted for presentation.

Journal Publications:

1. C. de Beer, P.S. Barendse, P. Pillay, B. Bullecks and R. Rengaswamy, "Electrical Circuit Analysis of CO Poisoning in High Temperature PEM Fuel Cells for Fault Diagnostics and Mitigation", *Industry Applications, IEEE Transactions on*, Accepted for publication.
2. C. de Beer, P.S. Barendse, P. Pillay, B. Bullecks and R. Rengaswamy, "Online Diagnostics of HTPEM Fuel Cells Using Small Amplitude Transient Analysis", *IEEE Transactions on Industrial Electronics Special session,* under review.
3. C. de Beer, P.S. Barendse, P. Pillay, B. Bullecks and R. Rengaswamy, "Classification of High Temperature PEM Fuel Cell Performance Degradation Using Equivalent Circuits", *IEEE Transactions on Industrial Electronics Special session,* under review.
4. C. de Beer, P.S. Barendse, P. Pillay, "Fuel Cell Condition Monitoring Using Optimized Broadband Impedance Spectroscopy", *IEEE Transactions on Industrial Electronics Special session,* under review.

Provisional Patents Filed:

PPA GB 1411419.3: Apparatus and Method for Determining the Condition of an Electricity-Producing Cell. This patent is based on the OBIS system developed in Chapter 7.

Awards:

Best research paper award:

Presented at the *IEEE International Conference on Industrial Technology (ICIT)*, Cape Town, 2013, for the paper entitled: "Degradation of High Temperature PEM Fuel Cells and the Impact on Electrical Performance".

Chapter 2

Fuel Cell Degradation Mechanisms and Condition Monitoring Techniques

2.1 Introduction

The modern world has created an insatiable demand for energy to drive growth and development. This demand was met by fossil fuels and corresponding technologies in the 20th and 21st centuries and continues as the primary energy source. Natural gas and shale gas obtained from the so called “fracking” method has also been employed to meet the ever growing energy requirements of modern society. The environmental impact resulting from the use of these energy sources and the sustainability has been a growing concern. In response, renewable energy sources such as solar, wind and geothermal generation have received considerable attention to act as an alternative for energy supply. These systems have been implemented by a number of countries to assist with base power generation in national power grids. Energy storage devices and systems that can act as a replacement energy carrier for fossil fuels in the automotive market have also been the focus of recent research. In the portable electronic and emerging electric vehicle markets, batteries have been the technology of choice. These systems have inherent drawbacks that include long charge times, limited energy densities and high costs. As an alternative, fuel cells have

been developed to resolve some of these limitations.

Fuel cells act as electrochemical energy conversion devices that convert reactants or fuels directly into electrical energy without an intermediate phase. This process can be highly efficient and sustainable provided that the reactants are obtained in a similar manner. Unlike a battery, a fuel cell does not store charge but requires a constant supply of reactants to deliver electrical power. The system has a positive and negative electrode that facilitates the reactions but does not partake or undergo chemical changes as is the case with battery systems. The inherent changes in the internal chemistry of batteries facilitates the charging and discharging processes and causes limitations in the charge times associated with these systems. In contrast, fuel cells can produce electrical power as long as reactants are being supplied and have been implemented in fuel cell electric vehicles that may deliver longer travel distances and shorter filling times. Despite the advantages, fuel cell systems still face a number of challenges before they can be deployed on a very large scale. On an operational level, hydrogen infrastructure including the generation and storage thereof must still be developed. The manufacturing and life cycle of the technology is dependent on the complexity and durability of the materials and is one of the primary focal areas for research and development.

To ensure that performance is maintained for a reasonable period of operational time and usage, the fuel cell must be monitored and the state of health continuously determined. This allows the system to not only mitigate certain faults that can occur during operation but also minimize downtime during maintenance and repair. The condition monitoring of fuel cells is not a simple process and requires detailed knowledge of the possible operational and fault conditions, and the various diagnostic methods and procedures that can be employed. Due to the complex nature of the electrochemical system, the available methods are severely limited in terms of measurement time and complexity to implement. It is the goal of this thesis to not only improve our understanding of the effect of faults on the internal mechanisms but also to develop new detection strategies and methodologies that can quantify these effects very rapidly for online condition monitoring purposes.

2.2 Technology overview

2.2.1 Polymer Membrane as a Proton Conductor

Many types of fuel cells are available with each making use of certain materials and reactants to operate under specific conditions and serve a particular function. The different technologies are typically classified by the electrolyte and determine the fuel composition that can be used. Detailed discussions on the different types can be found in literature [1]. Recently, the Proton Exchange Membrane or Polymer Electrolyte (PEM) fuel cell has arisen as the technology of choice for the portable power markets and fuel cell electric vehicle manufacturers. PEM fuel cells have short start-up times, high efficiencies and power densities and are fairly simple to manufacture [1]. These characteristics have allowed PEM fuel cells to capture the majority of the current fuel cell market with a recent survey attributing it with an 80% share [2]. The technology has been applied in almost every type of application from base power supply in national power grids to usage on the space station. The basic principle of operation requires that Hydrogen be fed to the anode and Oxygen to the cathode. The Hydrogen splits into positive ions and electrons where it recombines with the Oxygen on the cathode side to form water. The solid polymer that acts as the membrane is situated between the anode and cathode catalyst layers and allows the Hydrogen ions to pass through while blocking the electrons. When the fuel cell is connected to an external load or circuit, the electrons flow through the circuit delivering power.

A schematic of the physical structure of the fuel cell assembly is presented in Fig. 2.1. The membrane electrode assembly consists of the polymer membrane situated between the catalyst layers. The catalyst layers consist of a carbon support with finely dispersed platinum particles [1]. This doping mechanism increases the effective surface area of the platinum resulting in an increase in chemical reactivity during the fuel cell reaction. The catalyst layers are fabricated onto the gas diffusion layers (GDL) and are typically manufactured from a carbon cloth or a carbon fibre matrix. The GDL must be electrically conductive and allow the reactant gasses to diffuse to the catalyst layers. The complete Membrane Electrode Assembly (MEA) is clamped between the two graphite bipolar plates that act as the current collectors. Etched into the plates are the flow fields that allow the reactant gasses to flow across the surface area of the diffusion layers. Many different types of flow field patterns have been developed in order to increase electrical conductivity and gas diffusion surface area [3].

Most PEM fuel cells make use of a perfluorosulfonic acid (PFSA), ex. Nafion by Dupont,

membrane that must be humidified to ensure proton conductivity. These cells typically operate in a temperature range between 60°C and 80°C. As a result, the water flow in the gas channels is considered to be in a two-phase state, meaning both liquid and vapour phase. The low operating temperature and the humidification requirement gives rise to water management issues within the fuel cell assembly.

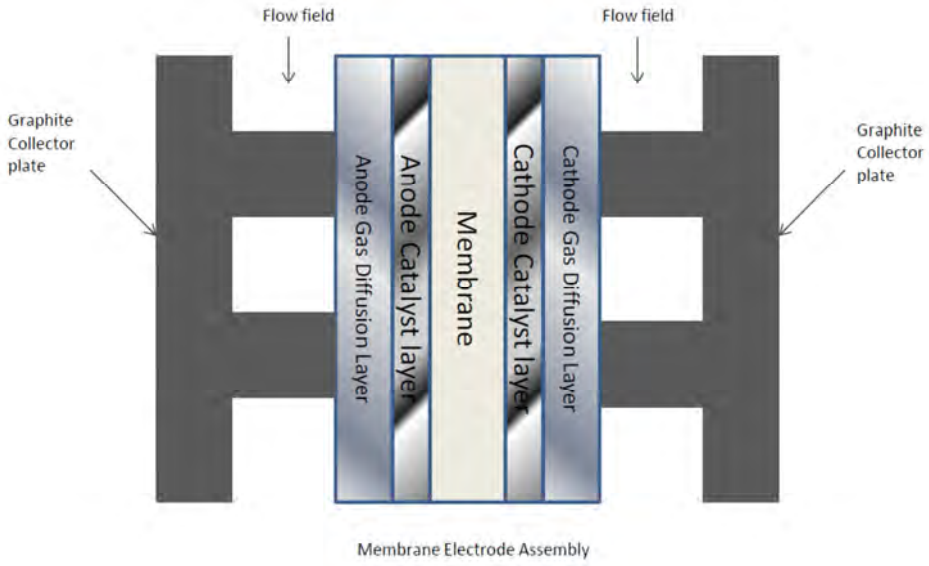

Figure 2.1. PEM fuel cell schematic.

2.2.2 Transition to Higher Operating Temperatures

In order to improve performance and mitigate the water management issues, PEM fuel cells have been developed that operate at higher temperatures. These High Temperature (HT) PEM fuel cells require different materials to withstand the operating conditions. The most viable membrane developed to date is polybenzimidazole (PBI) [4]. To enable proton conduction, the membrane must be doped with phosphoric acid. The typical operating temperatures of HT-PEM fuel cell systems range between 120°C and 180°C. At these temperatures, the acid becomes immobile and the water generated can be assumed to be in vapour phase only [5]. Operation at higher temperatures leads to several prominent advantages. Firstly, the electrochemical kinetics is enhanced and leads to increased system efficiencies and output power. Secondly, the higher temperatures allow the cooling system to be simplified as the thermal gradient between the fuel cell and ambient is greater. Further system simplification is possible due to liquid water no longer being present. This

results in a simplified water management system and removal of the gas humidification systems. Other advantages include increased tolerance towards impurities (such as CO and sulphides) in the gas streams, leading to simplified gas cleaning systems when hydrogen is generated from other fuel sources. It is, however, possible for HT-PEM fuel cells to undergo performance loss at very high concentrations of impurities. This thesis will examine this phenomenon in detail and propose innovative methods for mitigating the effects.

2.3 Performance Degradation

The drop in performance of fuel cells can occur due to a number of factors. During operation, components of the MEA and the cell assembly can start to degrade with the degradation rate being dependant on various conditions. This will cause an ultimate decline in output power until complete system failure occurs. While component degradation is inevitable, it is possible to limit the degradation rate of the individual mechanisms to extend system life expectancy. It is also possible for certain fault conditions that accelerate degradation to be mitigated by employing an appropriate control strategy thereby improving the time to failure in the system. For this to be viable, the individual degradation phenomena must be properly classified and understood in order to enable early detection during the execution of diagnostic protocols. For normal PEM fuel cells operating below 100°C, hereafter referred to as Low Temperature (LT-PEM) fuel cells, a large number of studies have been conducted and the fault mechanisms are mostly understood [6]-[8]. HT-PEM fuel cells, however, are the focus of the research community since a number of these fault mechanisms are still not properly understood or quantified. In this thesis, investigations and results obtained from HT-PEM fuel cells under the key degradation conditions are analyzed. The resulting impact on the electrical performance and equivalent circuit models pertaining to classification is then presented to further our understanding.

Fuel cells require a catalyst to facilitate the oxidation and reduction reactions at the anode and cathode reaction sites. In PEM fuel cells, the industry standard is the use of platinum that is finely dispersed on a carbon support. The loss of active surface area of platinum can occur due to a number of mechanisms with the most prevalent causes summarised in table 2.1 [8]. The loss of catalyst surface area is highly susceptible to

potential cycling as significant rates of change in overpotential across the electrodes cause increased intermolecular stresses that enforce surface area loss. The primary cause of such cycling is attributed to the connection of power electronic converters to the terminals of a fuel cell. The switching characteristics of the converters can introduce both low and high frequency ripple that result in varying degrees of surface area loss. With the low frequency ripple typically being generated due to inverter operation in an AC system and the high frequency ripple being caused by the PWM switching operation of the power electronics. The other components that make up a functioning fuel cell are also susceptible to degradation based on extreme operating conditions such as temperature fluctuations and over compression of the fuel cell assemblies. The most prominent being the degradation of the membrane and gas diffusion layers. Mechanical and thermal stresses will cause accelerated rates of failure in these components. The formation of pin-holes, perforations or tears in the membrane can lead to gas crossover and unwanted reactions taking place and ultimately to catastrophic failure [9].

In HT-PEM MEAs, the membrane must be doped with liquid phosphoric acid. Improper operation and assembly can lead to redistribution and leaching causing severe performance loss. Little has been done to characterize the resulting effect of the acid leaching mechanism on electrical performance and models to predict lifetime and is the focus of current work. Further component degradation, albeit less destructive, takes place in the bipolar plates, seals and gaskets. A list of possible failure modes and causes in these cell components are presented in table 2.2 [9]. The bipolar plates in a fuel cell are most generally manufactured from high density graphite due to the high conductivity, gas impermeability and corrosion resistant properties [10]. This enables the material to serve well as a gas separator while maintaining good electrical contact between the GDL and the adjacent plates in a stack. Graphite exhibits poor mechanical strength and is susceptible to a number of failure and degradation mechanisms. Therefore, recent works have focused on developing new metallic and carbon-composite materials for use in fuel cell applications [10]. Gasket and seal degradation has not undergone extensive study as has been performed with the aforementioned components. Degradation is, however, still possible and can lead to gas leaks, gas crossover and reduced pressures on the GDL. Various accelerated stress and lifetime testing standards have been developed to determine component failure rates with the most widely used protocols developed by the US department of energy (DOE)

[11].

In general, the effect of extreme operating conditions on the MEA is investigated by running the cell under open circuit voltage (OCV) or by performing enhanced load cycling tests [12], [13]. Operating under OCV conditions can lead to peroxide radical formation that will accelerate chemical degradation of the membrane. Load cycling forces the cell to undergo aggressive current changes and causes wet-up and dry-out cycles that lead to mechanical stresses and degradation.

TABLE 2.1
POSSIBLE FAULTS LEADING TO EFFECTIVE ELECTRO-CATALYTIC SURFACE LOSS

Mechanism	*Cause*	*Effect*
Catalyst degradation (agglomeration/dissolution)	Reactant starvation	Reduction in active surface area
	Ageing	Catalyst in exhaust water
	Potential cycling	Increase in Pt particle size
Carbon Corrosion	Reactant starvation	Uneven current distribution
	Flooding	Temperature distribution
	Obstruction of reactant flow in channels/GDL	Increase of cell voltage dispersion
	Potential cycling	Reverse flow at outlet
	Start-up and shutdown	Presence of C, CO and CO_2 in exhaust gas
Starvation	Flooding	Uneven current distribution
	Insufficient reactant supply	Temperature distribution
	Uneven supply of reactants	Increase of cell voltage dispersion

TABLE 2.2
FAILURE MODES RESULTING IN COMPONENT DEGRADATION

Component	*Cause*	*Effect*
Membrane	Non-uniform and high clamping pressures	Mechanical degradation
	Thermal stress and thermal cycling	Thermal degradation
	Contamination and Radical attack	Chemical degradation
Gas diffusion layers	Degradation of carbon materials	Loss of mass transport
	Mechanical stress	Loss of water transport ability
	Corrosion	Loss of conductivity
Bipolar plates	Corrosion	Loss of conductivity
	Mechanical stress	Component fracture
Sealing gaskets	Corrosion	Mechanical failure
	Mechanical stress	

2.4 The Art of Fuel Cell Condition Monitoring

The condition monitoring strategy can be broken down into four sequences as shown in Fig. 2.2. The first step involves the data acquisition and may require the use of certain electrochemical diagnostic methods that will be discussed in the following section. After the diagnostic techniques have been employed, the marker or parameter calculation must be performed. This may involve the use of simple fitting procedures to more advanced signal processing methodologies. Once the markers have been determined, the state of health or fault condition can be determined and classified for identification. This step can involve very complex multidimensional models or simple lookup tables. Finally, if a fault condition has been identified, an appropriate mitigation strategy can be employed by the master control via any of the sub-systems to clear the fault or shut the system down to limit component degradation.

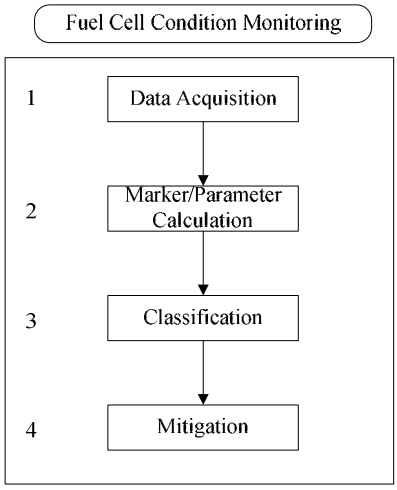

Figure 2.2. Condition monitoring strategy.

2.4.1 Diagnostic Tools for Data Acquisition

In order to execute the condition monitoring strategy as outlined above, operational data from the fuel cell is required. For detailed diagnostics, electrochemical methods are usually employed. These methods provide important information required for the design and optimization of fuel cell systems. The diagnostic methodologies are used to gather data regarding cell performance, material properties and assessing its state of health. Diagnostic

procedures can be divided into intrusive and non-intrusive procedures as shown in Fig. 2.3. Non-intrusive procedures are performed to record data during the fuel cell life cycle in order to quantify performance and assess the loss mechanisms. The methods do not cause component degradation and can be performed repeatedly. In contrast, intrusive procedures can lead to accelerated performance loss and are typically performed at the end of life (EOL) or after component failure. For the purpose of ensuring that cell lifetime is not negatively affected, the non-intrusive procedures are performed in this work. These include polarization curve analysis, current interrupt (CI), electrochemical impedance spectroscopy (EIS), gas cross-over and others [14]. These methods can be further subdivided into invasive and non-invasive procedures where invasive refers to procedures that require the cell to be functioning but not delivering power to an application. Non-invasive procedures can be performed online while the fuel cell is delivering power with minimal impact on the performance.

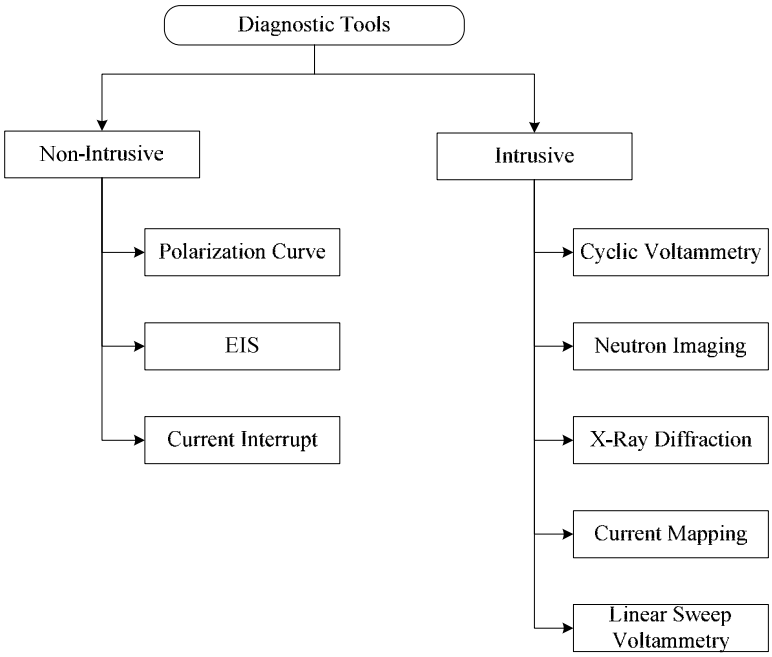

Figure 2.3. Classification of fuel cell diagnostic tools.

2.4.1.1 Polarization Curve Analysis

A polarization curve represents the V-I characteristics of a fuel cell at a specific operating condition. From the data, the maximum power point can be calculated and performance optimized. The curve is one of the most standard electrochemical procedures

that can be performed and gives information on the activation losses, ohmic losses and diffusion through the triple-phase boundary. A typical polarization curve is presented in Fig. 2.4 along with the loss regions. From the data, the three loss regions are clearly identifiable and can be used for optimization of the system and control. The curve is generated by increasing or decreasing the voltage or current of the cell. At each increment the cell is allowed to stabilize before the measurement is recorded. A polarization curve does not provide detailed information on individual component performance and it is difficult to diagnose a specific fault condition. It is also not possible to record a curve while the fuel cell is operational and delivering power to a load.

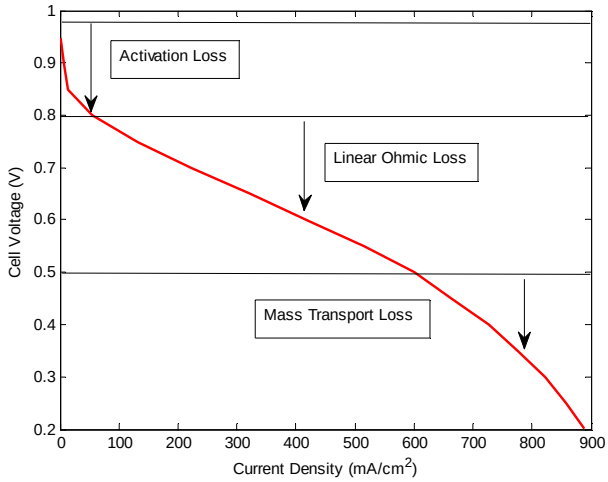

Figure 2.4. Voltage loss components of the polarization curve.

2.4.1.2 Electrochemical Impedance Spectroscopy

Electrochemical impedance spectroscopy (EIS) is conducted at a specific loading point and can be done while the fuel cell is in operation making it a non-invasive procedure. The technique requires that a sinusoidal waveform be superimposed upon the DC load point, either voltage or current. The feedback is then measured and the magnitude and phase of the resulting impedance calculated. The frequency of the sine wave is varied, typically between 0.1Hz and 10kHz in order to produce a full spectrum Nyquist plot of the impedance. A graphical representation is presented in Fig. 2.5 at the operating point on the polarization curve. The magnitude of the sine wave is varied to maintain good signal to noise ratio while minimizing the disturbance on the fuel cell output. The resulting Nyquist plot is usually fitted to the impedance spectrum of an electrochemical equivalent circuit.

By monitoring the values of the circuit elements, a number of tasks can be performed. This includes investigating the performance of individual cell components as well as fault diagnostics. Most laboratory setups make use of a frequency response analyzer (FRA) and a potentiostat module to perform EIS. More recently, it was shown how high performance electronic loads and controllers can perform the same tests without the use of the expensive FRA [14].

Proper evaluation of the fuel cell impedance can yield valuable information on the state of health of internal components and is a powerful tool in condition monitoring. The drawback of the methodology is the long measurement time associated with the technique while requiring expensive and complex equipment to perform the task. To reduce the measurement time, this thesis will examine and propose possible alternative strategies to obtain the impedance data while minimizing system cost, complexity and execution time.

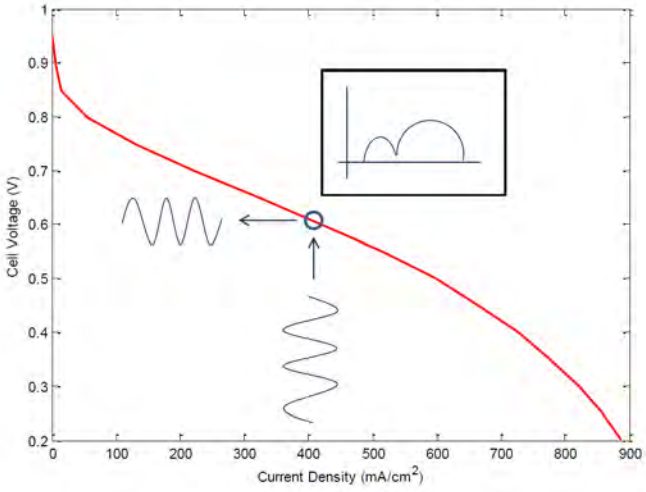

Figure 2.5. Polarization curve and EIS at a specific operating point.

2.4.1.3 Current Interrupt

A non-intrusive technique that can be performed by most test stations is the current interrupt (CI) technique. This method mainly gives information regarding the impedance of the fuel cell and requires that the fuel cell load be switched or stepped between two current set-points. The voltage response is then recorded and time domain analysis is performed to determine a transfer function of the impedance for the system. A typical voltage response for a CI of a fuel cell is presented in Fig. 2.6. The fitted components of the

impedance transfer function can be related to certain electrochemical parameters such as membrane ionic resistance, charge double layer capacitance and charge transfer resistance. Depending on the impedance model used and the fitting procedure, the technique can yield very good results when compared to the more complex methods such as EIS.

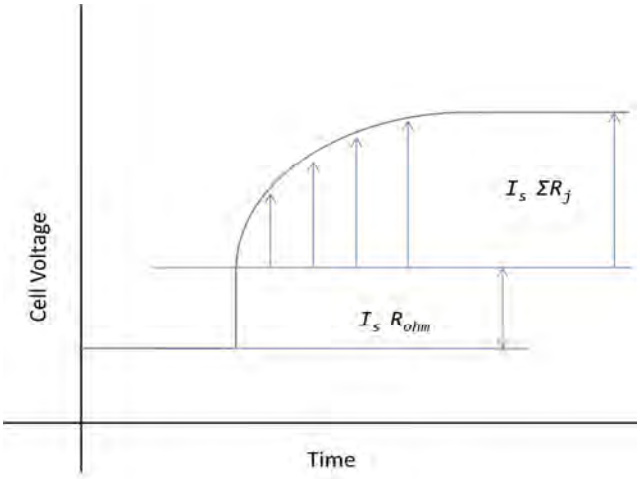

Figure 2.6. Typical voltage response from current interrupt.

2.4.1.4 Other Methods

To determine the extent of catalyst degradation, the electro-catalytic surface area (ECSA) can be determined using cyclic voltammetry (CV). This method requires the use of a potentionstat or galvanostat to drive the fuel cell voltage and then measure the feedback current. For in-situ measurements, a two electrode configuration is used where the working electrode of interest is typically the fuel cell cathode and the reference and counter electrode is selected as the anode. The voltage is linearly varied between two chosen set-points at a few millivolts per second. The current-voltage plots that are generated are referred to as voltammograms and provide valuable information on catalyst utilization. The use of CV on fuel cells can lead to additional degradation of the catalyst/carbon due to the high cell potentials involved and therefore it is typically performed during end of life studies [15]. Other more advanced methods include neutron imaging, used to capture visual images of liquid water in the flow channels, X-ray diffraction and current density mapping. These methods require dedicated and expensive laboratory setups and are generally not suited for online condition monitoring in functioning fuel cells.

2.4.2 Marker Identification and Fault Classification

Once data has been obtained from the fuel cell, methods can be used to perform marker identification and classification in order to diagnose the fault condition. These methodologies can be divided into two categories. These include model based and non-model based strategies and employ various techniques ranging in functionality and complexity.

2.4.2.1 Non-Model Based Methods

The first set of identifiers and classifiers make use of methods that do not require a pre selected or developed model and are thus non-model based. The principle behind these methods involves a data driven heuristic approach to fault identification where complex electrochemical models are not required [16]. In general, the non-model based methods can be divided into three sub categories, as shown in Fig. 2.7 [17]. The first category makes use of pattern recognition and can be used on the fuel cell output current and voltage profiles. The objective of the classifier is to act as a pattern recognition system as is the case with Neural Networks and Fuzzy Logic. Cluster recognition is performed with Fuzzy clustering and has also been used in fuel cell diagnostics where separate clusters and groups represent different fault mechanisms that can occur. More advanced methods in the form of Adaptive Neural Fuzzy Logic and Genetic algorithms have also been used to predict fuel cell performance [18].

During steady state or transients, the fuel cell current or voltage outputs can exhibit certain characteristics that can be identified and classified using signal processing methods. For steady state or periodic excitations, standard frequency domain methodologies can be applied. These include the Fourier Transform and derivatives thereof. It has been shown how the total harmonic distortion of the fuel cell, calculated using standard FFT, can be used to classify certain fault mechanisms [19]. For transient analysis, time-frequency domain signal processing methods can be applied. The Short Time Fourier Transform (STFT), being a variant of standard FFT with a moving window, can easily be applied to non-stationary signals. The drawback of this transform includes the fixed window size that leads to poor time-frequency localization. Therefore other transforms have been proposed, including the Gabor and Cohen class distributions. A general form for these distributions can be expressed as follows [20]:

$$P(t,\omega) = \frac{1}{4\pi^2}\iiint e^{-j\theta t - j\tau\omega + j\theta u}\varphi(\theta,\tau) * s^*\left(u - \frac{1}{2}\tau\right)s\left(u + \frac{1}{2}\tau\right)dud\tau d\theta \qquad (2.1)$$

Where $\varphi(\theta,\tau)$ is the arbitrary kernel function by Claasen and Mecklenbrauker [20], t the time and ω the frequency. By changing the kernel function, different distributions can be obtained. The Wigner, Rihaczek and Page distributions have kernel functions of $\varphi(\theta,\tau)=1$, $e^{j\theta\tau/2}$ and $e^{j\theta|\tau|/2}$ respectively. The application of these distributions is complex to execute and interpret for diagnostic purposes and the selection of the kernel function is difficult to perform.

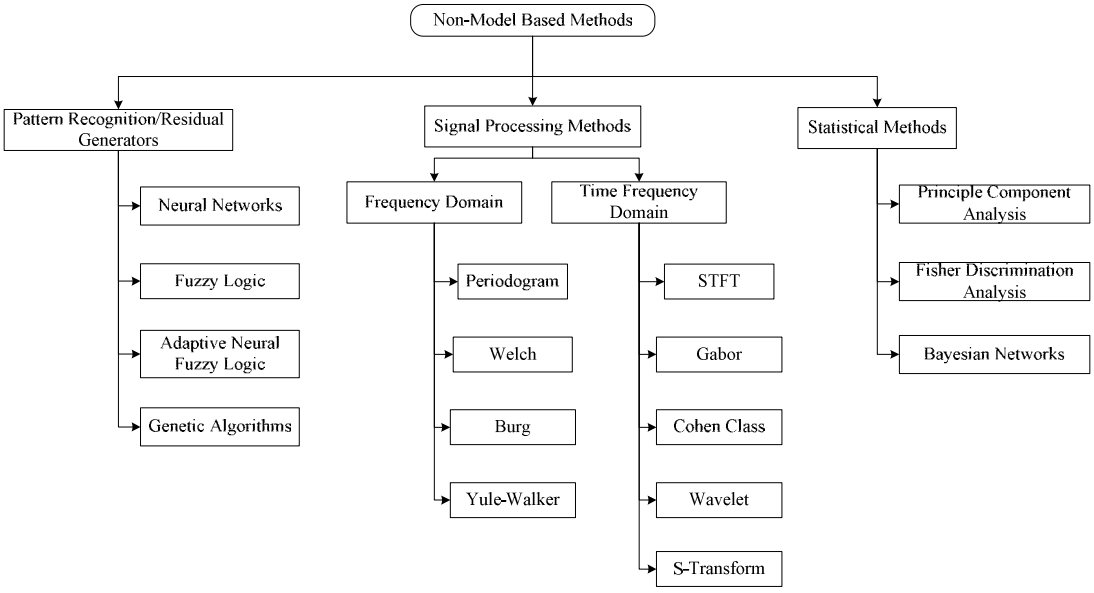

Figure 2.7. Non-model based diagnostic methods.

More recently, advanced signal processing methods such as the continuous and discrete wavelet transforms have been applied to fuel cell diagnostics. The wavelet transform uses a scaling function and a wavelet function that act as transitory windows within the time-frequency plane. Both the continuous and discrete wavelet transforms have been applied to fuel cell state of health estimation in recent work [21]-[23]. Some of the problems associated with the proposed methods are the dependency on the mother wavelet that can influence the results, susceptibility to noise and algorithm complexity for real time implementation. In an attempt to resolve some of these limitations, this thesis proposes the use of the S-transform for the evaluation of small transients to diagnose state of health, as will be discussed in more detail in the following chapters.

Statistical methods can be applied to large data sets in order to differentiate between healthy and faulted conditions. Towards this end, dimension reduction methods such as principle component analysis, Fisher discrimination analysis and Bayesian networks can be applied for feature extraction in the datasets [17]. The methods are well suited for classification during off-line analysis but not for real time or online implementation.

2.4.2.2 Model Based Methods

Fuel cell models are developed to perform a number of functions and assist with the development and control of the systems. During the design stages, proper simulation can yield new solutions to persisting problems encountered during operation. Model based diagnostics can be classified into three groups, as shown in Fig. 2.8. For detailed analysis, analytical models based on fundamental electrochemical relationships are preferred. These can range in complexity from single dimension to multidimensional finite element models that require significant computational power to simulate. In contrast, black-box models are data driven in order to reduce complexity. This makes them attractive in online systems for monitoring, control and diagnostics [24]. While this is a major advantage, the limitations imposed by available experimental data and the possible operational conditions that were used to generate the models make the use of black-box models highly specific. To overcome some of these limitations, semi-empirical models have been proposed. These models make use of fundamental electrochemical formulations and experimental data in order to produce empirical relationships that can replace highly complex analytical ones. This is particularly useful when phenomena that are not well understood must be incorporated into the model.

Semi-empirical models have relatively low computational complexity and produce lumped parameter models that can be implemented in online classifiers. For observer based systems, the model is run in parallel with the system control and certain parameters monitored. The observer generates residuals by using the predicted and actual values measured. Once this has been done the residuals are compared with set-thresholds to determine state of health and operation. If the thresholds are breached, certain fault conditions can be declared and isolated.

Parameter estimation is popular with the use of equivalent circuit models. These models can be fitted to experimental data generated via EIS. The method is simple and effective

and can provide fast estimations of internal component performance for evaluation. A comprehensive study of published works and their use for failure mode analysis using EIS and the other electrochemical techniques is presented in [25]. It has been shown how variation of certain markers or parameters can be linked to specific fault mechanisms. In online systems, the model parameters are monitored in order to determine if certain thresholds are exceeded. This allows for fault classification and isolation with minimal computational effort.

As with non-model based methods, black-box models using neural networks and fuzzy logic can be used to predict fuel cell behaviour. The input/output relationships are built upon experimental data sets. For highly non-linear systems, these models can perform well without the need of the complex analytical relationships that would normally be associated with fuel cells. The models typically require separate data sets for training and for model validation thereby limiting possible operating and fault scenarios that can be simulated to those captured in the experimental data. Other black-box methods used include support vector machines (SVM) that use a statistical learning approach and produce very good correlation with experimental data [26]. Further development is still required to extend the models for diagnostics.

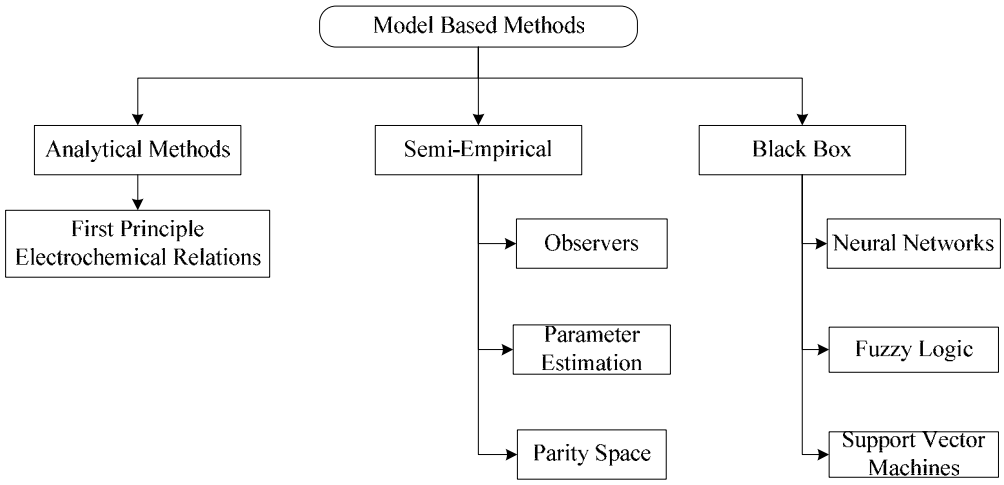

Figure 2.8. Model based diagnostic methods.

2.4.3 Mitigation

Mitigation strategies for certain degradation mechanisms have been reviewed in

literature [8], [9] and [25]. In order to reduce the impact of certain mechanisms on performance loss, alternative materials or composites were designed and implemented. To reduce mechanical failure of the membrane related to water management, the design of the MEA and flow fields must be considered to avoid local drying or flooding. This can be reduced further with proper system control where the humidification and internal water generation of the fuel cell is actively monitored. By varying the current drawn from the cell, flooding and drying can potentially be avoided as the reaction rate can be changed to produce more or less water at the cathode side [27].

Catalyst and carbon corrosion can be minimised by avoiding large cell potentials as this has been proven to accelerate the degradation mechanisms [8], [12]. The reduction of intermolecular stresses due to potential cycling can be reduced with proper control of the power electronic subsystems. Platinum surface area loss due to catalyst poisoning can be reduced by operating at higher operating temperatures. Other proposed methods include the enhancement of electro-oxidation of the impurities via load cycling. This does, however, require further research in order to limit degradation that might occur and is the focus of parts of this thesis.

Conclusion

This chapter presents a detailed overview of the condition monitoring strategy employed in modern fuel cell systems. The four main areas of research and development are divided into sub-categories to provide a stepwise approach to fuel cell condition monitoring. The assembly and operation of the PEM fuel cell is presented and discussed. To gain a better understanding of the possible failure modes associated with the fuel cell, the possible degradation mechanisms are investigated. The electrochemical diagnostic methods used to evaluate the performance loss and generate data for fault identification and classification is presented. This was then followed by listing the most prevalent methods used to perform fault identification. Finally, possible mitigation strategies are introduced. The key features associated with the techniques for the different stages of the condition monitoring strategy is presented and discussed. This serves as the foundation for the proceeding chapters whereby specific focus is given towards ensuring the developed methodologies be implemented online.

The critical paths for further research and development in each of stage of the condition

monitoring strategy were identified and form the basis for the contributions presented in this thesis; the fault identification and classification knowledge base is extended in chapter 3 and 4 for HT-PEM fuel cells by developing equivalent circuit models and reduced order semi-empirical models, a new mitigation strategy is proposed for CO poisoning in HT-PEM fuel cells in chapter 5 and rapid online fault detection methodologies are developed in chapters 6 and 7.

References

[1] F. Barbir, PEM Fuel Cells Theory and Practice, Elsevier, 2005.

[2] Fuel Cell Today Industry Review 2013, Fuel Cell Today.

[3] Ryan Anderson, Lifeng Zhang, Yulong Ding, Mauricio Blanco, Xiaotao Bi, David P. Wilkinson," A critical review of two-phase flow in gas flow channels of proton exchange membrane fuel cells", *Journal of Power Sources*, Vol. 195, Issue 15, pp. 4531-4553, 1 August 2010.

[4] Jianlu Zang et al., "High Temperature PEM Fuel Cells", *Journal of Power Sources*, Vol. 160, pp 872-892, 2006.

[5] A. Su, Y.M. Ferng, J. Hou, T.L. Yu, "Experimental and numerical investigations of the effects of PBI loading and operating temperature on a high-temperature PEMFC", *International Journal of Hydrogen Energy*, Vol. 37 pp. 7710-7718, 2012.

[6] Hui Li et al., "A review of water flooding issues in the proton exchange membrane fuel cell", *Journal of Power Sources*, Vol. 178, Jan 2008.

[7] N. Yousfi-Steiner et al., "A review on PEM voltage degradation associated with water management: Impacts, influent factors and characterization", *Journal of Power Sources*, Vol. 183, April 2008.

[8] N. Yousfi-Steiner, Ph. Moçotéguy, D. Candusso, D. Hissel, "A review on polymer electrolyte membrane fuel cell catalyst degradation and starvation issues: Causes, consequences and diagnostic for mitigation", *Journal of Power Sources*, Volume 194, Issue 1, pp. 130-145, 20 October 2009.

[9] Jinfeng Wu, Xiao Zi Yuan, Jonathan J. Martin, Haijiang Wang, Jiujun Zhang, Jun Shen, Shaohong Wu, Walter Merida," A review of PEM fuel cell durability: Degradation mechanisms and mitigation strategies", *Journal of Power Sources*, Volume 184, Issue 1, pp. 104-119, 15 September 2008.

[10] Reza Taherian, "A review of composite and metallic bipolar plates in proton exchange membrane fuel cell: Materials, fabrication, and material selection", *Journal of Power Sources*, Volume 265, pp. 370-390, 1 November 2014.

[11] Xiao-Zi Yuan, Hui Li, Shengsheng Zhang, Jonathan Martin, Haijiang Wang, "A review of polymer electrolyte membrane fuel cell durability test protocols", *Journal of Power Sources*, Volume 196, Issue 22, pp. 9107-9116, 15 November 2011.

[12] Shengsheng Zhang, Xiaozi Yuan, Haijiang Wang, Walter Mérida, Hong Zhu, Jun Shen, Shaohong Wu, Jiujun Zhang, "A review of accelerated stress tests of MEA durability in PEM fuel cells", *International Journal of Hydrogen Energy*, Volume 34, Issue 1, pp. 388-404, January 2009.

[13] C. Lim, L. Ghassemzadeh, F. Van Hove, M. Lauritzen, J. Kolodziej, G.G. Wang, S. Holdcroft, E. Kjeang, "Membrane degradation during combined chemical and mechanical accelerated stress testing of polymer electrolyte fuel cells", *Journal of Power Sources*, Volume 257, pp. 102-110, 1 July 2014.

[14] H. Wang, X. Yuan, PEM Fuel Cell Diagnostic Tools, CRC Press, 2012.

[15] Young-Chul Park, Katsuyoshi Kakinuma, Makoto Uchida, Hiroyuki Uchida, Masahiro Watanabe, "Deleterious effects of interim cyclic voltammetry on Pt/carbon black catalyst degradation during start-up/shutdown cycling evaluation", *Electrochimica Acta*, Volume 123, pp. 84-92, 20 March 2014.

[16] Zhongliang Li, Rachid Outbib, Daniel Hissel, Stefan Giurgea, "Data-driven diagnosis of PEM fuel cell: A comparative study", *Control Engineering Practice*, Volume 28, pp. 1-12 July 2014.

[17] Z. Zheng, R. Petrone, M.C. Péra, D. Hissel, M. Becherif, C. Pianese, N. Yousfi Steiner, M. Sorrentino, "A review on non-model based diagnosis methodologies for PEM fuel cell stacks and systems", *International Journal of Hydrogen Energy*, Volume 38, Issue 21, pp. 8914-8926, 17 July 2013.

[18] Yasemin Vural, Derek B. Ingham, Mohamed Pourkashanian, "Performance prediction of a proton exchange membrane fuel cell using the ANFIS model", *International Journal of Hydrogen Energy*, Volume 34, Issue 22, pp. 9181-9187 November 2009.

[19] Sobi Thomas, Sang C. Lee, A.K. Sahu, Sam Park, "Online health monitoring of a fuel cell using total harmonic distortion analysis", *International Journal of Hydrogen Energy*, Volume 39, Issue 9, pp. 4558-4565, 18 March 2014.

[20] Cohen, L., "Time-frequency distributions-a review," *Proceedings of the IEEE*, vol.77, no.7, pp. 941-981, July 1989.

[21] Jonghoon Kim, Yongsug Tak, "Implementation of discrete wavelet transform-based discrimination and state-of-health diagnosis for a polymer electrolyte membrane fuel cell", *International Journal of Hydrogen Energy*, Volume 39, Issue 20, pp. 10664-10682, 3 July 2014.

[22] Andrej Debenjak, Pavle Boškoski, Bojan Musizza, Janko Petrovčič, Đani Juričić, "Fast measurement of proton exchange membrane fuel cell impedance based on pseudo-random binary sequence perturbation signals and continuous wavelet transform", *Journal of Power Sources*, Volume 254, pp. 112-118, 15 May 2014.

[23] D. Benouioua, D. Candusso, F. Harel, L. Oukhellou, "Fuel cell diagnosis method based on multifractal analysis of stack voltage signal", *International Journal of Hydrogen Energy*, Volume 39, Issue 5, pp. 2236-2245, 4 February 2014.

[24] R. Petrone, Z. Zheng, D. Hissel, M.C. Péra, C. Pianese, M. Sorrentino, M. Becherif, N. Yousfi-Steiner, "A review on model-based diagnosis methodologies for PEMFCs", *International Journal of Hydrogen Energy*, Volume 38, Issue 17, pp. 7077-7091, 10 June 2013.

[25] H. Wang, X. Yuan, PEM Fuel Cell Failure Mode Analysis, CRC Press, 2012.

[26] Chun-Hua Li, Xin-Jian Zhu, Guang-Yi Cao, Sheng Sui, Ming-Ruo Hu, "Identification of the Hammerstein model of a PEMFC stack based on least squares support vector machines", *Journal of Power Sources*, Volume 175, Issue 1, pp. 303-316, 3 January 2008.

[27] Gebregergis, A; Pillay, P.; Rengaswamy, R., "PEMFC Fault Diagnosis, Modeling, and Mitigation," Industry *Applications, IEEE Transactions on*, vol.46, no.1, pp.295-303, Jan.-feb. 2010.

Chapter 3

Analysis and Classification of HT-PEM Fuel Cell Degradation Mechanisms

3.1 Introduction

PEM fuel cells have received considerable attention due to their high efficiency, good power density and ability to function well in small scale stationary, portable and automotive power applications [1]. The conventional PEM fuel cells use a hydrated Nafion membrane and typically operate at temperatures below 100°C. Therefore, the system faces a number of operational problems, including water management in the gas channels and intolerance to impurities, such as CO, in the gas streams [1], [2].

To avoid some of these issues, PEM fuel cells that operate at higher temperatures, 100°C to 200°C, have been developed. These HT-PEM fuel cells have a number of advantages, including improved system kinetics, the ability to use hydrogen from a reformer and a simplified cooling system due to the higher temperature gradients involved [2]. The dehydration and subsequent loss of proton conductivity of Nafion® at these temperatures require a different membrane structure and chemistry. Due to its physiochemical properties, polybenzimidazole (PBI) has emerged as a prime candidate for HT-PEM fuel cell applications [3]. PBI, serving as the physical structure, shows acceptable proton conductivity and gas permeability when doped with phosphoric acid (PA) [4].

Considerable effort has gone into determining the optimal doping method and PA concentration in the membrane [3], [5]-[12].

HT-PEM fuel cells still suffer from a number of problems that influence performance. In particular, the new materials experience degradation mechanisms that decrease the overall life expectancy of the fuel cell. A number of studies have been published to quantify the different mechanisms that contribute to performance loss under normal and accelerated life cycle tests [13]-[16]. The most important of these being: loss of carbon support, platinum agglomeration, dissolution and phosphoric acid loss [17], [18]. Several studies have been performed to evaluate how different operating conditions can influence these mechanisms [19], [20]. Further work was done to evaluate the electrical performance and parameter variation under different operating conditions via EIS [20]-[23]. However, there is no previous work that attempts to identify and distinguish the key degradation mechanisms in HT-PEM fuel cells using electrical equivalent circuits. In this chapter, the key fault mechanisms in HT-PEM fuel cells are examined using EIS and polarization curves. The impact of these fault mechanisms on the key circuit parameters of the electrochemical equivalent circuit (EEC) is then studied and accounted for. The variation of the adapted EEC is linked to physiological changes in the fuel cell along with detailed explanations provided. Afterwards a matrix is presented to assist in classifying the different fault mechanisms based on the variation of the identified parameters in the EEC. The investigated faults include catalyst/carbon degradation, reactant starvation, acid leaching and CO poisoning. Special focus is given to acid leaching and the developed accelerated leaching procedure as this is the one fault mechanism that was found to have the greatest impact on performance loss. Section 3.2 discusses the degradation mechanisms in further detail. Sections 3.3 and 3.4 describe the experimental setups and procedures followed in this work. The EEC used to evaluate the EIS data is presented in section 3.5. The experimental results, evaluations and the introduction of a fault classification matrix for diagnostics are presented in section 3.6. Finally, conclusions are drawn.

3.2 Degradation of HT-PEM Fuel Cells

Commercial PA doped membrane electrode assemblies have very good acid retention under stable operating conditions with acid loss recorded as $0.5\mu gm^{-2}s^{-1}$ [3]. However, these

tests are conducted under laboratory conditions with no extreme thermal or load cycling that would accelerate degradation. Other factors that must be taken into account are the assembly of the cell itself, since factors like clamping pressure on the MEA can increase the acid loss rate [24]. It is imperative that the changes in electrical parameters be tracked and quantified in order to diagnose the problem during implementation in a complete system. High temperature operation of PEM fuel cells increases the reaction kinetics and enforces certain corrosion and degradation mechanisms. In order to facilitate the electrochemical reaction, finely dispersed platinum particles are dispersed onto a carbon support in the catalyst layers of the anode and cathode. This maximizes the effective electrocatalytic surface area that takes part in the reaction of the fuel cell. During operation, various mechanisms cause degradation of the catalyst, including prolonged operation at open circuit voltage [16], [25], [26] current ripple as caused by power electronics [27], [28] and fuel starvation [29]-[31]. At higher temperatures, the catalyst/carbon degradation is accelerated and causes specific changes to the dynamic resistance of the fuel cell [25], [26].

The tolerance towards poisoning of the catalyst in HT-PEM fuel cells is significantly increased. This allows the system to operate from hydrogen generated by a reformer. During start-up of the system, it is possible for a sudden increase in CO concentration due to temperature fluctuations, which would cause a drop in performance. Detailed studies on CO poisoning and the effect on circuit model variations were presented in [22] and [32]. Most work on HT-PEM fuel cells focuses on life cycle tests and little has been done to isolate individual fault mechanisms that can occur during operation. For diagnostic purposes it is required that the main degradation or fault mechanisms be investigated and distinguished. These include fuel starvation, acid leaching, catalyst degradation and CO-poisoning. This work will use the results generated from EIS to identify and distinguish the variations in the circuit parameters. Specific consideration is given to acid leaching of the assembled cell as little has been done to quantify the effect on the electrochemical equivalent circuit (EEC). It is shown how each of the degradation mechanisms can be classified according to the variation of the EEC.

3.3 Experimental Setups

3.3.1 Cell Assembly

In this experimental procedure, a new HT-PEM cell, type P1100W from BASF, with an

active surface area of 45cm^2 was used at the start of the investigation for each fault mechanism. The MEAs were sealed to prevent absorption of moisture from the air. Upon assembly, the new MEA was removed from the bag and integrated with the cell assembly as quickly as possible. Total assembly time never exceeded 10 minutes.

The cell assembly was acquired from Fuel Cell Technologies and comprised a pair of graphite bipolar plates with quad serpentine flow fields. An exploded schematic of the single HT-PEM fuel cell assembly is presented in Fig. 3.1.

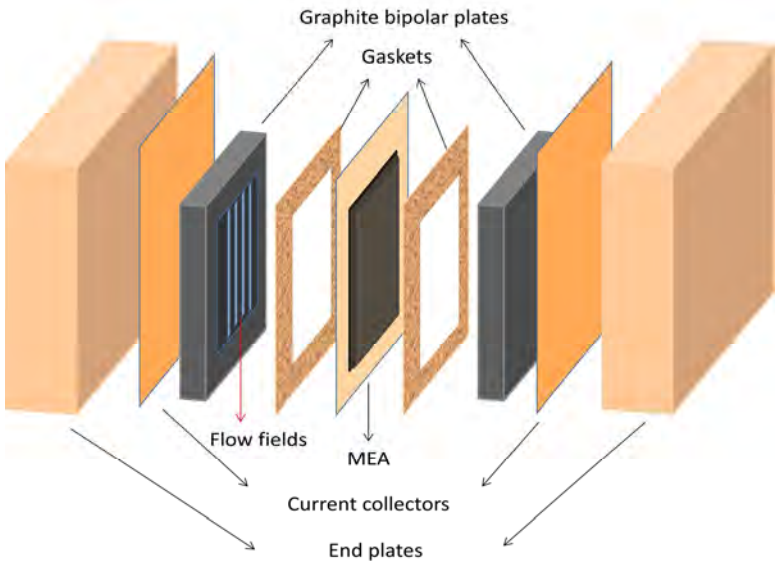

Figure 3.1. Schematic of the experimental fuel cell assembly.

The cell assembly was heated using cartridge heaters in the end plates. These were controlled using a dedicated temperature controller between the chosen set points of 140°C to 180°C while deviating with no more than 0.5°C during any point in time of operation.

3.3.2 Commercial Test Station

For the starvation, acid leaching and catalyst degradation studies testing was conducted on a commercial Scribner associates test bench, shown in Fig. 3.2, with the humidifiers kept at room temperature to avoid additional humidification of the gas streams. The gas transfer lines were heated to a set temperature of 85°C. During normal operation the cell was fed with compressed air on the cathode side and research grade hydrogen on the anode side.

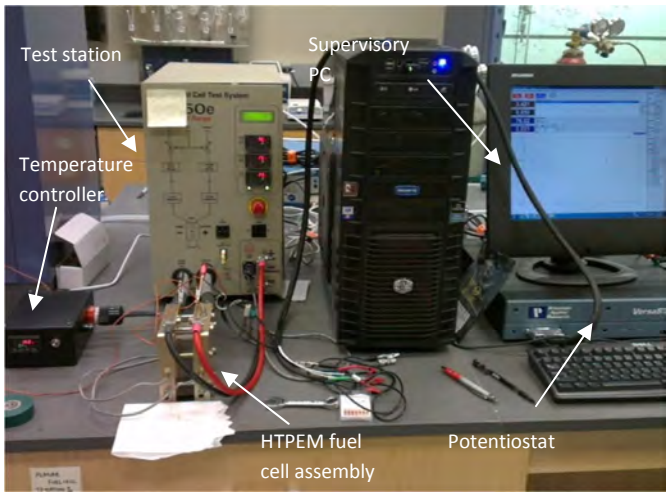

Figure 3.2. Commercial fuel cell test bench.

3.3.3 Custom Test Station

In order to introduce CO into the anode gas stream for the catalyst poisoning studies, a custom test bench was constructed capable of conducting both steady state and transient analysis. The experimental setup is presented in Fig. 3.3 and the schematic representing the test setup and equipment used is presented in Fig. 3.4. The cathode was supplied with compressed air and the flow controlled by the mass flow controller (MFC). The anode was supplied by two gas feed lines: a high purity hydrogen supply connected to the hydrogen mass flow controller and a 4% CO/hydrogen mixture, connected to the CO mass flow controller. All the mass flow controllers were supplied by Cole-Parmer and have a response time of 50ms, accuracy of ±0.8% and repeatability of ±0.2%. The gas flows and load flows were controlled by the single supervisory computer that also recorded the data captured by the data acquisition (DAQ) system. The DAQ has a maximum sampling frequency of 500 kHz that can be scaled down depending on the test being performed. The data acquisition was performed with MATLAB and the real time data acquisition toolbox.

The fuel cell current and voltage was controlled by the Agilent electronic load with the set points generated by the experimental script in MATLAB. The cell assembly was heated using cartridge heaters housed in the end plates. The temperature was controlled by a LOVE controls temperature controller with an integrated PI control system that was tuned during testing to maintain cell temperature at the chosen set point with minimum deviation.

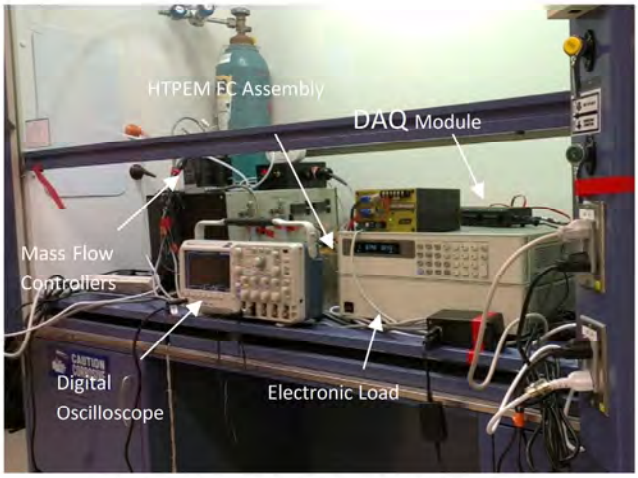

Figure 3.3. Experimental test setup.

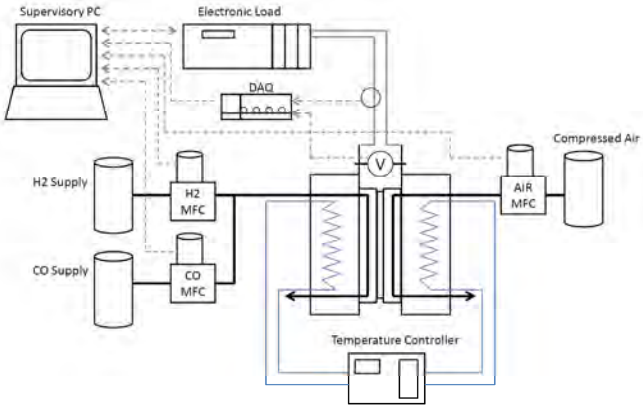

Figure 3.4. Schematic of the experimental test setup.

3.4 Experimental Procedures

3.4.1 Conditioning Procedure

The cell was run-in according to the manufacturer specifications before experimental analyses commenced to ensure the results were stable and repeatable. The run-in was conducted at an anode stoichiometry of 2.4 and a cathode stoichiometry of 4 to ensure that fuel starvation is avoided. The load current was kept constant at 0.2A/cm^2 for the total run-in period of 12 hours. The temperature was kept at a nominal operating temperature of 160°C during the run-in procedure as specified by the manufacturer.

3.4.2 Polarization Curve Analysis

The polarization curve provides information on the activation losses, ohmic losses and

diffusion through the triple-phase boundary. A typical polarization curve requires a substantial amount of time to record as the system must be allowed to reach complete steady state at each set-point. From the data, the three main loss mechanisms can be identified and investigated. A polarization curve does not deliver detailed information on individual component performance and it is difficult to diagnose a specific fault condition. The polarization curves are used to quantify the electrical performance of the fuel cell. To generate the polarization curves, the cell voltage was stepped in 0.05V increments and the current recorded after it had stabilized.

3.4.3 Electrochemical Impedance Spectroscopy (EIS)

For *in situ* Electrochemical Impedance Spectroscopy (EIS), a two electrode setup is usually implemented with the anode acting as both the counter and reference electrode. Compared to the three electrode configuration, this method delivers less information but is much easier to implement. Typical experimental setups implement a frequency response analyzer (FRA) in series with a programmable electronic load as was done on the commercial test station. The system can be simplified by removing the FRA and using only an electronic load with a high current and voltage slew rate as done on the custom test station. The analyses were performed by directly controlling the voltage or current profiles of the electronic load via an external control system.

The EIS tests were conducted using the integrated model 880 impedance analyzer on the Scribner test bench. The magnitude of the injected signal was varied with the load operating point to achieve satisfactory magnitudes on the response. The frequency was varied between 0.1Hz and 10kHz at 10 points per decade to generate the Nyquist plots.

For the custom test station, the EIS tests were conducted in galvanostatic mode whereby a sinusoidal signal was superimposed upon the DC current signal. The voltage feedback was recorded and the impedance calculated from the magnitude and phase difference of the voltage and current signals. As was done on the commercial test station, the frequency was varied from 0.1Hz to 10kHz at ten points per decade. The magnitude of the current perturbation was maintained in order to generate an adequate voltage response.

3.4.4 Accelerated Acid Leaching Procedure

A new method was developed to forcibly remove the PA from the MEA in order to quantify the effect of acid concentration on the performance of the HT-PEM fuel cell. Measurements and diagnostics had to be performed at various intervals during the leaching process. During ideal operation, very little acid loss occurs over time, which required that the process be accelerated in order to gain significant variations in the diagnostic test results for interpretation and quantification.

It was found that PA leaches out at a very aggressive rate if the cell is run in driven cell mode with Nitrogen on the cathode side at low temperatures (60°C-80°C). However, it proved difficult to control the amount of acid that is removed since it is also dependent on the specific operating conditions used. For the purpose of this test, the cell was driven by the high current potentiostat for a short interval before shutting down to determine the amount of acid removed. Determining the amount of acid lost by titration of the exiting gas streams was found to be ineffective due to a finite amount of acid being absorbed and retained by the porous graphite bipolar plates. This amount of acid could not be measured accurately and resulted in an error in the measurements. More accurate acid loss measurements were obtained by completely removing the MEA from the assembly, determining its weight by using a high resolution scale and then comparing with the weight of the MEA prior to testing.

To ensure all water was removed from the MEA, the cell was purged at high temperatures with Nitrogen. After weight measurements, the MEA was re-inserted into the assembly and the clamping bolts tightened to the initial torque in order to maintain constant contact pressure. This process was repeated for a number of iterations and thus different MEA acid concentrations. After reassembly, the cell was run for a period of one hour to allow performance to stabilize. It was found that the accelerated leaching process did not cause additional leaching during normal high temperature operation in the short term. However, further life cycle testing needs to be performed to evaluate the effects over a long period of time.

3.4.5 CO Poisoning Procedure

Polarization curves and EIS data were recorded for a constant stoichiometry of λ_A=2.4

and λ_C=4, and for a constant flow rate of M_A=300sccm and M_C=900sccm. The cell temperature was varied from 140°C to 180°C in 10°C steps. As the MEA was designed to work optimally between temperatures of 160°C and 180°C, the results presented in this thesis will be focused on this temperature region. The CO concentration in the anode gas stream was varied from 0% to 1% in 0.25% steps and in 0.5% steps above 1%. The pressures of the anode and cathode were constant at one atmosphere. Tests were conducted for both constant stoichiometry and constant flow to evaluate the effect of the surface concentration change of the gas species on electrical circuit parameter values. Higher system pressure will result in higher output voltages based on the Nernst relationship. In this work, the CO concentrations were tightly controlled. Similar trends compared to those presented in the following sections would thus be expected if the system was to be operated at higher pressures. Working at temperatures below 140°C resulted in a drop in performance and reduced tolerance to CO. It was found that the lower temperatures, higher CO concentrations produced inconsistent data as the cell voltages never reached complete steady state conditions and caused variations in the diagnostic measurements.

3.5 Electrical Equivalent Circuit Model

The Nyquist plot of the impedance is generated from the EIS data at each operating point. Variations in temperature, stoichiometry and current densities will affect the respective arcs within the spectrum. For a typical HT-PEM fuel cell, the impedance diagram will exhibit three distinct arcs. The recorded Nyquist plots exhibit several distinct features that are evaluated. Each of the arcs in the diagram can be related to a mechanism in the fuel cell and the equivalent circuit model. To quantify variations in the Nyquist plots, the circuit model in Fig. 3.5 can be used to fit the experimental data. The circuit model includes the low frequency and high frequency inductive elements that can generally be ignored. The inductive loops are formed due to stray cable impedance and do not contribute to the analysis of the fuel cell parameters.

The first parameter of interest is the ohmic resistance R_Ω. This value can be determined from the high frequency intercept of the semicircle with the real axis. R_Ω represents a value for the total ohmic resistance of the cell and includes the resistances of the bipolar

plates, membrane, gas diffusion layers and cable resistances. In most of the experimental plots captured, a high frequency semicircle can be observed, which is usually attributed to the porous electrodes of the cell. This arc is represented by the first of three resistor capacitor pairs, R_{el} and C_{el}. It was found that the magnitude and variation of these parameters in the EEC was small when compared with the other components and was removed from the circuit to reduce complexity. The second semicircle is a measure of the charge transfer of the oxidation reduction reaction (ORR) on the cathode side and can be affected by cathode parameters such as: catalyst loading, catalyst utilization and surface area [13], and is represented by R_{ct} and C_{ct}. The last semicircle gives information on the diffusion resistance or gas transport properties, and is represented by R_{gt} and C_{gt}. The capacitance in the circuit elements can be replaced by constant phase elements (CPE) to generate a better fit to the experimental plot.

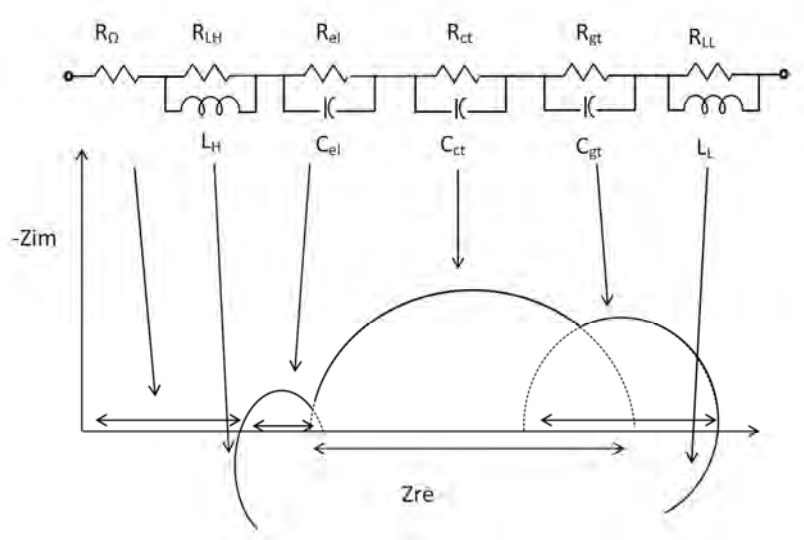

Figure 3.5. Typical Nyquist plot and EEC for an HT-PEM fuel cell.

If the electrode impedance sub-circuit and inductive elements are ignored, the impedance of the fuel cell using the EEC of Fig. 3.5 can be calculated as follows:

$$\overrightarrow{Z(\omega)} = R_{\Omega} + \frac{R_{ct}}{1 + j\omega R_{ct} C_{ct}} + \frac{R_{gt}}{1 + j\omega R_{gt} C_{gt}} \tag{3.1}$$

By setting the two time constants $\tau_1 = R_{ct} \times C_{ct}$ and $\tau_2 = R_{gt} \times C_{gt}$, $\vec{Z}$ can be rearranged as follows:

$$\overrightarrow{Z(\omega)} = R_{\Omega} + \frac{R_{ct}}{1 + \omega^2 \tau_1^2} + \frac{R_{gt}}{1 + j\omega^2 \tau_2^2} - j\omega \left[\frac{\tau_1 R_{ct}}{1 + \omega^2 \tau_1^2} + \frac{\tau_2 R_{gt}}{1 + j\omega^2 \tau_2^2} \right] \tag{3.2}$$

Where the first time constant represents the time constant associated with the charge transfer kinetics and the second time constant represents the gas diffusion dynamics. Variation in the time constants will lead to changes in the system response during load transients thereby affecting system performance.

3.6 Experimental Results

3.6.1 Variation in Operating Conditions

To accurately characterize the fuel cell under healthy operating conditions, polarization curves and Nyquist plots were recorded for changes in temperature, flow and stoichiometry. Initially, the cell was operated at a constant flow rate at both the anode and the cathode while varying temperature. From Fig. 3.6, it is clear that there is a significant increase in cell performance with a rise in temperature due to the higher electrochemical kinetics and improved conductive properties of the materials.

The Nyquist plots were recorded at a current density of 0.4A/cm^2, corresponding to an operating point in the linear ohmic region of the polarization curve for the different temperatures. From Fig. 3.7, the changes in the electrical parameters can be identified. The high, low and intermediate frequency arcs represented by the equivalent circuit are visible and can be related to the physical properties of the cell. The first high frequency intercept of the real axis decreases with an increase in cell temperature. Authors in [13], [14] stated that this part of the ohmic resistance can be related to the resistance of the electrolyte in the catalyst layer or to the construction of the cell itself. Since variations in temperature affect the conductivity of the phosphoric acid and the cell components, it can be assumed that all contribute to the value of the ohmic resistance value. The increased temperature reduces the diameter of the charge transfer semicircle and equivalently the charge transfer resistance, as expected due to the increased reaction rates. At elevated temperatures, the gas diffusion kinetics is improved, resulting in a decrease in the diameter of the low frequency semicircle and the equivalent gas transport resistance.

The cell was run at a constant stoichiometric ratio while the temperature was varied. The Nyquist plots for a stoichiometric ratio of 2.4/4 are shown in Fig. 3.8. The low frequency semicircle becomes less visible when compared to constant flow results of Fig. 3.7 mainly due to the increased flow rate and the reduced diffusion resistance. The low

frequency inductive loop is now visible for the same low frequency test limit of 0.1Hz used for the EIS. Changes in current density to demonstrate the effect on charge transfer resistance are shown in Fig. 3.9.

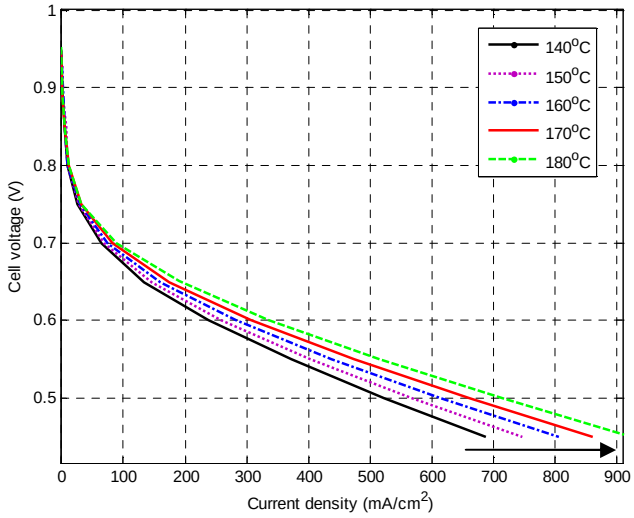

Figure 3.6. Polarization curves for variations in cell temperature at a constant stoichiometry.

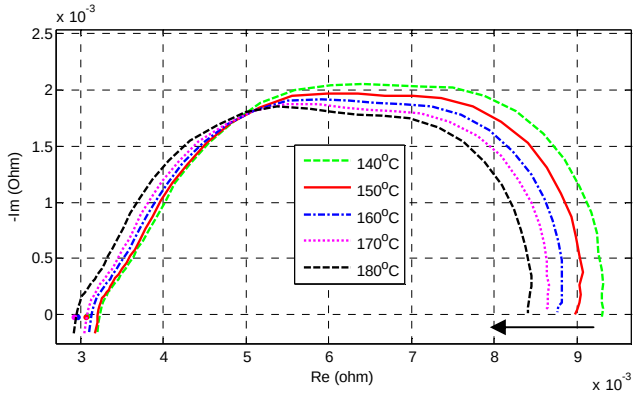

Figure 3.7. Nyquist plots for variations in cell temperature at 400mA/cm² with a constant flow rate of A: 300sccm C: 900sccm.

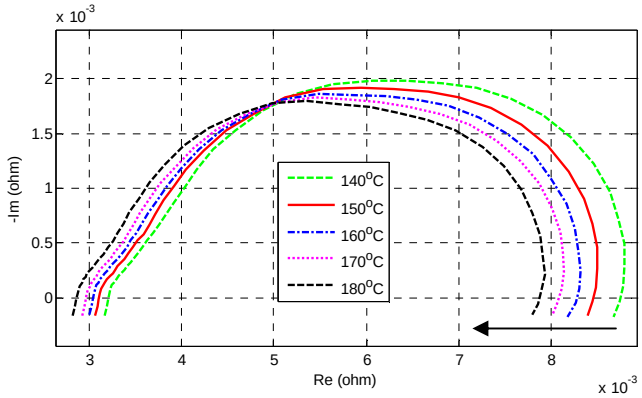

Figure 3.8. Nyquist plots for variations in cell temperature at 400mA/cm² at a stiochiometric ratio of 2.4/4.

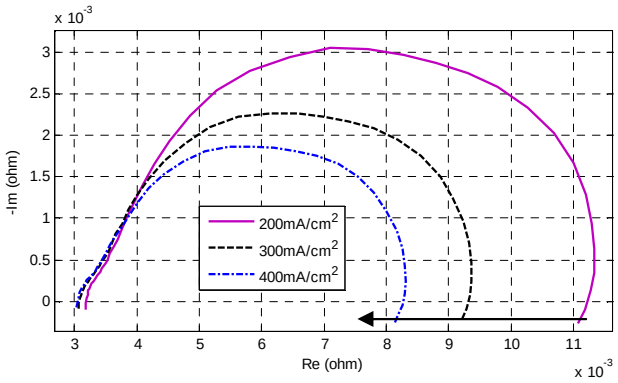

Figure 3.9. Nyquist plots for variations in current densities at constant stoichiometric ratio of 2.4/4 at 160°C.

3.6.2 Reactant Starvation Circuit Variations

An important factor to consider in the fuel cell system is the flow control of the anode and cathode gas streams. This is of particular importance where the load is not constant and subject to large transients. During operation the cell or stack must be supplied with reactants at a flow rate that is sufficient to maintain the required concentration at the reaction sites. Due to diffusion losses and other physical limitations the flow is typically kept above a specific safety margin. Since the flow must be varied with the applied current density, the mass flow controllers must have a fast response time in order to maintain the stoichiometric ratio. If the current is increased and the flow rate is below the required set-point, reactant starvation can occur, which leads to an immediate drop in performance [29], [30]. Long term operation under starved conditions can lead to catalyst degradation and will be discussed in the following section. In this work the flow rates were tightly controlled via the mass flow controllers. To observe the effects of possible reactant starvation on the equivalent circuit, the stoichiometric ratio was dropped from an excess of 3/3 to 2/2. The drop in output voltage is presented in the polarization curves of Fig. 3.10. The Nyquist plots for these two flow conditions are presented in Fig. 3.11 whereby the change in the EIS Nyquist plots is clearly visible and distinct. There is minimal change in the ohmic resistance as expected while the charge transfer resistance also demonstrates negligible change. The primary variation for this condition can be captured in the gas transport resistance. The drop in flow reduces the gas transport rate of the reactants through the micro porous layers and the gas diffusion layers. Therefore, the variation in flow and the subsequent fuel starvation that can occur is proportional to the gas transport

resistance of the EEC. The fault parameter for this effect can be included as an additional resistance, ΔR_{fs}, in series with the gas transport resistance R_{gt}, as shown in Fig. 3.12. The variation of the capacitance of the gas transport sub-circuit is included as ΔC_{fs}. By fitting the EEC to the experimental Nyquist plots, the values for the circuit elements and the variation for changes in the flow rates were determined and presented in table 3.1. For the reduced flow, the gas transport capacitance increases and will lead to increased response times during load transients.

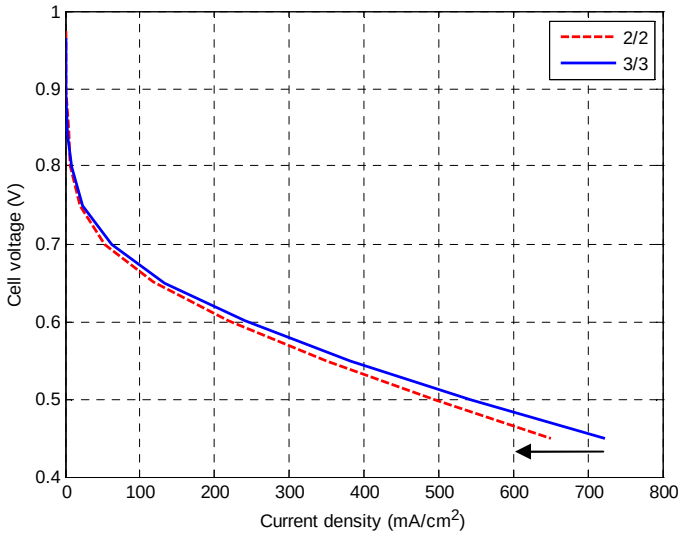

Figure 3.10. Polarization curves for variations in stoichiometry at 160°C.

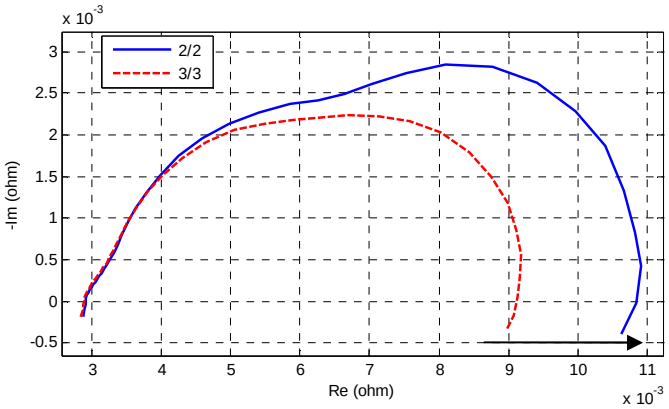

Figure 3.11. Nyquist plots for variations in stoichiometry at 400mA/cm² at 160°C.

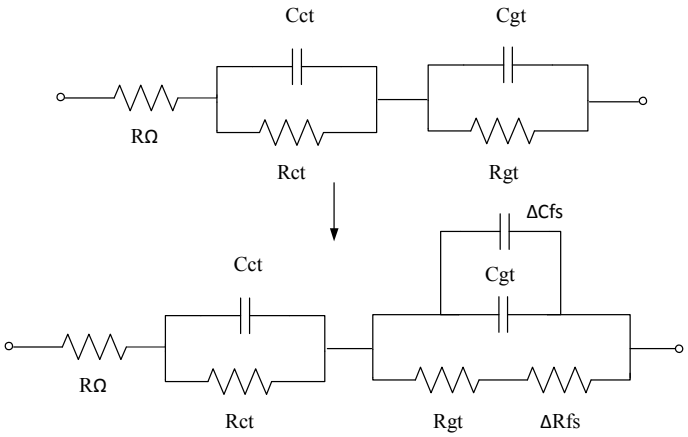

Figure 3.12. Variation in the EEC for the fuel starvation fault.

TABLE 3.1
VARIATION OF EEC PARAMETERS FOR REACTANT STARVATION

RΩ (Ω)	*Rct (Ω)*	*Cct (F)*	*Rgt (Ω)*	*ΔRfs (Ω)*	*Cgt (F)*	*ΔCfs(F)*
			3/3			
0.00289	0.00244	5.6364	0.00373	-	18.654	-
			2/2			
0.00291	0.00284	5.7542	0.00518	0.00145	22.485	3.8309

3.6.3 Acid Leaching Circuit Variations

Under extreme loading or operational conditions, the HT-PEM fuel cell can exhibit a fault condition where the proton conducting electrolyte is lost from the assembly. This phenomenon is commonly referred to as acid leaching. A number of studies have been conducted that investigate the variation on the conductance of the membrane with the acid content [3], [6], [15], and to quantify operational parameters and performance on a complete and functioning cell [7]-[9].

Acid loss in a HT-PEM fuel cell may be attributed to a number of factors. The most important of these include incorrect assembly procedures of the cell or stack assembly [24], operation under heavy load for long periods of time, extreme dynamic load conditions and operation at low or incorrect cell temperatures [7]-[10]. For a newly doped membrane, the PA can contribute up to 70%-80% of the total membrane weight [3]. The acid doping process requires that the membrane be submerged in PA solutions for extended periods of time. The concentration of the solution and the temperature can be varied to increase acid uptake and reduce the time until equilibrium concentrations are reached. Other methods

have been proposed where the membrane is impregnated via the catalyst layers [8]. Studies have also shown that when the initial doping level of the membrane is too high, electrode flooding with PA can occur [33] causing a drop in performance. During the run-in procedure, the acid is redistributed between the membrane and catalyst layers and is influenced by the initial clamping pressure of the cell assembly on the MEA. High clamping pressures on the MEA can enforce leaching, as can be observed in Fig. 3.13a. The acid that is lost is either vented through the gas outlets or can be absorbed by the graphite bipolar plates, as shown in Fig. 3.13b. Both anode and cathode sides exhibited the effects of leaching as observed in the figures.

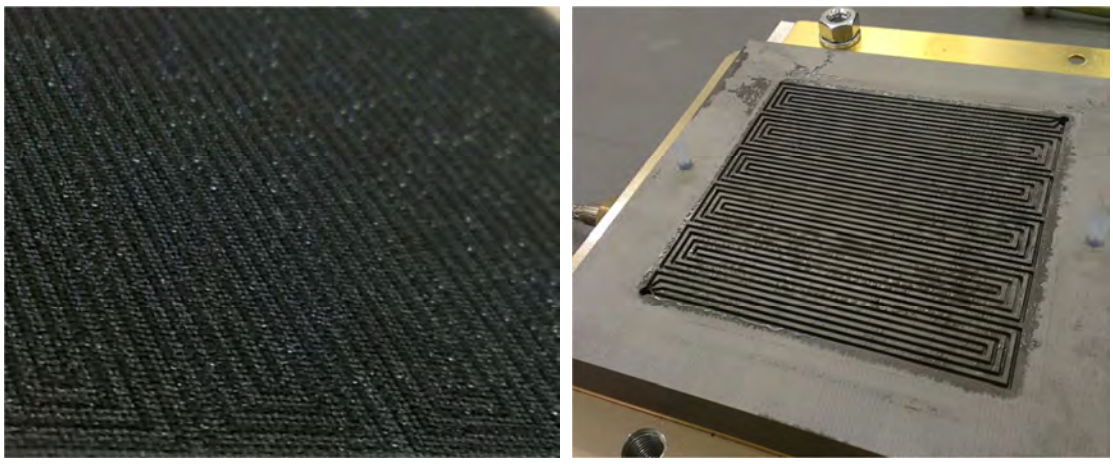

Figure 3.13. Image captured of (a) acid loss from the MEA and (b) absorbed by the bipolar plates.

Fig. 3.14 shows the polarization curves for the new MEA and for different degrees of acid loss. The second curve was recorded after 12%wt of the MEA was lost. At this point, the MEA was only producing 50% of the original power output, demonstrating the effect of acid loss on performance. The corresponding Nyquist plots are shown in Fig. 3.15. The results compare well with those in other published works where the initial doping level of the membrane was varied [7]-[11], [33]. The polarization curves show similar drops in performance for PA variation and confirm the viability of the proposed testing and accelerated leaching procedures.

Polarization curves and EIS curves were recorded for different levels of MEA acid content until performance had dropped to 30%. The Nyquist plots clearly demonstrate the effect of acid loss on the electrical parameters of the EEC. The effective diameter increases

and the entire plot shifts away from the origin. This corresponds to EIS results for variation in initial membrane doping levels in literature [11], [33]. However, since acid leaching is now greatly accelerated, other effects on the MEA morphology must also be considered. A schematic representation of the physiochemical changes that can occur during the acid leaching process is presented in Fig. 3.16. For a saturated MEA, the PBI exhibits substantial ion conducting pathways similar to a properly hydrated Nafion membrane. This ensures that membrane ionic resistance is low and facilitates charge transfer in the catalyst layer. The results from various tests conducted in [10], [11] indicate that variation in the acid content will have a direct effect on the membrane volume, thickness and area. It can be assumed that acid leaching will result in some physical changes inside the MEA, as shown in Fig. 3.16 and contributes to the changes observed in the Nyquist plots and the EEC.

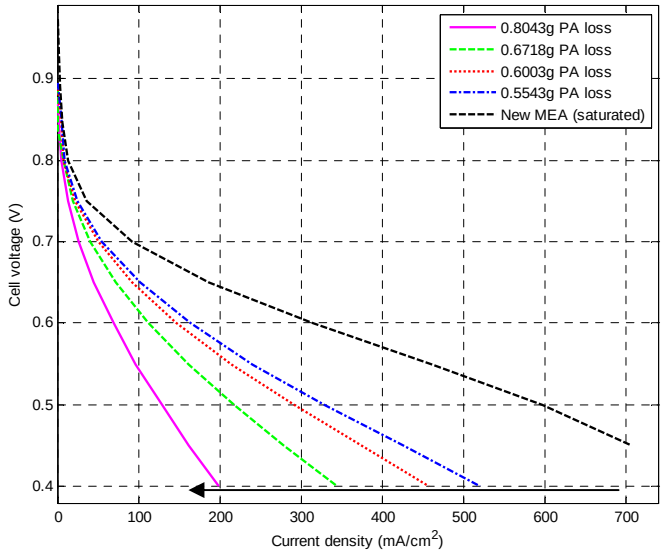

Figure 3.14. Polarization curves for different acid weight loss at 160°C.

Once acid leaching has taken place there will be a reduction in volume, thickness and conductivity of the membrane along with slight possible variations in the gas diffusion layers (GDL). This will result in the increase in the ohmic resistance that was observed in Fig. 3.15. For the step wise increase in acid loss, the Nyquist plots shift gradually away from the origin as the ability of the PBI to provide ionic conduction is lost. The diameter increase of the plots demonstrates the increased resistance to charge transfer. The changes to the EEC for the acid leaching effect are presented in Fig. 3.17 and the parameter values determined from the fitting procedure in table 3.2. The increased ohmic resistance is

included as ΔR_{Ω}, the change to the charge transfer is included as ΔR_{al} and the change to the gas transport resistance as ΔR_{am}. The change to the gas transport resistance results from the migration of acid from the membrane to the gas diffusion layer. This causes a reduction in effective pore size that is required for diffusion of the gasses due to acid blocking the pores. For an increase in acid loss and migration from the MEA, the diffusion resistance will increase.

The change of ohmic resistance with acid loss is shown in Fig. 3.18. The initial 50% performance loss corresponds to a change of 3.166mΩ/g or 70μΩcm^{-2}g^{-1} in ohmic resistance compared to a change of 56.4mΩ/g or 1.25mΩcm^{-2}g^{-1} thereafter. The increase in the ohmic resistance is expected as the loss of PA in the MEA effectively reduces the thickness of the membrane and increases the contact resistance between the MEA and the bipolar plates of the cell assembly. The contact resistance is a function of both the compression force and the MEA morphology. Due to the loss of acid the MEA undergoes changes in morphology, as shown in Fig. 3.16, which leads to increased contact resistance. It was found that by increasing the clamping pressures, by tightening the assembly bolts, improved surface contact after leaching was observed, resulting in reduced ohmic resistances.

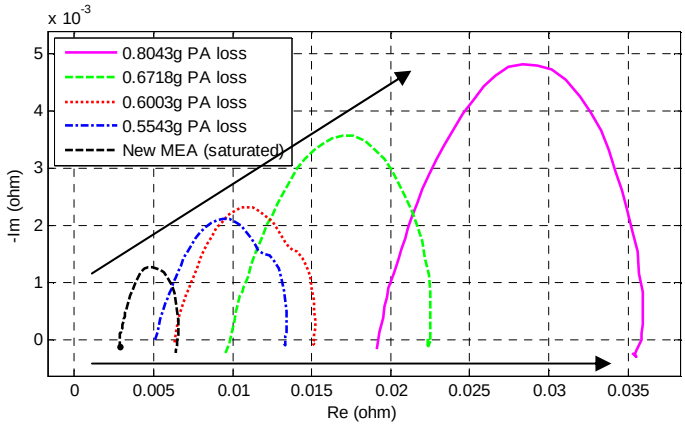

Figure 3.15. Nyquist plots for different acid weight loss at 160°C.

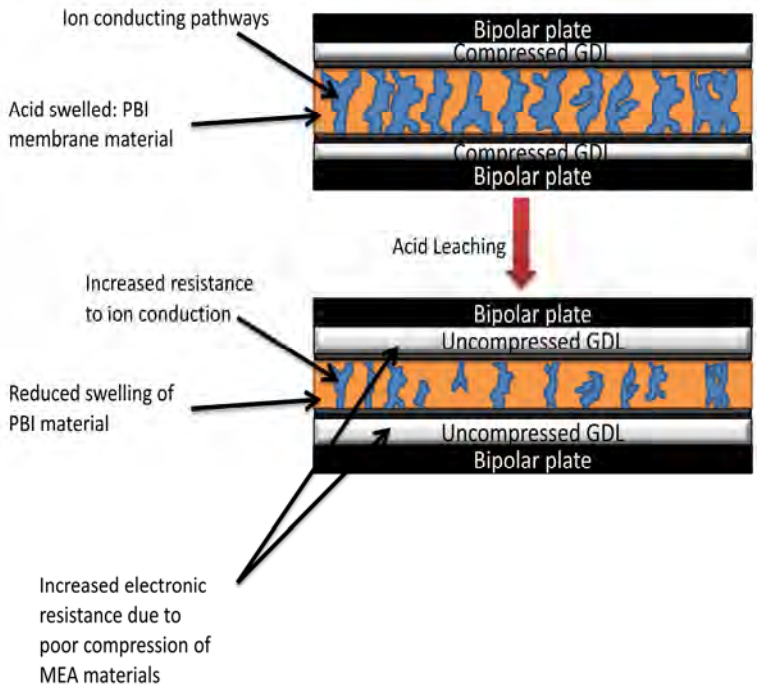

Figure 3.16. Schematic detailing changes in the MEA and assembly with acid loss.

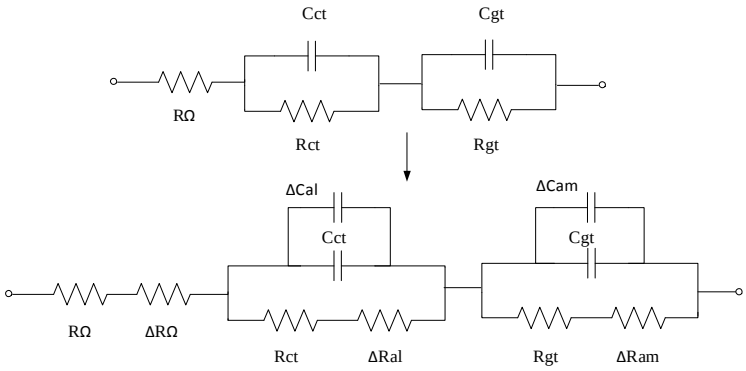

Figure 3.17. Variation in the EEC for the acid leaching phenomenon.

TABLE 3.2
VARIATION OF EEC PARAMETERS FOR ACID LEACHING

Acid loss (g)	*RΩ (Ω)*	*ΔRΩ (Ω)*	*Rct (Ω)*	*ΔRal (Ω)*	*Cct (F)*	*ΔCal (F)*	*Rgt (Ω)*	*ΔRam(Ω)*	*Cgt (F)*	*ΔCam (F)*
0	0.00310	-	0.00192	-	4.73024	-	0.00159	-	26.8731	-
0.5543	0.00505	0.00194	0.00439	0.00247	0.81238	-3.91787	0.00303	0.00144	16.3399	-10.5332
0.6003	0.00658	0.00347	0.00467	0.00275	0.74183	-3.98841	0.00331	0.00171	13.5842	-13.2889
0.6718	0.01099	0.00788	0.00629	0.00436	1.52776	-3.20248	0.00365	0.00205	13.9568	-12.9163
0.8043	0.01832	0.01521	0.00733	0.00541	0.90737	-3.82288	0.00568	0.00409	6.29923	-20.5739

A critical point of change for the MEA was found to be at a PA loss of 14%wt or 0.55g where the ohmic resistance started to increase dramatically as a result of surface area contact loss with the bipolar plates and decreased membrane ionic conductivity. The change of the MEA structure and subsequent increase in resistance is not proportional to acid loss. The curves presented in Fig. 3.18 and Fig. 3.19 demonstrate that the loss in performance is not only due to the acid loss, causing reduced ionic conductivity of the PBI membrane, but also MEA morphology changes as a result of the acid migration.

The variation of R_{ct} and R_{gt} is shown in Fig. 3.19 and indicates an increase in resistances for reduced acid content in the MEA. The changes in capacitance for the two sub-circuits are presented in Fig. 3.20 and depict an almost linear decrease in magnitude. This results from the loss in electrolyte thereby reducing the amount of charge that can be stored in the respective layers of the MEA. Due to the measurement procedure requiring that the MEA be removed, the capacitive elements exhibit some inconsistencies between the 0.6g and 0.7g loss measurement intervals. However, the general trend can be assumed to be linearly decreasing in magnitude for the EEC based on the result set presented.

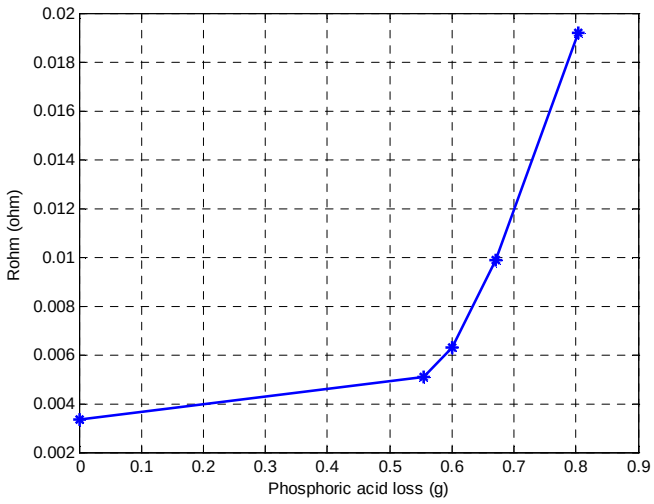

Figure 3.18. Membrane and contact resistance vs PA loss.

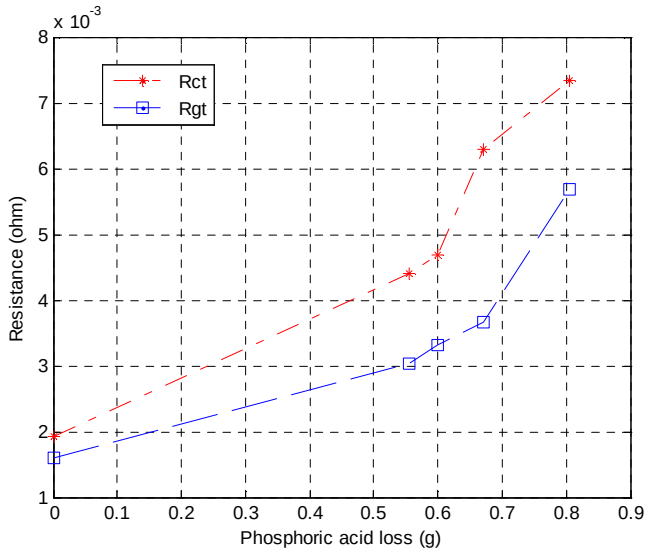

Figure 3.19. Resistance vs PA loss.

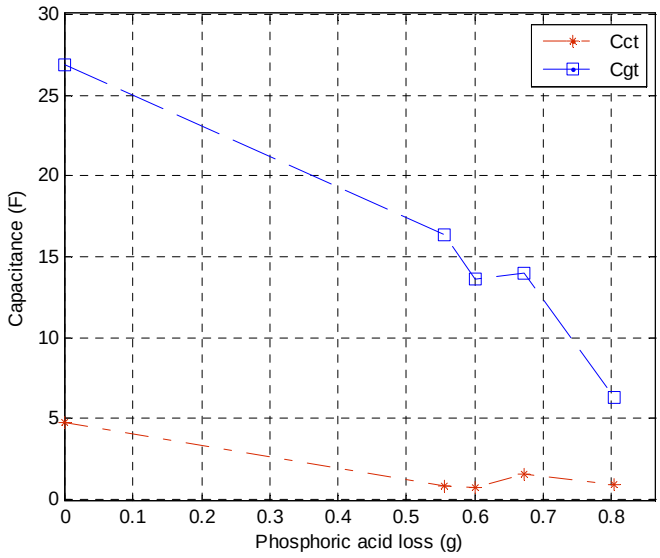

Figure 3.20. Capacitance vs PA loss.

3.6.4 Carbon/Catalyst Degradation Circuit Variations

The stability of platinum catalyst on carbon black under high operating temperatures has been the focus of a number of works, [20], [25]-[28]. The enhanced electrochemical kinetics accelerate the degradation that takes place through a number of mechanisms. The most important of these mechanisms include the platinum sintering, agglomeration and the corrosion of the carbon support. During the manufacturing process, the platinum is finely dispersed across carbon particles that act as the support structures. This increases the effective electrocatalytic surface area of the platinum that facilitates the reactions in the

anode and cathode. At elevated temperatures the degradation of the carbon black is accelerated and results in a drop in the effective surface area of the platinum. In an operational fuel cell, the platinum can break free from the carbon and dissolve into the electrolyte or the particles can bond with adjacent platinum, which causes agglomeration. This degradation mechanism also reduces the effective surface area available at the reaction sites.

The above mentioned mechanisms are enforced by operating the fuel cell in a certain manner. Long term aging studies have confirmed that prolonged operation at open circuit voltage (OCV) or similar high potentials can enforce the corrosion rate of the carbon based catalysts [25], [26], [28]. High potential or potential cycling weakens the interaction of the platinum and carbon and enforces agglomeration. The frequency of the potential cycling has also been the focus of recent studies along with the waveform applied. This effect can be caused by the low or high frequency current ripple on the primary side of the power electronic converters connected to the fuel cells [27]. The degradation of the carbon support is severely accelerated under extreme fuel starvation where the cell potential can be reversed [28], [31].

In this work the degradation of the catalyst layer and carbon support was accelerated for a short period of 24 hours to identify the primary change in the equivalent circuit parameters. After run-in, polarization curves, EIS and CV were performed. The cell was then left at an operating temperature of 160°C at OCV for 24 hours with the anode and cathode flows shut down. This procedure forced the cell to stay at a high potential while starving the catalyst layers in order to enforce the main catalyst and carbon degradation mechanisms. After 24 hours the fuel flows were restarted and the diagnostic tests were repeated. The polarization curves at 140°C and 180°C for the new and degraded MEA are presented in Fig. 3.21. The loss in performance is clearly visible and is more profound at the higher operating temperature. The Nyquist plots recorded via EIS along the polarization curves are presented in Fig. 3.22. There is a small variation in the ohmic resistance for the change in current density that can be attributed to the low SNR at the high frequencies and can be ignored. The most significant change takes place in the low frequency arc that represents the gas transport resistance. This indicates that a substantial amount of carbon corrosion took place both in the gas diffusion layers and possibly the catalyst layers. The change to the effective electrocatalytic surface area (ECSA) was

determined via cyclic voltammetry and the results are shown in Fig. 3.23. For the short period of OCV under starved conditions, changes to the ECSA are visible as a reduction in surface area of the voltammogram.

The change to the EEC for catalyst/carbon degradation is shown in Fig. 3.24. The drop in the ECSA will result in small changes to the effective charge transfer resistance that can be ignored for short time operation fault diagnostics. The catalyst/carbon degradation of the MEA is captured as ΔR_{cd} in the gas transport sub-circuit and the change to capacitance as ΔC_{cd}. The variation in circuit parameter values are presented in table 3.3. The variation in the gas transport capacitance, ΔC_{cd}, is negative, allowing it to be distinguished from reactant starvation when performing diagnostics.

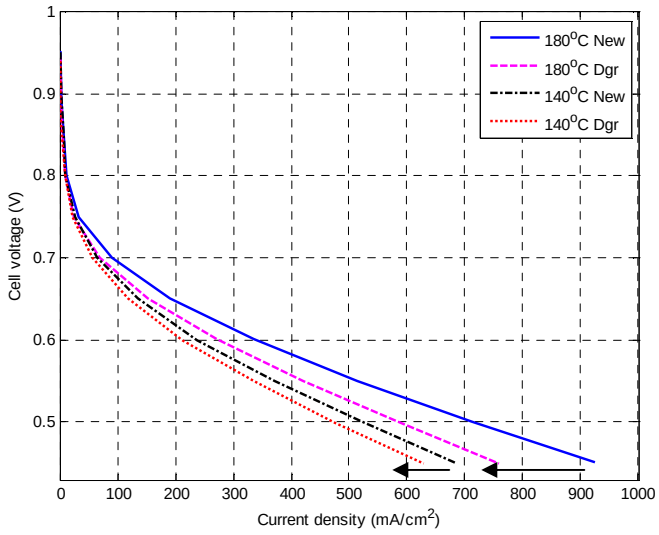

Figure 3.21. Effect of OCV on cell performance.

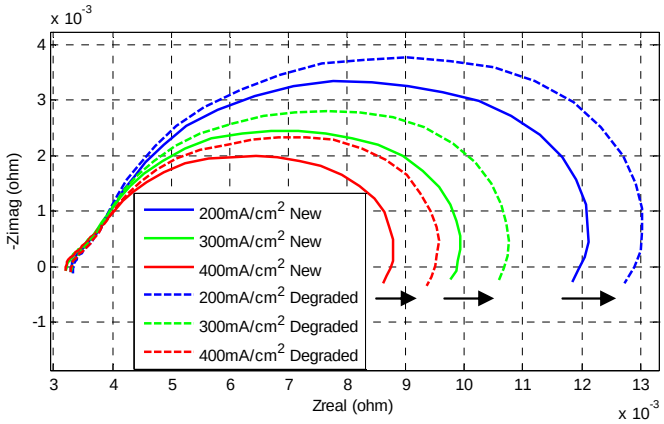

Figure 3.22. Effect of OCV on cell impedance.

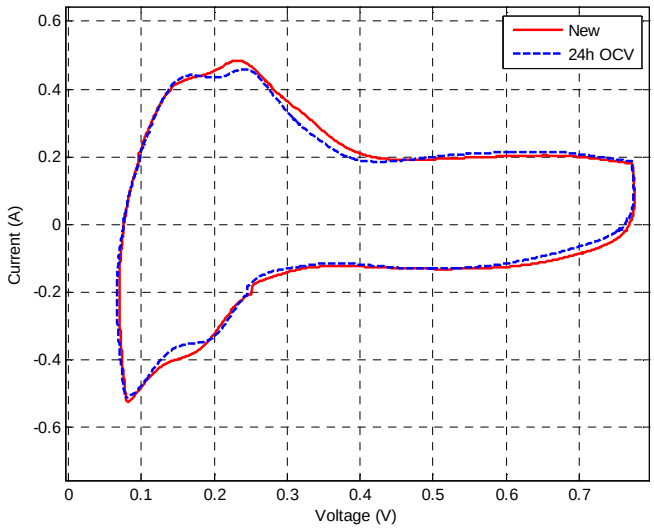

Figure 3.23. Effect of OCV on cell ECSA.

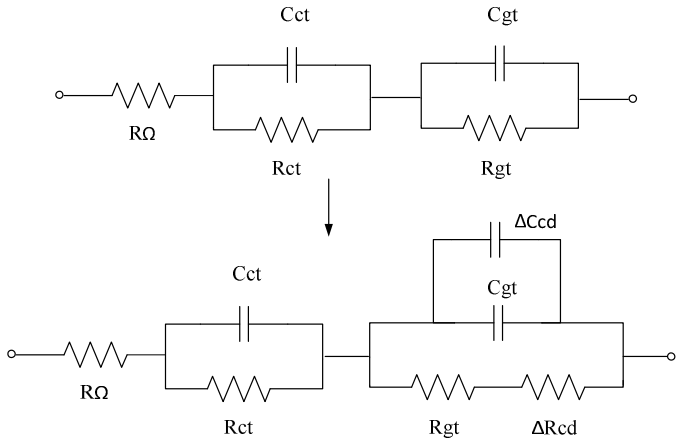

Figure 3.24. Variation in the EEC for catalyst/carbon degradation.

TABLE 3.3
VARIATION OF EEC PARAMETERS FOR CARBON/CATALYST DEGRADATION

RΩ (Ω)	*Rct (Ω)*	*Cct (F)*	*Rgt (Ω)*	*ΔRcd (Ω)*	*Cgt (F)*	*ΔCcd (F)*
			200mA/cm^2			
0.00329	0.00365	5.10475	0.00496	-	15.5006	-
0.00334	0.00337	5.73514	0.00625	0.00129	13.3949	-2.10574
			300mA/cm^2			
0.00321	0.00273	5.03394	0.00376	-	16.1361	-
0.00330	0.00270	5.77274	0.00466	0.00090	15.0612	-1.07492
			400mA/cm^2			
0.00320	0.00215	4.82993	0.00323	-	15.3518	-
0.00329	0.00207	5.71473	0.00406	0.00083	13.9826	-1.36917

3.6.5 CO Poisoning Circuit Variations

The increased tolerance towards certain poisoning elements that may be introduced to the hydrogen gas stream makes HT-PEM fuel cells a very attractive solution for standalone reformer fed applications. By reforming natural gas or hydrocarbons, CO is produced as a by-product and must typically be removed for low temperature PEM fuel cells to function. The increased temperature of HT-PEM fuel cells can tolerate up to 3% CO at 200°C in the anode [2] thereby allowing the scrubbing phase in the reformer to be removed and the system cost reduced. Despite the increased tolerance towards CO poisoning, high concentrations can still severely affect the performance. During start-up, a reformer can exhibit sudden increases in the output CO concentration that must be monitored.

The CO poisoning investigations were conducted on the custom test bench to enable steady state and transient analysis. For the purpose of classification, the results for a typical operating temperature of 170°C for the HT-PEM fuel cell is presented in this chapter. Detailed investigations on the phenomena that will enable the estimation of the extent of CO poisoning, including the mitigation strategies, will be presented in chapter 5 of this thesis. The polarization curves for variations in CO concentration at the 170°C operating point are presented in Fig. 3.25 and the corresponding EIS in Fig. 3.26. The drop in performance for the increased CO concentration is evident. As CO is introduced it is adsorbed onto the platinum, which reduces the effective surface area available for the reaction.

Initially, there is a large increase in the diameter of the mid frequency arc as the surface coverage of the CO on the catalyst increases. For the very high concentrations, the low frequency arc representing the gas transport resistance starts to increase due to the non-reacting competing species. The EEC is affected in both the charge transport and gas transport sub-circuits and the additional resistances ΔR_{cp} and ΔR_{co} representing the catalyst poisoning resistance and CO resistance are introduced, as shown in Fig. 3.27. The variation of the component values for changes in CO concentration are presented in table 3.4 for the purpose of fault classification.

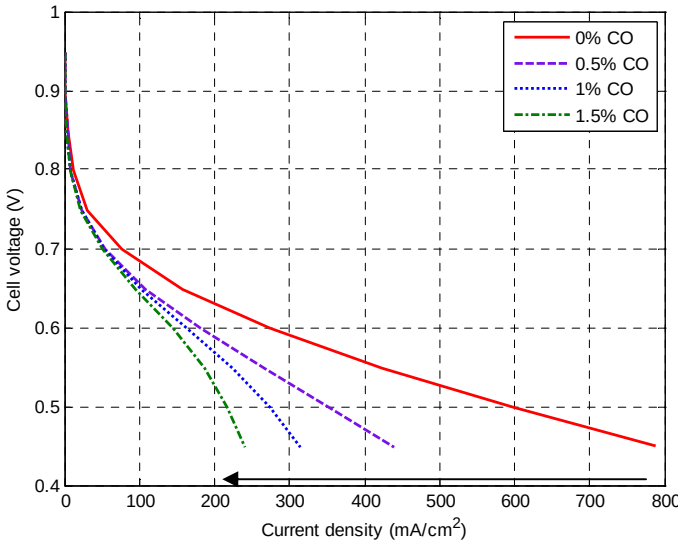

Figure 3.25. Polarization curves for different CO concentrations.

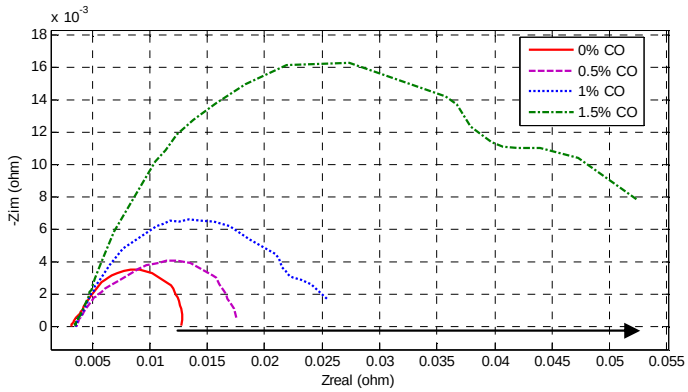

Figure 3.26. Effect of catalyst poisoning on cell performance.

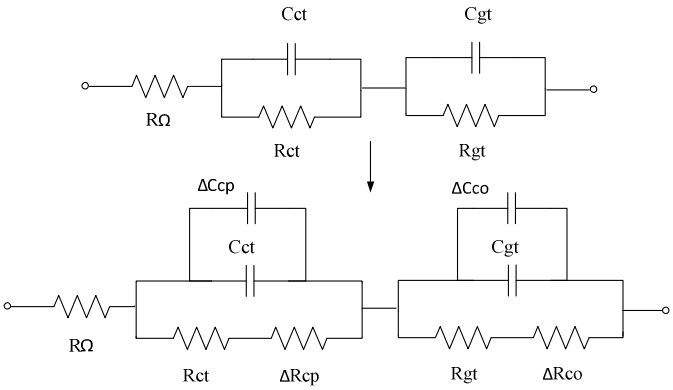

Figure 3.27. Variation in the EEC for catalyst poisoning.

TABLE 3.4
VARIATION OF EEC PARAMETERS FOR CO POISONING

CO (%)	*RΩ (Ω)*	*Rct (Ω)*	*ΔRcp (Ω)*	*Cct (F)*	*ΔCcp (F)*	*Rgt (Ω)*	*ΔRco (Ω)*	*Cgt (F)*	*ΔCco (F)*
0	0.00325	0.00386	-	3.90295	-	0.00540	-	13.9419	-
0.5	0.00362	0.00528	0.00142	1.14813	-2.75482	0.00751	0.00211	9.63699	-4.30491
1	0.00355	0.01424	0.01037	1.54874	-2.35421	0.00556	0.00016	48.4546	34.5127
1.5	0.00347	0.03216	0.02829	1.76430	-2.13865	0.01632	0.01092	46.2332	32.2913

3.6.6 Fault Classification Matrix for Diagnostics

The faults can be classified using the fault classification matrix presented in table 3.5. Each of the faults yields a unique combination of parameter variations. Comparing the reactant starvation and carbon degradation faults shows variations in the same parameters. There is, however, a unique change in the gas transport capacitance. For the starvation phenomenon, the effective capacitance will increase by ΔC_{fs} while the carbon degradation phenomena will yield a drop in capacitance by ΔC_{cd}. A similar comparison can be made between the acid leaching and catalyst poisoning faults. Even though variations in the charge transfer and gas transport sub-circuits follow roughly similar trends, only acid leaching will yield a change in the membrane and ohmic resistance.

It is clear that monitoring the impedance at a single frequency or the drop in output power using the polarization curves alone does not provide adequate information for fault classification. By using the impedance spectrum and the proposed equivalent circuit analysis it is possible to isolate a specific fault for rapid online fault diagnostics. Studies done on rapidly occurring faults, such as catalyst poisoning, have yielded detailed impedance signature maps [22], [32]. These maps can be integrated with the proposed fault classification matrix and an observer based diagnostics system that interfaces with the master control of the fuel cell. By monitoring the identified circuit parameters in the model, the fault can be identified and possible mitigation strategies employed. This will increase not only the performance of the system but also the life expectancy of the cell by limiting component degradation.

TABLE 3.5
VARIATION OF EEC FOR INDIVIDUAL FAULT MECHANISMS

	Starvation	*Acid Leaching*	*Carbon Deg*	*Cat Poisoning*
RΩ	-	*ΔRΩ (+ ↑)*	-	-
Rct	-	*ΔRal (+ ↑)*	-	*ΔRcp (+ ↑)*
Cct	-	*ΔCal (- ↓)*	-	*ΔCcp (- ↓)*
Rgt	*ΔRfs (+ ↑)*	*ΔRam (+ ↑)*	*ΔRcd (+ ↑)*	*ΔRco (+ ↑)*
Cgt	*ΔCfs (+ ↑)*	*ΔCam (- ↓)*	*ΔCcd (- ↓)*	*ΔCco (+ ↑)*

Conclusion

This chapter presents the changes in the electrochemical equivalent circuit and performance of an HT-PEM fuel cell under normal operating conditions and for four major degradation mechanisms. Specific consideration is given to the fault condition known as acid leaching. Tracking these changes is vital for the purpose of condition monitoring in a functioning fuel cell and can be used to increase the performance and life expectancy of the system. A new method is developed to accelerate acid loss in an assembled MEA by running the system in driven cell mode. It is shown that there is a distinct variation in equivalent circuit parameters for differences in MEA acid content via EIS. The loss in output power is clearly identifiable and shows the effect this condition has on the fuel cell performance.

It is shown that loss of PA acid had a significant effect on the ionic conductivity of the membrane as well as charge transfer resistance while proton conduction is heavily influenced, resulting in the drop in performance. The drop in performance is non-linear with respect to the acid loss due to a number of factors. The causes of fuel starvation, catalyst degradation and CO poisoning are discussed. Each mechanism was individually introduced to the fuel cell and diagnostics performed to isolate the resulting changes in the EEC. A fault classification matrix is developed in order to provide a basis for fault classification in an operational HT-PEM fuel cell system.

References

[1] Hui Li et al., "A review of water flooding issues in the proton exchange membrane fuel cell*." Journal of Power Sources*, Vol 178, pp 103-117, 2008.

[2] Jianlu Zang et al., "High Temperature PEM Fuel Cells", *Journal of Power Sources*, Vol. 160, pp 872-892, 2006.

[3] C. Seel, B. C. Benicewicz, L. Xiao and T. J. Schmidt, High-temperature polybenzimidazole-based membranes. In: Wolf Vielstich, Harumi Yokokawa, Hubert A. Gasteiger, editors. Handbook of Fuel Cells – Fundamentals, Technology and Applications, John Wiley & Sons, Ltd. 2009.

[4] Jianlu Zang, Yanghua Tang, Chaojie Song and Jiujun Zang, "Polybenzimidazole membrane based PEM fuel cell in the temperature range of 120°C-200°C", *Journal of Power Sources*, Vol. 172, pp. 163-171, 2007.

[5] Su, Y.M. Ferng, J. Hou, T.L. Yu, "Experimental and numerical investigations of the effects of PBI loading and operating temperature on a high-temperature PEMFC", *International Journal of Hydrogen Energy*, Vol. 37 pp. 7710-7718, 2012.

[6] Justo Lobato, Pablo Canizares, Manuel A. Rodrigo, Jose´ J. Linares, F. Javier Pinar, "Study of the influence of the amount of PBI–H3PO4 in the catalytic layer of a high temperature PEMFC", *International Journal of Hydrogen Energy*, Vol. 35, pp. 1347-1355, 2010.

[7] Christoph Wannek, Irene Konradi, Ju¨rgen Mergel, Werner Lehnert, "Redistribution of phosphoric acid in membrane electrode assemblies for high-temperature polymer electrolyte fuel cells", *International Journal of Hydrogen Energy*, vol. 34, pp. 9479 – 9485, 2009.

[8] Christoph Wannek,Werner Lehnert, Jürgen Mergel, "Membrane electrode assemblies for high-temperature polymer electrolyte fuel cells based on poly(2,5-benzimidazole) membranes with phosphoric acid impregnation via the catalyst layers", *Journal of Power Sources* , vol.192, pp. 258–266, 2009.

[9] F. Liu, S.Mohajeri, Y. Di, K.Wippermann,W. Lehnert, "Influence of the Interaction Between Phosphoric Acid and Catalyst Layers on the Properties of HT-PEFCs", *FUEL CELLS*, Available online.

[10] Ronghuan He, Qingfeng Li, Anders Bach, Jens Oluf Jensen, Niels J. Bjerrum, "Physicochemical properties of phosphoric acid doped polybenzimidazole membranes for fuel cells", *Journal of Membrane Science* ,Vol. 277, Issues 1–2, pp. 38–45, 1 June 2006.

[11] Yuka Oono, Atsuo Sounai, Michio Hori, "Influence of the phosphoric acid-doping level in a polybenzimidazole membrane on the cell performance of high-temperature proton exchange membrane fuel cells", *Journal of Power Sources* , vol. 189, pp. 943–949, 2009.

[12] Seonghan Yu and Brian C. Benicewicz," Synthesis and Properties of Functionalized Polybenzimidazoles for High-Temperature PEMFCs", *Macromolecules*, Vol. 42, pp. 8640-8648, 2009.

[13] Jingwei Hua, Huamin Zhanga, Yunfeng Zhaia, Gang Liua, and BaolianYia, "500 h Continuous aging life test on PBI/H3PO4 high-temperature PEMFC", *International Journal of Hydrogen Energy*, Vol. 31, pp.1855-1862, 2006.

[14] Modestov, M.R. Tarasevich, V.Ya. Filimonov and N.M. Zagudaeva, "Degradation of high temperature MEA with PBI-H3PO4 membrane in a life test", *Electrochimica Acta*, Vol. 54 pp. 7121–7127, 2009.

[15] Yunfeng Zhai, Huamin Zhang, Gang Liu, Jingwei Hu and Baolian Yia," Degradation Study on MEA in H3PO4/PBI High-Temperature PEMFC Life Test*", Journal of The Electrochemical Society*, Vol. 154, pp. B72-B76, 2007.

[16] Zhigang Qi and Steve Buelte, "Effect of open circuit voltage on performance and degradation of high temperature PBI–H3PO4 fuel cells*", Journal of Power Sources*, Vol. 161, pp. 1126-1132, 2006.

[17] Ji-Rae Kim, Jung S. Yi, Tae-Won Song, "Investigation of degradation mechanisms of a high-temperature polymer-electrolyte-membrane fuel cell stack by electrochemical impedance spectroscopy*", Journal of Power Sources*, vol. 220, pp.54-64, 2012.

[18] C. de Beer, P.S. Barendse, P. Pillay, B. Bullecks and R. Rengaswamy, "Degradation of High Temperature PEM Fuel Cells and the Impact on Electrical Performance*", IEEE International Conference on Industrial Technology (ICIT)*, Cape Town, 2013.

[19] Eliana Quartarone and Piercarlo Mustarelli, "Polymer fuel cells based on polybenzimidazole/H3PO4", *Energy Environ. Sci.*, Vol. 5, pp. 6436-6444, 2012.

[20] Farhana S. Saleh and E. Bradley Easton, "Diagnosing Degradation within PEM Fuel Cell Catalyst Layers Using Electrochemical Impedance Spectroscopy", *Journal of The Electrochemical Society*, vol. 159, no. 5, pp. B546-B553, 2012.

[21] Xiaozi Yuan, HaijiangWang, Jian Colin Sun and Jiujun Zhang, "AC impedance technique in PEM fuel cell diagnosis—A review", *International Journal of Hydrogen Energy*, Vol. 32, pp. 4365-4380, 2007.

[22] Søren Juhl Andreasen, Jakob Rabjerg Vang and Søren Knudsen Kær, "High temperature PEM fuel cell performance characterization with CO and CO2 using electrochemical impedance spectroscopy", *International Journal of Hydrogen Energy*, Vol. 36, pp. 9815-9830, 2011.

[23] Dhirde A.M., Dale N.V., Salehfar H., Mann M.D. and Han T.H., "Equivalent Electric Circuit Modeling and Performance Analysis of a PEM Fuel Cell Stack Using Impedance Spectroscopy," *IEEE Transactions on Energy Conversion*, vol.25, no.3, pp. 778-786, Sept. 2010.

[24] Alex Bates , Santanu Mukherjee , Sunwook Hwang, Sang C. Lee, Osung Kwon ,Gyeung Ho Choi , Sam Park, "Simulation and experimental analysis of the clamping pressure distribution in a PEM fuel cell stack", *International Journal of Hydrogen Energy* , vol. 38, pp. 6481 -6493, 2013.

[25] L. N. Cleemann, "Catalyst Degradation in High Temperature Proton Exchange Membrane Fuel Cells Based on Acid Doped Polybenzimidazole Membranes", *FUEL CELLS*, vol. 13, No. 5, pp. 822–831, 2013.

[26] Yunfeng Zhai, Huamin Zhang, Danmin Xing, Zhi-Gang Shao, "The stability of Pt/C catalyst in H3PO4/PBI PEMFC during high temperature life test", *Journal of Power Sources* , vol. 164, pp. 126–133, 2007.

[27] Jonghoon Kim, Jaemoon Lee, and B. H. Cho , "Equivalent Circuit Modeling of PEM Fuel Cell Degradation Combined With a LFRC", *IEEE Transactions on Industrial Electronics*, Vol. 60, No. 11, November 2013.

[28] Shengsheng Zhanga, Xiao-Zi Yuana, Jason Ng Cheng Hina, Haijiang Wanga,K. Andreas Friedrich, Mathias Schulze, "A review of platinum-based catalyst layer degradation in proton exchange membrane fuel cells", *Journal of Power Sources*, vol. 194, pp. 588–600, 2009.

[29] Fabrizio Marignetti, Mariagiovanna Minutillo, Alessandra Perna, and Elio Jannelli, "Assessment of Fuel Cell Performance Under Different Air Stoichiometries and Fuel Composition", *IEEE Transactions on Industrial Electronics*, Vol. 58, No. 6, June 2011.

[30] Carlos Restrepo et al, "Simplified Mathematical Model for Calculating the Oxygen Excess Ratio of a PEM Fuel Cell System in Real-Time Applications", *IEEE Transactions on Industrial Electronics*, Vol. 61, No. 6,June 2014

[31] M.A. Travassos, Vitor V. Lopes, R.A. Silva, A.Q. Novais, C.M. Rangel, "Assessing cell polarity reversal degradation phenomena in PEM fuel cells by electrochemical impedance spectroscopy", *International Journal of Hydrogen Energy*, vol. 38, pp. 7684-7696, 2013.

[32] C. de Beer, P.S. Barendse, P. Pillay, B. Bullecks and R. Rengaswamy, "Electrical Circuit Analysis of CO Poisoning in High Temperature PEM Fuel Cells for Rapid Fault Diagnostics", *IEEE Energy Conversion Congress and Expo (ECCE)*, Denver Colorado, 2013.

[33] Kyungjung Kwon, Jung Ock Park, Duck Young Yoo, Jung S. Yi, "Phosphoric acid distribution in the membrane electrode assembly of high temperature proton exchange membrane fuel cells", *Electrochimica Acta*, vol. 54, Issue 26, pp. 6570-6575, November 2009.

Chapter 4

Modelling and Emulation of Performance Degradation

4.1 Introduction

HT-PEM fuel cell degradation was studied in chapter 2 and 3. Since platinum catalyst on carbon support is used in both LT-PEM and HT-PEM fuel cells, the degradation phenomena of these materials are similar. Research has, however, proven that the higher operating temperature enforces catalyst and carbon degradation and should thus be accounted for accordingly [1]. Water management faults, such as flooding and drying in LT-PEM fuel cells, has been studied extensively in literature and some methods that try and reduce these effects have been proposed but can never be completely eliminated. These problems are no longer present in HT-PEM systems but due to the acid doping requirement, acid leaching can occur [2]. Other advantages include the ability to use hydrogen generated from a reformer that includes impurities, such as CO. However, high concentrations of these impurities can severely affect performance and should also be taken into account [3]. The degradation mechanisms are dependent on the operation of the fuel cell. In most systems, the fuel cell is connected to a power electronic interface module to regulate the output DC voltage and invert to AC if required. The converter generates low and high frequency current ripple at the fuel cell output that contributes to catalyst degradation. Research has been focused on reducing the magnitude of the ripple

component by adapting the control philosophy or the topology of the power electronics [4], [5].

In order to design power electronics and control systems, fuel cell models and equivalent circuit models are used to predict what the output will be under certain operating conditions [6]-[8]. These models can be integrated into emulator hardware to replace the actual fuel cell and limit development costs when prototyping. Previous research has focused on HT-PEM electrochemical models but very little has been done to incorporate the degradation of more than one mechanism that can arise from extreme operating conditions while also exploring the impact of power electronic switching on the rate of degradation. Almost no circuit models for HT-PEM degradation are available as the systems are not yet fully commercialized [9]. The first part of this chapter presents the development of an electrochemical semi-empirical analytical and electrical circuit model that incorporates the main degradation effects for HT-PEM fuel cells. The models can be used to determine optimal operational requirements to maximize output power and increase life expectancy.

A fuel cell emulator is a hardware platform that is able to mimic the behaviour of an actual fuel cell system. Fuel cell emulators allow for the variation of parameters in real time to evaluate and facilitate subsystem development without the need of the actual fuel cell. This reduces the need for the use of the expensive electrochemical systems and allows developers to perform hardware in the loop testing under fault conditions, which is the focus of the work presented in the second part of this chapter. By emulating the electrical behaviour under fault conditions, mitigation strategies can be developed that will increase the performance and the life expectancy of the fuel cells and improve the success for commercialization. Current emulator systems focus on normal operating conditions and are limited when reproducing the voltage and current behaviour during transients [10]-[16].

The electrochemical model and associated circuit elements for the HT-PEM fuel cell are presented in section 4.2. The proposed hardware for the real time emulator platform is presented in section 4.3 and 4.4. The model is validated in section 4.5 where simulation and experimental results are presented for the experimental fuel cells and emulator systems. Results are presented for life cycle and performance estimation based on varying operating conditions. Finally, conclusions are drawn and the results commented upon.

4.2 HT-PEM Fuel Cell Model

The fuel cell model is semi-empirical with the standard elements derived from electrochemical relations. The model takes into account the three main degradation mechanisms that contribute to performance drop, as identified in chapter 3. These include catalyst degradation, CO poisoning, and acid leaching. The impact of ripple frequency on the performance loss also forms part of the model development. The parameters affected by each degradation or fault type are identified and the effect of the mechanism is modelled accordingly. This section presents the expressions relating to these mechanisms and the equivalent circuit elements that can be used to represent the effects.

4.2.1 Steady State

The cell voltage can be represented as follows:

$$E_{cell} = E_{rev} - \eta_{act} - \eta_{ohm} - \eta_{conc} \tag{4.1}$$

Where η represents the voltage loss components and E_{rev} the reversible open circuit voltage that can be calculated using the Nernst equation:

$$E_{rev} = \frac{-\Delta g_{nrx}^{ref}}{nF} + \frac{\Delta S}{nF}\left(T_{cell} - T_{ref}\right) - \frac{RT_{cell}}{nF} ln\left(\frac{p_{H_2} p_{O_2}^{0.5}}{p_{H_2O}}\right) \tag{4.2}$$

The first term in (4.2) is related to the Gibbs free energy of the system and can be taken as a constant value of 1.185V for the temperature range under investigation, 100°C to 200°C. The second term relates to the entropy of the system where the reversible potential is adjusted for temperature variations. The last term adjusts the reversible potential for concentration variations. In this work, T_{cell} refers to the temperature in Kelvin, n the number of electrons taking place in the reaction, R is the gas constant, F is Faradays constant and p represents the partial pressures of the individual gas species. The entropy change, ΔS, for high temperature operation where water is in vapour form can be represented as follows [17]:

$$\frac{\Delta S}{n} = -48.119 - 0.01283T_{cell} \tag{4.3}$$

In most circuit models, the open circuit voltage is represented by a variable voltage source where temperature and pressures are taken as the input parameters.

The second term in (4.1) represents the first voltage loss component that forms part of the reaction, namely the activation voltage loss, η_{act}. The activation voltage loss represents the finite amount of energy required for the reaction to take place and represents the part of the model relating to the reaction or catalyst layer. It is this loss component that must reflect catalyst degradation caused by various effects and catalyst coverage caused by CO poisoning. Typically, only the cathode catalyst layer is included in the model as the reaction rate at the anode is assumed to be much faster and thus contributing minimally to the loss component. As CO is introduced into the anode gas feed, this component can no longer be excluded from the model as the adsorption of CO now affects the effective surface area of the catalyst. For this model, we will assume that the catalyst layer acts as an interface in order to simplify the equation set. This assumes that the catalyst layer is infinitely thin and situated between the gas diffusion layer and the membrane. More advanced models, such as micro-porous models that are used to model flooding in low temperature PEM can be ignored due to the HT operation. The activation voltage loss is thus expanded as follows:

$$\eta_{act} = \eta_{act,a} + \eta_{act,c} \tag{4.4}$$

The reactions at the anode and the cathode can be modelled using the Butler-Volmer relationship:

$$i_a = i_0^a \left[exp\left(\alpha_a \frac{nF\eta_{act,a}}{RT_{cell}}\right) - exp\left(-\alpha_c \frac{nF\eta_{act,a}}{RT_{cell}}\right)\right] \tag{4.5}$$

$$i_c = i_0^c \left[exp\left(-\alpha_a \frac{nF\eta_{act,c}}{RT_{cell}}\right) + exp\left(\alpha_c \frac{nF\eta_{act,c}}{RT_{cell}}\right)\right] \tag{4.6}$$

Where *i* represents the reaction current density at the anode or cathode side and α the charge transfer coefficient at the anode or cathode side. By assuming that the second term in the expression in the anode side and the first term in the expression for the cathode side is negligible and solving for the voltage loss yields [18]:

$$\eta_{act,j} = \frac{RT_{cell}}{\alpha_j nF} ln\left(\frac{i_j}{{i_0}^j}\right) \tag{4.7}$$

Where *j* represents the respective variable at the anode or cathode side. These voltage loss components can be represented by a diode model and will be discussed in the following section. The exchange current density i_0 is a function of temperature and reactant partial pressure at the reaction sites. This parameter gives an indication of the rate of the reaction and influences the activation over-potential. The exchange current density is also dependant on the effective catalyst surface area. Therefore, this parameter will be influenced by degradation mechanisms, such as CO poisoning and catalyst degradation. The exchange current densities are represented as follows:

$$i_0^c = i_o^{c,ref} S_{eff,c} \left(\frac{p_{O_2}}{P_{O_2}^0}\right)^{\gamma} exp\left[\frac{-E_c}{RT}\left(1 - \frac{T_{cell}}{T_{ref}}\right)\right] \tag{4.8}$$

$$i_0^a = i_o^{a,ref} S_{eff,a} \left(\frac{p_{H_2}}{P_{H_2}^0}\right)^{\gamma 1} \left(\frac{p_{H_2O}}{P_{H_2O}^0}\right)^{\gamma 2} exp\left[\frac{-E_a}{RT}\left(1 - \frac{T_{cell}}{T_{ref}}\right)\right] \tag{4.9}$$

Where i_0^{ref} represents the reference exchange current densities, S_{eff} the effective catalyst surface area, γ the reaction orders and E the activation energy at the anode and cathode respectively.

The partial pressures of the individual gas species at the reaction sites are dependent on the diffusion through the gas diffusion layer, micro porous layer and the catalyst layer. Using the Stefan-Maxwell relation for multicomponent diffusion and a Knudsen diffusion term, the mass transport resistances can be modelled as series components as follows:

$$\nabla p_i = \sum_{j \neq i} \frac{RT_{cell}}{p_G D_{i,j}} \left(p_i N_j - p_j N_i\right) - \frac{RT_{cell}}{D_{k,i}} N_i \tag{4.10}$$

Where p_i is the partial pressure of species *i*, D_{ij} is the effective binary diffusion coefficient between two species, N is the molar flux of the individual gas species and p_G is the total gas-phase pressure. The second term represents the Knudsen diffusion and represents the interaction between the molecules of the individual species and the pore walls of the medium [19]. The Knudsen diffusion coefficient is determined as follows:

$$D_{k,i} = \frac{e}{\tau}\left(\frac{8RT_{cell}}{\pi M_i}\right)^{1/2} \frac{2}{3} r_p \tag{4.11}$$

Where M_i is the molar mass of the gas species, e and τ are the porosity and tortuosity of the porous medium and r_p is the mean pore radius.

4.2.2 Surface Area Loss

The parameter that is affected during catalyst degradation is the effective surface areas, S_{eff}. Since the degradation mechanism is highly dependent on operating conditions, an empirical expression is used. In the results presented in [20], the effect of ripple frequency on cell performance is studied. The authors did, however, not specify what the internal effect is on the cell components. It is known from other works [21], [22], that variation in current enforces catalyst agglomeration thereby reducing the effective surface area in the model. It is thus possible to incorporate this effect into the empirical expression. An exponential and polynomial expression was fitted onto experimental data presented in [21] that relates catalyst degradation in the cathode to temperature and operating time.

$$S_{deg,c} = S_{new,c}[(1 - \beta_1 exp(\beta_2 T_{cell} i_{cell}))t + \beta_3 T_{cell} + \beta_4 i_{cell}] \tag{4.12}$$

To extend the functionality of the model, however, the effect of the load current ripple frequency has also been included. An expression that incorporates the effect can be written as follows:

$$S_{eff,c} = S_{deg,c}\left(1 - \frac{\beta_5}{log(\omega)}t\right) \tag{4.13}$$

Where S_{new} is the effective surface area of a new cell, ω the frequency of the ripple component and β the respective coefficients used to fit experimental data. In addition to catalyst degradation, the surface coverage of the catalyst at the anode due to CO poisoning must be added. The effective catalyst surface area can be expressed as follows for CO coverage of the platinum in HT-PEM fuel cells:

$$S_{eff,a} = S_{new,a}(1 - \theta_{CO}) \tag{4.14}$$

where θ_{CO} represents the catalyst surface coverage due to CO in the anode. A number of attempts have been made to model these analytically using different isotherms for the CO adsorption onto the platinum [23], [24]. These models are, however, extremely complex

and computationally expensive. In general, hydrogen and CO adsorption/desorption can be modelled using Temkin, Frumkin or Langmuir kinetics. By using the Langmuir isotherm for the hydrogen and CO kinetics, the adsorption rates can be calculated as follows [24]:

$$q_H^{ads} = k_H^{ads} c_H (1 - \theta_H - \theta_{co})^2 - b_H^{ads} k_H^{ads} (\theta_H)^2 \tag{4.15}$$

$$q_{co}^{ads} = k_{co}^{ads} c_{co} (1 - \theta_H - \theta_{co})^2 - b_{co}^{ads} k_{co}^{ads} (\theta_{co})^2 \tag{4.16}$$

Where k and b are pre-exponential factors fitted onto experimental data. The electro-oxidation rate of hydrogen can be related to the current density in the anode as follows:

$$q_H^{eox} = \frac{i_a}{F} \tag{4.17}$$

The coverage of the Hydrogen and CO on the catalyst sites are a function of time. For steady state conditions, the following is assumed:

$$\frac{d\theta_H}{dt} = q_H^{ads} - q_H^{eox} = 0 \tag{4.18}$$

$$\frac{d\theta_{co}}{dt} = q_{co}^{ads} = 0 \tag{4.19}$$

By using the above relations, the coverage of CO as a function of current density and gas concentration is obtained:

$$\theta_{co} = \left(\frac{i_a}{F} \frac{c_{co}}{k_H c_{H2}} \right)^{1/2} \tag{4.20}$$

An empirical expression for catalyst coverage based on experimental data for low temperature PEM fuel cells was presented in [3]. This can be modified to reflect HT operation and the subsequent reduction of CO adsorption at the elevated temperatures by using (4.20) to produce the following:

$$\theta_{CO} = \sigma_1 + \sigma_2 ln\left(1 + \frac{p_{CO}}{p_{H_2}}\right) + \sigma_3 \ln(1 + i_{cell}) + \sigma_4 T_{cell} \tag{4.21}$$

Where p represents the respective partial pressures of the species and σ the coefficients used to fit the experimental data for CO coverage.

4.2.3 Acid Loss

The final mechanism that can cause severe performance loss is acid leaching of the membrane [2]. The ohmic voltage loss of the membrane is expressed as follows:

$$\eta_{ohm,mem} = i_{cell}\frac{\delta_m}{k_m} = i_{cell}R_{mem} \tag{4.22}$$

Where δ_m represents the membrane thickness and k_m represents the conductivity of the membrane. To account for variations in cell temperature on conductivity, the Arrhenius law is used:

$$k_m = \frac{ab}{T_{cell}} exp\left(\frac{-E_{act,mem}}{RT_{cell}}\right) \tag{4.23}$$

Where a and b accounts for the acid content or doping level (DL) and E_{act} represents the activation energy of the PBI membrane [17]. For this model the following set of empirical expressions reported in literature will be used to model this effect and is based on extensive experimental work produced by [2], [17], and [22]:

$$a = 168DL^3 - 6324DL^2 + 65750DL + 8460 \tag{4.24}$$

$$b = 1 + (0.1432T_{cell} - 56.89)RH \tag{4.25}$$

$$E_a = -619.6DL + 21750 \tag{4.26}$$

The relative humidity, RH, can in most cases be set to zero due to the high operating temperature and the fact that the gas streams do not need to be humidified. The total ohmic resistance is a function of a number of mechanisms. In most models, however, this value is equated to the membrane resistance only as this is the largest contributor. When acid leaching occurs, the contact resistance between the GDL and the bipolar plates starts becoming substantial. In general, this resistance can be expressed as follows [18]:

$$R_{contact} = \frac{A_a K G^{D-1}}{\kappa L^D}\left[\frac{D}{(2-D)P^*}\right]^{D/2} \tag{4.27}$$

Where A_a is the contact area, K the geometric constant, G the topothesy of the surface profile, D the fractal dimension of the surface profile, L the length, κ the effective electrical conductivity of the two surfaces and P the dimensionless clamping pressure and compression modulus of the GDL [18].

4.2.4 Transients

During transient conditions, electrons and protons accumulate at the electrode and electrolyte interface. This acts as a capacitive element and will cause time delays in the activation overvoltage. For a short period, the reaction current will not be the same as the current drawn by the external load. This charge double layer effect is represented as follows [25]:

$$i_{cell} = i_{reac} + C_{cdl}\frac{d\eta_{act}}{dt} \tag{4.28}$$

Where the charge double layer capacitance, C_{cdl} can be expressed as follows [8]:

$$C_{cdl} = \varepsilon\frac{A}{dl} \tag{4.29}$$

In the above relationship, A represents the surface area of either the anode or the cathode, ε the permittivity and dl the distance between the two charge layers. The change in the partial pressures due to variations in load can be expressed as follows [6]:

$$\frac{dp_{H2}}{dt} = \frac{RT_{cell}}{V_a}\left[M_{H2,net} - \frac{i}{2F}\right] \tag{4.30}$$

$$\frac{dp_{O2}}{dt} = \frac{RT_{cell}}{V_c}\left[M_{O2,net} - \frac{i}{4F}\right] \tag{4.31}$$

In this work, the cell temperature is assumed to be constant. For stack level simulations, it is, however, required that the cooling mechanism be incorporated and the transient effect on the temperature during load changes. This can be done by incorporating the following relationship [9]:

$$C_t\frac{dT_{cell}}{dt} = i_{cell}(E_{rev} - E_{cell}) - h(T_{cool} - T_{cell}) \tag{4.32}$$

Where C_t is the thermal capacitance of the fuel cell and h is the heat transfer coefficient of convection in Watts per Kelvin.

The terminal voltage of a fuel cell stack using a lumped parameter approach can be calculated as follows:

$$V_T = N_{cell}E_{cell} \tag{4.33}$$

Where N_{cell} represents the series number of cells in the stack. To simulate the transient characteristics, the three dominant domains were incorporated into the model. These include the fluidic, electrical and thermal dynamics. During transient state, there are delays between the change in current and the flow rates of the fuel and the oxygen as supplied by the mass flow controllers. These dynamics are modelled by using mass balance as follows [10]:

$$\frac{M_{gas}V_{ch}}{RT}\left(\frac{d}{dt}P_{ch}\right) = \sum_{\overline{out}}^{Ch} \dot{q}_{fluid} \tag{4.34}$$

Where V_{ch} is the volume of the channels in m^3, P_{ch} is the pressure of the gas in the channel, M_{gas} is the molar mass and $\dot{q}_{fluid}$ is the fluid mass flow.

Equations (4.30) and (4.31) are modified to produce the following first order differential equations to calculate the flow rates in the anode and cathode gas channels [11], [12]:

$$\tau_a \frac{dM_{H_2net}}{dt} = \frac{i}{2F} - M_{H_2net} \tag{4.35}$$

$$\tau_c \frac{dM_{O_2net}}{dt} = \frac{i}{4F} - M_{O_2net} \tag{4.36}$$

The time constants τ_a and τ_c represent the mass transport delays of the anode and cathode respectively. M_{H_2net} and M_{O_2net} represent the net molar flow rates of the hydrogen and oxygen in the fuel cell.

4.2.5 Circuit Model Development

Most of the expressions presented can be related to both variable voltage sources and resistors. To get direct access to the parameters that effect the degradation and subsequent performance loss, the non-linear components can be represented by a diode using a simplified Shockley approximation as follows:

$$V_D = NV_T ln\frac{I_D}{I_S} \tag{4.37}$$

Where V_D is the voltage drop across the diode, N is the diode ideality factor, V_T the thermal voltage, I_D the diode current and I_S the saturation current. The thermal voltage of the diodes is related to the cell temperature as follows:

$$V_T = \frac{RT}{nF} \tag{4.38}$$

For a single cell, a series connection of resistors and diodes, each representing a voltage loss component of (4.1) is used, as shown in Fig. 4.1. The voltage source set-point is calculated by using (4.2). The anode and cathode activation voltages are separated to account for catalyst contamination or degradation. The charge double layer effect relating to the electrical dynamics is added as a capacitor across the activation loss components. The ohmic resistance of the cell as a function of acid content is represented by a variable resistor.

For the activation voltage loss, the diode ideality factor is set to the inverse of the respective charge transfer constant for the anode and cathode. The diode current is the fuel cell current per unit area and the saturation currents are set to the exchange current densities as calculated by (4.8) and (4.9). The loss in active surface area due to poisoning and catalyst degradation will reduce the effective surface area influencing the exchange current densities and, consequently, the saturation currents of the diodes according to the relationships presented in the previous section. The electrical charge double layer capacitance for the circuit is determined by using (4.29). The ohmic resistance of the cell is represented by the variable resistor of the model and is calculated as follows:

$$R_{ohmic} = R_{mem} + R_{contact} \tag{4.39}$$

where the membrane and contact resistances are calculated using (4.22) and (4.27). The model constants and the empirical coefficients used to model the individual degradation mechanisms are presented in table 4.1. The coefficients were determined using non-linear optimization of the least square error between the model and the experimental data using the MATLAB optimization toolbox.

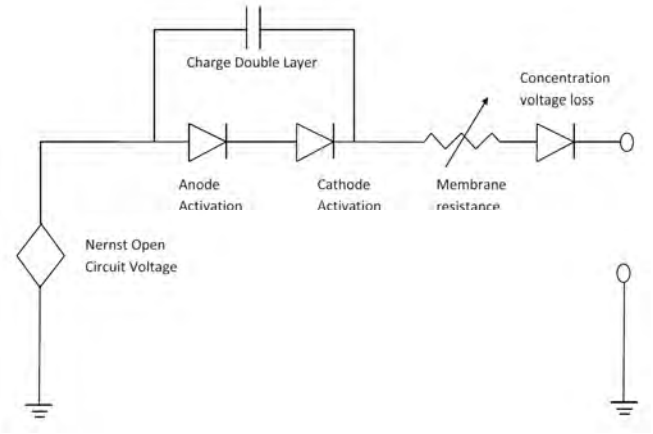

Figure 4.1. Equivalent circuit model.

TABLE 4.1
HT-PEM DEGRADATION MODEL CONSTANTS

Coefficient	*Symbol*	*Value*	*Unit*
Charge transfer coeff anode	α_a	0.48	-
Charge transfer coeff cathode	α_c	0.65	-
Reaction order cathode	γ	1	-
Reaction order anode	γ_1	0.5	-
Activation energy anode	Ea	72.4×10^{3}	$J.mol^{-1}$
Activation energy cathode	*Ec*	16.9×10^{3}	$J.mol^{-1}$
Ref. temperature	T_{ref}	433	K
Ref.pressure H2	P_{H2}^{0}	1.01325	bar
Ref. pressure O2	P_{O2}^{0}	1.01325	bar
Ref. exchange current density	$i_0^{a,ref}$	0.062	-
Ref. exchange current density	$i_0^{c,ref}$	1.13×10^{-8}	-
Porosity	*e*	0.3	-
Mean pore radius	r_p	0.04	μm
Catalyst degradation coefficient	β_1	0.5×10^{-9}	-
Catalyst degradation coefficient	β_2	0.01	-
Catalyst degradation coefficient	β_3	0.1×10^{-4}	-
Catalyst degradation coefficient	β_4	0.01	-
Catalyst degradation coefficient	β_5	0.02	-
CO poisoning coefficient	σ_1	20	-
CO poisoning coefficient	σ_2	1.2	-
CO poisoning coefficient	σ_3	0.67	-
CO poisoning coefficient	σ_4	0.4	-
Membrane thickness	δ_m	100×10^{-6}	m
Initial acid doping level	*DL*	28	-

4.3 Fuel Cell Emulator Platforms

In this work, two emulator systems were developed to verify performance of the models and the proposed hardware. The first is a single cell emulator that is able to output voltages below 1V at high currents and was used to emulate HT-PEM operation. A second emulator system, developed in [9], is capable of producing stack level voltages and was used to emulate LT-PEM flooding operation with the results presented in Appendix A.

In general, fuel cell emulators either make use of high precision controllable voltage sources and amplifiers or switch mode power electronic converters to reproduce the fuel cell electrical characteristics as determined by a model [7], [9]-[16]. While the high precision programmable power supplies are able to produce both single cell and stack level outputs they are in general expensive and bulky. To reduce cost, DC-DC or AC-DC switch mode power electronic topologies have been developed. Due to the losses, however, single cell voltages are difficult to control. To overcome this limitation, this thesis proposes the use of a single high performance power transistor that acts as a high precision dynamic resistor that in turn emulates the internal loss mechanisms of the fuel cell. This is connected to a standard low cost DC power supply as shown in Fig. 4.2. The transistor is controlled to operate in the active region with analogue gate drive circuitry.

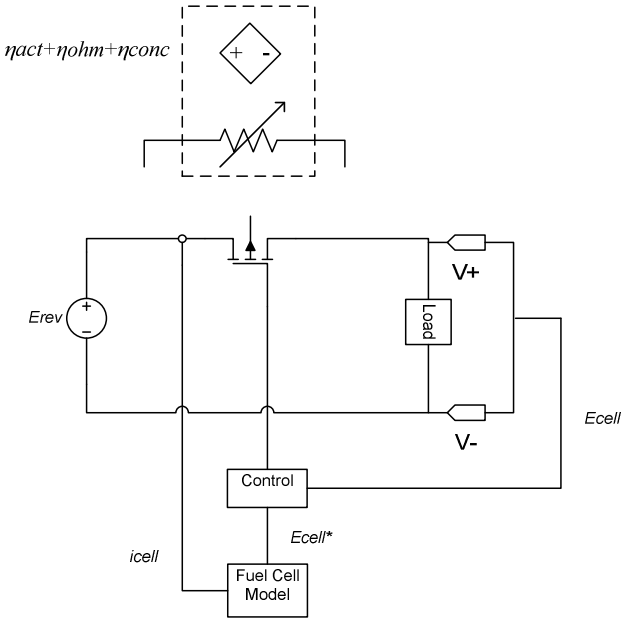

Figure 4.2. Schematic of the single cell emulator.

4.4 Emulator Experimental Setup

The experimental setup of the single cell emulator system is shown in Fig. 4.3. The control systems are implemented on a dSpace DS1104 prototyping system and allows for real time variation of the input parameters of the PEM FC model. The input and output currents and voltages are recorded using the real time workshop data acquisition tool. The output voltage of the emulators are monitored and recorded on a digital oscilloscope with a 1.2 giga sample per second bandwidth.

An electronic load is used to control the output current of the emulator systems. Pre-programmed current density set points that match those used during the testing of the fuel cells are used to test the output response of the emulators during steady state and transients.

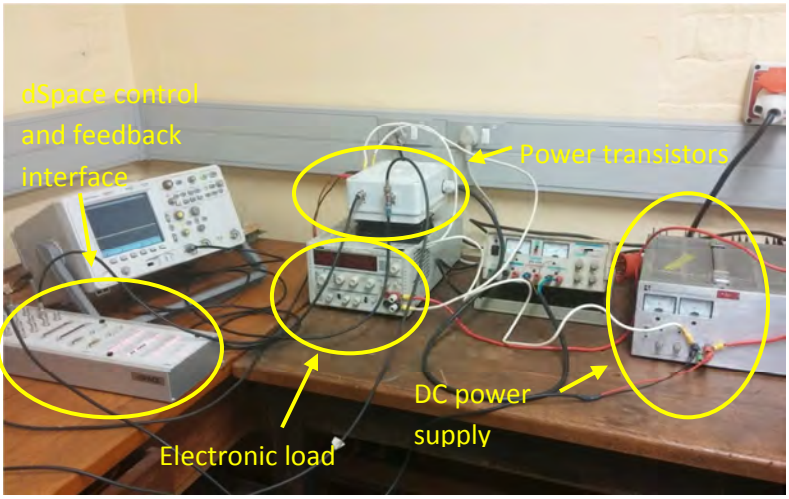

Figure 4.3. Experimental setup of the single cell emulator system.

4.5 Results and Discussion

The coefficients of the semi-empirical model were fitted to experimental data, where available, of the tested 45cm^2 HT-PEM fuel cell using a non-linear least squares approach. For mechanisms where limited experimental data were available, the model coefficients were approximated based on experimental data available in literature.

The effect of catalyst degradation on the fuel cell output is depicted by the polarization

curves of Fig. 4.4. As discussed in chapter 3, this mechanism will degrade the catalyst/carbon support required to facilitate the electrochemical reaction. To accelerate the effect, the cell was run at open circuit voltage (OCV) for a period of 24 hours after which results were captured. By running the cell at no load, the effect of acid leaching is kept to a minimum and the effect of catalyst degradation can be captured and modelled. The effect on performance is clearly visible in the figure and the performance loss follows an almost linear trend for increasing current. The simulated and experimental results of the proposed model and single cell emulator are plotted overlapping the experimental results from the fuel cell and demonstrate acceptable accuracy with minimal model complexity. It should be noted that the single cell emulator requires a finite amount of current to function properly, therefore the curves were recorded from 20mA/cm^2 upwards in this work.

The loss in performance due to the drop in MEA acid content is presented in Fig. 4.5. Acid loss occurs over time in an operational fuel cell due to evaporation mainly in the cathode. The water generated by the reaction acts as a carrier and can accelerate degradation for high current operation when more water is produced. It is clear that the performance loss is non-linear with respect to the leaching effect and the model is able to reproduce the effect accurately. The drop in acid content causes the effective membrane and contact resistances to increase and was modelled accordingly. Variation in acid content contributes mainly to the effective ohmic resistance of the cell as captured by the variable resistor in the model. A minimal effect on the activation loss is present. The proposed model and emulator delivered acceptable performance for this mechanism.

A combination of catalyst degradation and acid leaching is always present in an operational fuel cell and affects the life expectancy. Based on the experimental results and the developed model, the life expectancy can be estimated. The modelled results for different operating temperatures at a constant current density of 0.2A/cm^2 are presented in Fig. 4.6. It is clear that even though the cell produces greater output power at higher temperatures the failure time is greatly reduced. Based on such analyses, system optimization can be conducted to improve total energy output over the life time of the system.

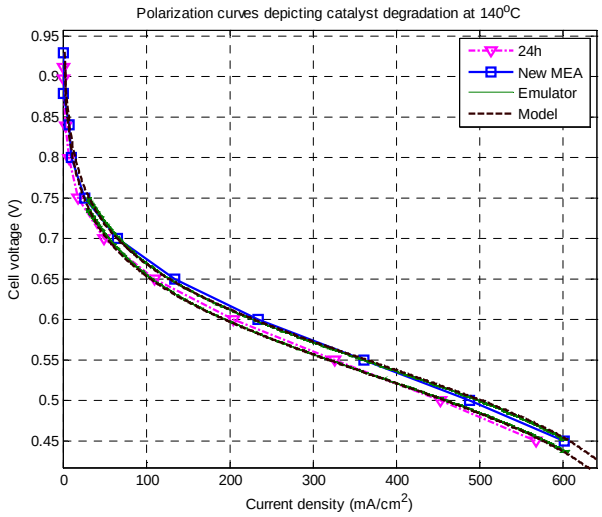

Figure 4.4. Experimental and model polarization curves for catalyst degradation.

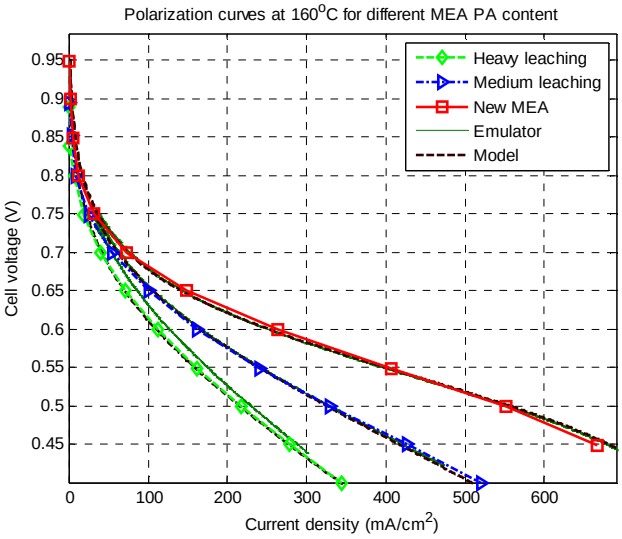

Figure 4.5. Experimental and model polarization curves for acid leaching.

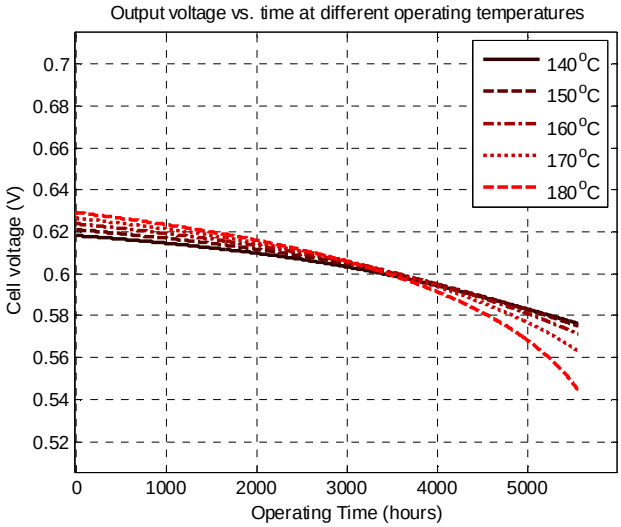

Figure 4.6. Lifetime prediction including catalyst degradation and acid leaching.

Current ripple is typically introduced by the DC-DC converter and/or inverter connected to the terminals of the fuel cell. Depending on the switching scheme, topology and control of the power electronics, a wide range of ripple current frequencies can be present. As discussed in the previous section, ripple current or continuous switching between two current set points for prolonged periods of time causes catalyst/carbon degradation similar to prolonged operation at OCV. For the evaluation of current ripple on performance, the percentage voltage loss with respect to frequency variation from [20] was used to fit the parameter coefficients for the relationship presented in (4.13). An estimate of the drop in performance at different current ripple frequencies was modelled and successfully emulated, as shown in the results presented in Fig. 4.7. Experimental data of this effect on HT-PEM fuel cells is still limited.

The CO poisoning effect on cell performance will be investigated further in chapter 5. To verify performance of the model and emulator, results for varying CO concentrations at 180°C and 160°C are presented in Fig. 4.8 and Fig. 4.9 respectively. The catalyst coverage as a function of temperature, current and CO concentration is effectively captured by the semi-empirical relations despite the complexity of the phenomenon. For a reduction in operating temperature, catalyst coverage can be severely increased causing increased losses in the anode activation component. During load transients, the increased activation losses become clearly visible, as shown in Fig. 4.10. During this test, a 10% load step was applied to the cell for different CO concentrations. The initial ohmic voltage loss and discharge due to the charge double layer is clearly visible. Minor discrepancies between the model and experimental results are present and can be attributed to diffusion dynamics and minor variations in CO catalyst coverage taking place during the transients that were omitted to reduce model complexity.

Based on the experimental results and the corresponding model fit, the lifetime performance of an HT-PEM fuel cell in the presence of CO can be estimated, as shown in Fig. 4.11.

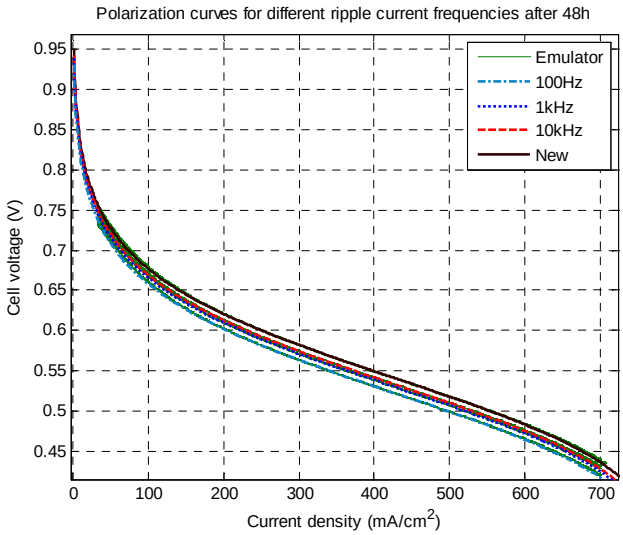

Figure 4.7. Model polarization curves depicting the effect of ripple frequency.

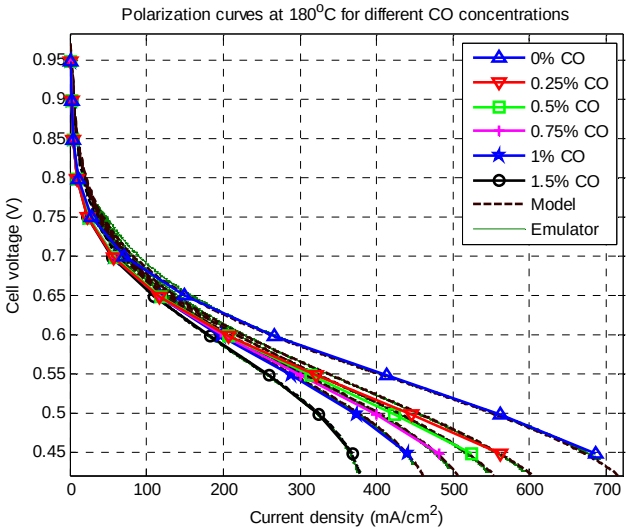

Figure 4.8. Experimental and model polarization curves for CO poisoning.

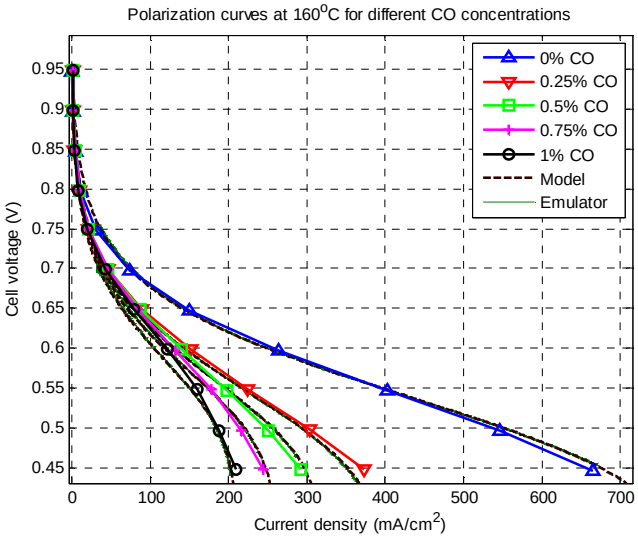

Figure 4.9. Experimental and model polarization curves for CO poisoning.

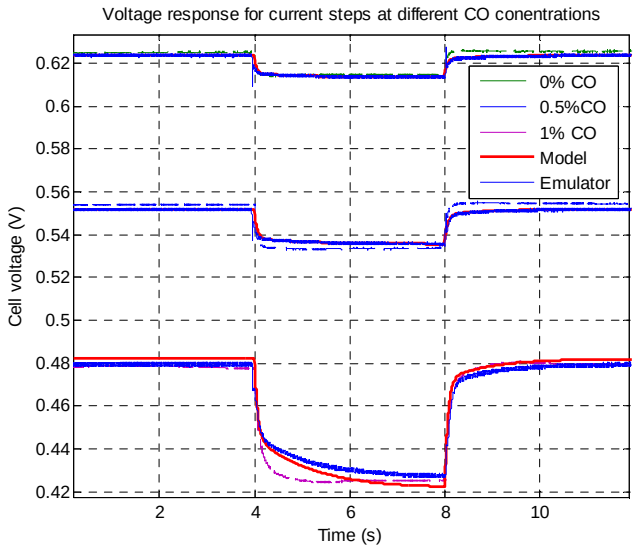

Figure 4.10. Voltage response for current step at different CO concentrations.

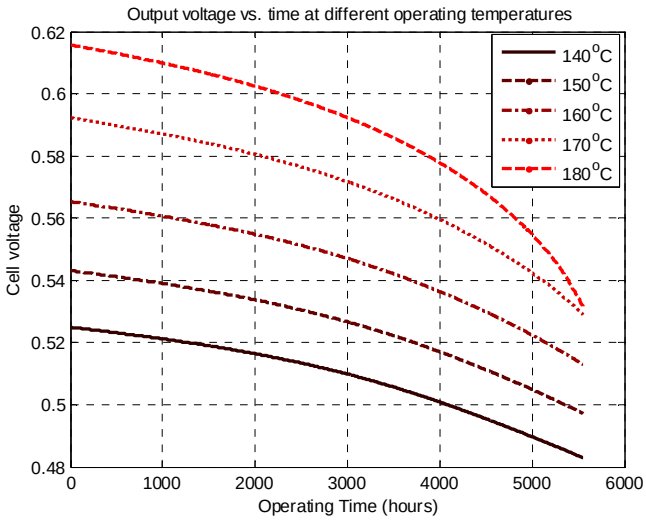

Figure 4.11. Lifetime prediction including catalyst degradation and acid leaching during CO poisoning.

The increased temperature demonstrates distinct improvements in CO tolerance and voltage levels for the constant loading of 200mA/cm^2. Operation at the higher temperature will, however, result in increased catalyst degradation over time. The system can be optimized to maximize performance with respect to the CO content while minimizing the effect caused by the other degradation mechanisms presented.

Conclusion

It is the objective of this chapter to present a system that can emulate HT-PEM fuel cell characteristics under both normal and fault conditions. The results from the simplified lumped parameter model that were applied on real time emulator system that requires the minimum amount of processing hardware is presented. The model takes into account the three dominant transient domains that effect output voltage and current characteristics for both steady state and transient behaviour. The model is derived from a detailed study on the electrochemical formulation of fuel cell behaviour and incorporates the main degradation mechanisms that cause system failure. This allows for the estimation of cell life expectancy based on operating conditions. The effect of ripple current on performance loss is investigated and the parameter variations based on loading time and frequency modelled accordingly. The model was validated against experimental data collected as well as that presented in other published works.

The developed circuit model can be used to estimate real time performance in simulators or incorporated into hardware in the loop emulators to facilitate and accelerate system development and optimization. Current emulator systems are designed to replicate fuel cell performance under normal operating conditions. A single cell and stack level emulator platform is developed that was able to emulate the behaviour of the fuel cell as predicted by the model. The experimental results obtained from the emulator during validation and testing for the fault mechanisms is presented and corresponds well to the results in literature and that presented in the previous chapters. This system will contribute to the development of control philosophies and power conditioning hardware, which will be able to mitigate the fuel cell fault conditions, without the use of the actual fuel cell systems.

References

[1] Amrit Chandan et al., " High temperature (HT) polymer electrolyte membrane fuel cells (PEMFC) - A review", *Journal of Power Sources*, Vol. 231, pp 264-278, 2013.

[2] Yuka Oono, Atsuo Sounai, Michio Horia," Influence of the phosphoric acid-doping level in a polybenzimidazole membrane on the cell performance of high-temperature proton exchange membrane fuel cells", *Journal of Power Sources*, Vol. 189, pp 943-949, 2009.

[3] Rodrigues, A. Amphlett, J.C.; Mann, R.F. Peppley, B.A. Roberge, P.R., "Carbon monoxide poisoning of proton-exchange membrane fuel cells," Energy Conversion Engineering Conference, 1997. IECEC-97., Proceedings of the 32nd Intersociety, vol.2, pp.768-773, 27 Jul-1 Aug 1997.

[4] Jung-Min Kwon; Kim Eung-Ho; Bong-Hwan Kwon; Kwang-Hee Nam, "High-Efficiency Fuel Cell Power Conditioning System With Input Current Ripple Reduction," *Industrial Electronics, IEEE Transactions on* , vol.56, no.3, pp.826,834, March 2009.

[5] Xiaohu Liu; Hui Li; Zhan Wang, "A Fuel Cell Power Conditioning System With Low-Frequency Ripple-Free Input Current Using a Control-Oriented Power Pulsation Decoupling Strategy," *Power Electronics, IEEE Transactions on* , vol.29, no.1, pp.159,169, Jan. 2014.

[6] Caisheng Wang; Nehrir, M.H.; Shaw, S.R., "Dynamic models and model validation for PEM fuel cells using electrical circuits," *Energy Conversion, IEEE Transactions on* , vol.20, no.2, pp.442,451, June 2005

[7] Restrepo, C.; Konjedic, T.; Garces, A.; Calvente, J.; Giral, R., "Identification of a Proton-Exchange Membrane Fuel Cell's Model Parameters by Means of an Evolution Strategy," *Industrial Informatics, IEEE Transactions on,* DOI 10.1109/TII.2014.2317982.

[8] Puranik, S.V.; Keyhani, A.; Khorrami, F., "State-Space Modeling of Proton Exchange Membrane Fuel Cell," *Energy Conversion, IEEE Transactions on* , vol.25, no.3, pp.804,813, Sept. 2010.

[9] C. de Beer, P.S. Barendse and M.A. Khan, "Development of an HT PEM Fuel Cell Emulator Using a Multiphase Interleaved DC–DC Converter Topology," *Power Electronics, IEEE Transactions on*, vol.28, no.3, pp.1120-1131, March 2013.

[10] F. Gao, , B. Blunier, M.G. Simoes, and A. Miraoui, "PEM Fuel Cell Stack Modeling for Real-Time Emulation in Hardware-in-the-Loop Applications", *IEEE Transactions On Energy Conversion*, Vol. 26, No. 1, March 2011.

[11] Zehra Ural and Muhsin Tunay Gencoglu, Mathematical Models of PEM Fuel Cells, *5th International Ege Energy Symposium and Exhibition (IEESE-5),* Pamukkale University, Denizli, Turkey, 27-30 June 2010.

[12] M Hashem Nehrir and Caisheng Wang, Modeling and Control of Fuel Cells, Wiley & Sons, 2009.

[13] S. C Choe et al., "Dynamic simulator for a PEM fuel cell system with a PWM DC/DC converter", *IEEE Transactions on energy conversion*, vol. 23, No. 2, pp 669-680, June 2008.

[14] G. Marsala, M. Pucci, G. Vitale, M. Cirrincione, and A. Miraoui, "Aprototype of a fuel cell PEM emulator based on a buck converter," *Appl. Energy*, vol. 86, pp. 2192–2203, Oct. 2009.

[15] F. Gao, B. Blunier, D. Bouquain, A.Miraoui, and A. E. moudni, "Polymer electrolyte fuel cell stack emulator for automotive hardware-in-the-loop applications," in *Proc. IEEE Veh. Power Propulsion Conf.*, pp. 998–1004, Sep. 7–11 2009.

[16] A. Gebregergis and P. Pillay, "The Development of solid oxide fuel cell (SOFC) emulator", in *Proc. IEEE Power Electronics Specialists Conference*, Orlando FL, pp. 1232 – 1238, 2007.

[17] K. Jiao and X. Li, "A Three-Dimensional Non-isothermal Model of High Temperature Proton Exchange Membrane Fuel Cells with Phosphoric Acid Doped Polybenzimidazole Membranes", *FUEL CELLS*, Vol. 10, No. 3, pp. 351-362, 2010.

[18] F. Barbir, PEM Fuel Cells – Theory and Practice, Elsevier Academic Press, 2004.

[19] P.O. Olapade, J.P. Meyers, R.L. Borup, R. Mukundan, "Parametric Study of the Morphological Properties of HT-PEMFC Components for Effective Membrane Hydration", *Journal of the Electrochemical Society*, vol. 156 no.6, pp. B639-B649, 2011.

[20] Jong-Hoon Kim et al., "An Experimental Analysis of the Ripple Current Applied Variable Frequency Characteristic in a Polymer Electrolyte Membrane Fuel Cell", *Journal of Power Electronics*, Vol. 11, No. 1, January 2011.

[21] Yunfeng Zhai, Huamin Zhang, Danmin Xing and Zhi-Gang Shao, "The stability of Pt/C catalyst in H3PO4/PBI PEMFC during high temperature life test", *Journal of Power Sources*, Vol. 164, pp. 126–133, 2007.

[22] Kim J, et al., "Degradation modeling and operational optimization for improving the lifetime of high temperature PEM (proton exchange membrane) fuel cells", *Energy*, 2013, http://dx.doi.org/10.1016/j.energy.2013.08.053.

[23] A. Bergmann, D.Gerteisen, T. Kurz, 'Modelling of CO Poisoning and its Dynamics in HTPEM Fuel Cells", *FUEL CELLS*, Vol. 10, No. 2, pp. 278-287, 2010.

[24] Kui Jiao, Ibrahim E. Alaefour, Xianguo Li, "Three-dimensional non-isothermal modeling of carbon monoxide poisoning in high temperature proton exchange membrane fuel cells with phosphoric acid doped polybenzimidazole membranes", *Fuel*, Vol. 90, Issue 2, pp. 568-582, February 2011.

[25] M. Boaventura, J.M. Sousa, A. Mendes, "A dynamic model for high temperature polymer electrolyte membrane fuel cells", *International Journal of Hydrogen Energy*, Vol. 36, Issue 16, pp. 9842-9854, August 2011.

Chapter 5

Diagnosis and Mitigation of CO Poisoning In HT-PEM Fuel Cells

5.1 Introduction

PEM fuel cells still suffer from a wide range of operational issues that can degrade performance, as discussed in the previous chapters. This can include complex water management systems and susceptibility to CO poisoning when utilizing hydrogen generated by a reformer. A general fuel cell power generator incorporating a reformer system is presented in Fig. 5.1. By operating at higher cell temperatures, the water management system can be simplified as water is assumed to be in vapour phase. HT-PEM fuel cells present other advantages including increased electrochemical kinetics, simplified cooling systems and the ability to recover the waste heat in combined heat and power (CHP) applications. The increased temperature also allows the cell to tolerate higher concentrations of impurities in the gas streams. CO in the anode is of particular interest as this gas is prominent in hydrogen generated by a reformer. The adsorption of CO onto the platinum catalyst reduces the effective surface area that can participate in the Hydrogen Oxidation Reaction (HOR). This results in a reduction in the output power that can be delivered by the system. In chapter 3 it was shown how CO poisoning can be differentiated from the other possible fault mechanisms. Due to the complexity of the phenomenon, further investigation across a wide range of operating conditions is required to properly

analyze the fault and is now further explored in this chapter.

Electrochemically, the adsorption of CO onto the platinum is related to high negative entropy and is thus greater at low temperatures [1]. The reaction in the anode for a pure H_2 gas stream can be represented by (5.1) and (5.2).

$$H_2 + 2(Pt) \leftrightarrow 2(Pt - H) \tag{5.1}$$
$$2(Pt - H) \leftrightarrow 2(Pt) + 2H^+ + 2e^- \tag{5.2}$$

The two reactions representing the adsorption of CO are presented by (5.3) and (5.4) [1].

$$CO + (Pt) \leftrightarrow (Pt = CO) \tag{5.3}$$
$$2CO + 2(Pt - H) \leftrightarrow 2(Pt = CO) + H_2 \tag{5.4}$$

The CO in the anode catalyst is removed by electro-oxidation due to the presence of water. This reaction is represented by (5.5) [2].

$$CO = Pt + H_2O \leftrightarrow CO_2 + 2H^+ + 2e^- \tag{5.5}$$

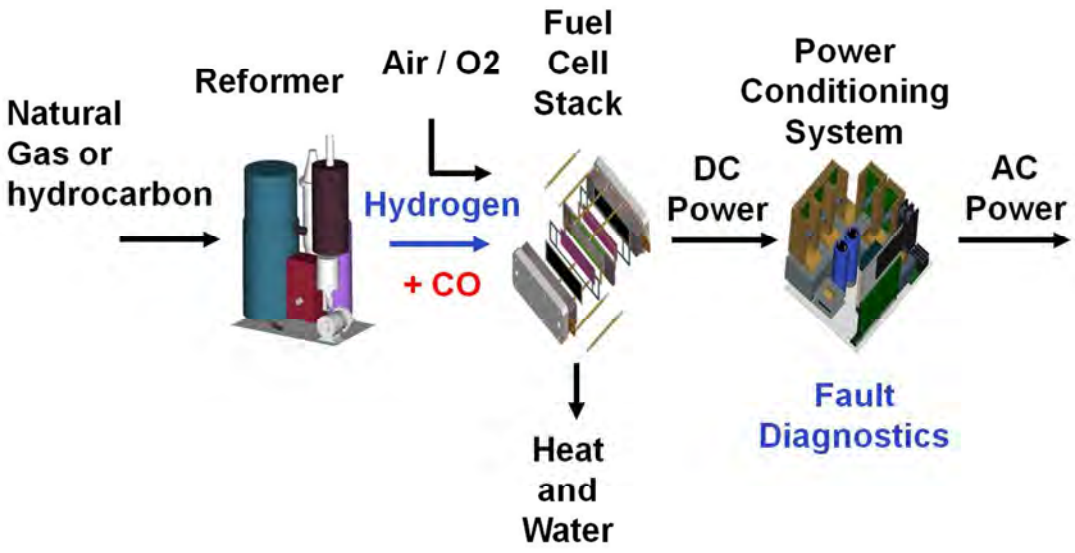

Figure 5.1. Reformer fed fuel cell system.

Other gasses generated by the reformer that can enter the gas stream such as N_2 and CO_2 are generally ignored in the analysis as these are almost electrochemically inert. The effect of CO in the anode can be investigated using electrochemical impedance spectroscopy (EIS) to determine the effect on the electrochemical circuit parameters [3]-[8]. Very little has been done to investigate the impact of CO on HT-PEM fuel cells under more extreme

operating conditions that may occur during transients, for example during system start-up. The low operating temperature and high CO concentrations can lead to a system fault and permanent degradation of the cell materials. This chapter presents results captured during a detailed study conducted on a HT-PEM fuel cell during CO poisoning in the anode gas stream. The steady state polarization curves at various operating conditions were captured and the drop in electrical performance for changes in CO content analyzed. From the experimental polarization curves, an electrical circuit model is developed to account for the impact of CO poisoning on the electrical performance of the fuel cell. The changes in electrochemical circuit parameters are tracked using the fitted equivalent electrochemical circuit (EEC) on the Nyquist plot generated from the EIS tests. In particular, CO concentrations above 1% were introduced into the anode gas stream to characterize the fuel cell under the more extreme operating conditions. The long term effects of CO poisoning on the HT-PEM fuel cell performance were investigated. The mitigation strategies used in LT-PEM were tested to reverse these effects and compared to the strategies proposed in this chapter that correspond to a more natural load profile.

The experimental setup that was constructed to conduct the CO analysis was presented in chapter 3, section 3.3.3. The EEC model and the steady state model used to fit the fuel cell experimental data is presented in section 5.3 and the mitigation in section 5.4. The experimental results from the EIS tests, polarization curves and transient tests are presented in section 5.5. The study on the long term effects and the proposed mitigation strategies are presented in section 5.6. Finally, conclusions are drawn and the results are discussed.

5.2 Diagnostics Using Equivalent Circuit Models

Circuit models for PEM fuel cells have been presented in literature [9]-[15], although very few exist for HT-PEM fuel cells. Analytical models have been developed [2], [4], [5] that accurately characterize the effects of CO poisoning on performance. However, these are complex and may not be suitable for implementation in online condition monitoring systems that require fast computational times [13], [16], [17]. Also, the experimental setup is complex and expensive to run and requires extensive periods of time to capture results. Therefore, to minimize the usage of the test setup and to ensure the computational

intensity of the models is reduced, circuit models are used to predict performance.

For a stationary power generator such as that presented in Fig. 5.1, a diagnostic system that can be integrated with the power conditioning subsystem can increase performance and life expectancy. Such a system might make use of small load perturbations to generate a Nyquist plot of the impedance for a certain bandwidth [18]. To reduce complexity and cost, a simple circuit model based observer diagnostic system may be employed to facilitate system optimization. Other model based diagnostic systems were presented in chapter 2 and reviewed in literature [19]. The more advanced and computationally intensive Neural Network and black box models provide better accuracy but require greater processing power from the hardware employed.

Monitoring a single circuit parameter may not be sufficient to diagnose a faulted condition. Therefore, two equivalent circuits were used to separately model the fuel cell parameter changes for polarization curve analysis and EIS analysis. Each model captures the changes in circuit parameters for the individual tests performed. During diagnostics it is required that multiple parameters be compared in order to accurately diagnose the fault condition. In the event that detailed EIS data is not available, the variation in the fault element component values of the polarization curve model can be used in conjunction with the variation of a single EIS EEC model parameter to deliver better accuracy during diagnostics.

5.2.1 Polarization Curve Equivalent Circuit

In chapter 4 it was shown that the steady state behaviour of an HT- PEM fuel cell can be represented by diodes and resistors that represent the respective loss components including the activation loss and ohmic voltage loss.

Concentration voltage losses occur when the reactant concentration at the catalyst sites start to drop due to diffusion limitations. The reaction thus consumes fuel at a faster rate than it can be supplied and is dependent on the amount of current produced. Therefore, the concentration losses only become substantial at high current densities beyond the maximum power point of HT-PEM fuel cells. Even with CO in the gas stream, the concentration of hydrogen is sufficient to sustain the reaction without the concentration losses becoming apparent due to the higher reaction kinetics in this temperature range. In this work the cell was not tested for high currents where cell voltages drop below 0.4V as

this enforces other degradation mechanisms, such as catalyst degradation. The circuit is simplified when the concentration loss component is ignored, allowing for easier implementation.

If the equivalent circuit in chapter 4 is used for steady state analysis only in order to capture polarization curve characteristics, the circuit can be simplified to a single diode and resistor, as shown in Fig. 5.2. For a specific operating condition, the component values will stay constant until CO is introduced. The fault mechanism in the steady state equivalent circuit can be represented by a second diode resistor pair, as shown in the figure. The component values for normal operation and during CO poisoning were calculated to fit the experimental polarization curves. The fault element in the circuit is only introduced once CO poisoning takes place and the resulting fit between the experimental data and the simulated circuit produced acceptable errors. By simplifying the model and monitoring only a single parameter for the diode and resistor, the variations can easily be tracked in an online condition monitoring system.

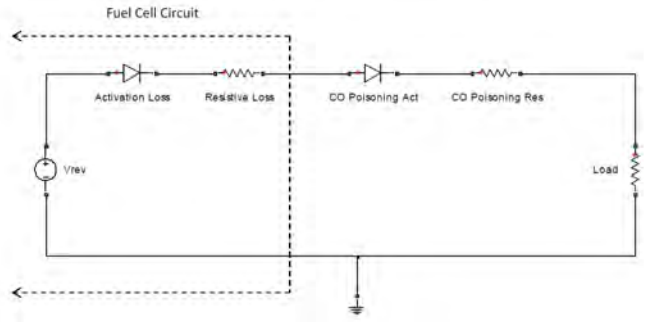

Figure 5.2. Equivalent circuit used to model polarization curves.

5.2.2 EIS Equivalent Circuit

The EEC model used to fit HT-PEM fuel cell EIS data was presented in chapter 3. However, in order to better quantify the effect of CO variation on the parameters, all three resistor capacitor pairs are used to model the three arcs observed in the experimental data with the high frequency sub-circuit no longer being ignored. The model parameters were optimised in MATLAB by using a minimization function and a bounded minimum search algorithm. The minimization function used to optimize the circuit parameters in order to

generate acceptable fits to the experimental plots is presented in (5.6).

$$\varepsilon = \sum_{n=1}^{N} \left(W_n \times \left[\left(real(Z_{mod})_n - real(Z_{exp})_n \right) + \left(im(Z_{mod})_n - im(Z_{exp})_n \right) \right] \right)^2 \quad (5.6)$$

Where N represents the number of frequency set points used in the EIS tests, W_n the weight matrix, Z_{mod} and Z_{exp} the impedance of the model and experimental data at a specific frequency.

In order to generate a better fit, the capacitive elements in the model were replaced by constant phase elements (CPE), as shown in Fig. 5.3. The general equation of the admittance for the CPE is presented in (5.7).

$$\frac{1}{Z} = Y = Q \times (j\omega)^A \quad (5.7)$$

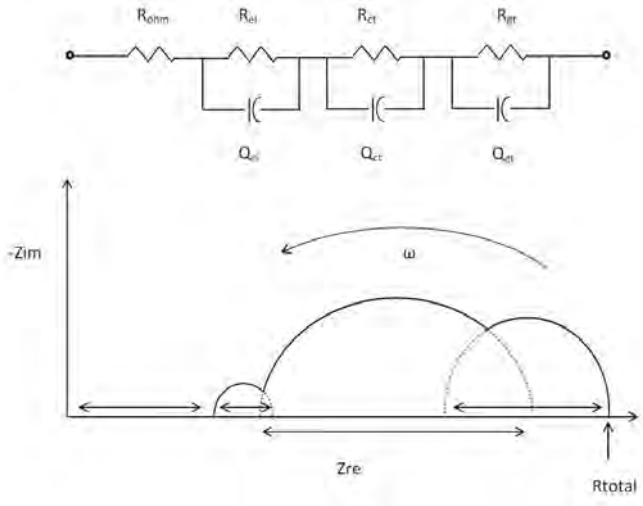

Figure 5.3. EEC used to model EIS data.

where A represents the angle of the element. The true capacitance can be calculated from (5.8); where ω_{max} is the angular frequency where the complex part of the impedance reaches a maximum.

$$C = Q \times (\omega_{max})^{A-1} \quad (5.8)$$

The inductive element observed in the high frequency range was ignored to reduce model complexity as it does not give significant information regarding cell performance.

The first arc in the Nyquist plot represents the electrode impedance of the fuel cell and is

represented by the first parallel resistor/CPE pair, R_{el} and Q_{el}. As the physical structure of the electrodes is minimally affected by the gas composition, little variation in these parameters is expected for CO poisoning. The second arc can be related to the reaction kinetics of the fuel cell and is influenced by a number of parameters including the CO concentration. The diameter of the arc represents the charge transfer resistance, R_{ct}, and is directly proportional to the derivative of the activation voltage loss component ($d\eta_{act}/di$) [21]. To relate the effect of CO on the charge transfer resistance and estimate surface coverage, the activation loss in the anode was calculated using the Bulter-Volmer relationship in (4.7).

The exchange current density, i_0, is the parameter that undergoes the greatest variation during CO coverage of the catalyst and can be related to the coverage as follows from (4.9) and (4.14):

$$i_0^a = i_o^{a,ref} S_{eff,a} \left(\frac{p_{H_2}}{P_{H_2}^0}\right)^{\gamma 1} \left(\frac{p_{H_2O}}{P_{H_2O}^0}\right)^{\gamma 2} exp\left[\frac{-E_a}{RT}\left(1 - \frac{T_{cell}}{T_{ref}}\right)\right](1 - \theta_{CO}) \qquad (5.9)$$

where i_o^{ref} is the reference exchange current density and θ_{co} the effective catalyst coverage of the CO in the anode. From the above relationships it is clear that the CO concentration will have a direct effect on the charge transfer resistance; it is therefore this parameter that will be mostly influenced in the Nyquist diagrams. The third arc in Fig. 5.5 represents the gas transport impedance and is modelled by the resistor/CPE pair, R_{gt} and Q_{gt}. The diameter of this arc gives information on the gas transport kinetics that can be related to the mass transport losses in the cell.

5.3 Mitigation of CO Poisoning Using Active Current Control

The power conditioning device or a separate active converter [22] can be used to control the output current profile of the fuel cell for a short period in order to mitigate the effects of the CO in the anode during a fault or system start-up. Available strategies make use of hard current pulsing between two set points to enforce electrode overvoltage that will effectively oxidize the CO that has bonded to the platinum catalyst reducing effective surface area and decreasing performance. This pulsing scheme has other negative effects, such as enhancing catalyst degradation that causes a permanent drop in performance and

cannot be mitigated. These techniques have been applied on LT-PEM systems but have not been tested on HT-PEM fuel cells. It is the purpose of this work to investigate these strategies and determine if other types of load control can provide better results. For the HT-PEM fuel cells, the higher rate of kinetics at the operating temperature reduces the effect of CO poisoning. However, at high concentrations there can still be a permanent bonding to the catalyst that must be mitigated. The high operating temperature allows for more flexibility in the current profile as it is easier to enforce CO oxidation. This work determined the most effective load profile to enforce the oxidation of CO and remove it from the catalyst sites and can be implemented on the power conditioning hardware in commercial systems and will be discussed in the following sections.

5.4 Experimental Setup

The experimental setup used for this chapter was presented in chapter 3 and the CO poisoning procedure detailed in section 3.4.5. The fuel cell was tested for a temperature range of 140°C to 180°C in 10°C increments. According to the manufacturer, the MEA was designed to work optimally between temperatures of 160°C and 180°C, and the results presented will be focused on this temperature region. The external temperature controller connected to the cartridge heaters was used for precise set point control. The test bench was used to perform all diagnostic tests including polarization curves, EIS and small current step responses. The analysis of the transient voltage characteristics will be presented in the following chapter.

5.5 Experimental Results and Discussion

5.5.1 Steady State Results

The polarization curves at constant stoichiometry for different CO concentrations at 160°C and 180°C are presented in Fig. 5.4 and Fig. 5.5 respectively. The increase in temperature results in a decrease in ohmic losses for the base curves recorded at 0% CO as expected. This is mainly due to the inherent characteristics of the acid doped polybenzimidazole (PBI) membrane. At higher temperatures, the proton conductivity of PBI increases, resulting in a reduction in losses in the linear ohmic region of the polarization curve. Once the CO is introduced into the gas stream, the drop in performance

is evident. The voltage loss at higher current densities for 0.25% CO is more prominent at 160°C when compared to the curve recorded at 180°C. The increased operating temperature and resulting increase in electrochemical kinetics restrict the adsorption of CO onto the catalyst. The curves generated at 160°C show that the cell voltage decays at a faster rate at a much lower current density and CO concentration than those generated at higher operating temperatures. This is mainly due to the increased restriction of the platinum sites due to the adsorption of CO and increased activation losses. Increasing the CO content in the anode gas stream beyond 1% at low temperatures becomes detrimental to the cell stability and was avoided in order to limit possible damage to the cell. At the higher temperatures, the cell demonstrated the ability to maintain stability despite the extreme CO content.

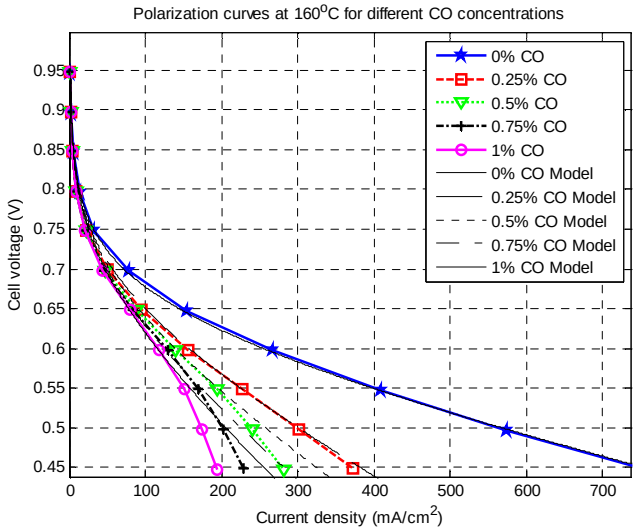

Figure 5.4. Experimental and simulated polarization curves generated at 160°C.

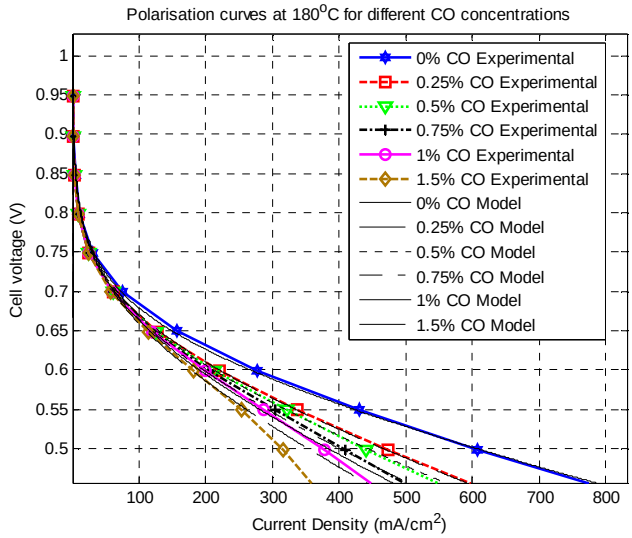

Figure 5.5. Experimental and simulated polarization curves generated at 180°C.

The Nyquist plots of the impedance for cell temperatures of 160°C and 180°C are shown in Fig. 5.6 and Fig. 5.7 respectively for a current density of 100mA/cm^2. The Nyquist plot for a current density of 200mA/cm^2 is presented in Fig. 5.8 and demonstrates the effect increased load has on the cell characteristics. The fitted Nyquist plots from the optimized EECs are presented as dashed lines overlapping with the experimental plots in the figures. From the results it is clear that there are three distinguishable arcs at the high, medium and low frequency ranges, with the medium frequency arcs being the most prominent. Very little change in the high frequency real axis intercept occurs for changes in CO concentration, which can be related to the ohmic resistance of the cell. This is to be expected, as the reduction of active catalyst sites should have very little impact on the physical properties that contribute the electrical ohmic resistance.

The diameter of the mid frequency arc of the Nyquist plots increases with the increase in CO concentration for the lower cell temperatures, as shown in Fig. 5.6 for 160°C. For the higher temperatures the increase in diameter is less prominent and only becomes more apparent at very high CO concentrations (above 1%) or at the higher current densities. The diameter of the mid frequency arc typically represents the charge transfer resistance of the cathode catalyst layer [7]. The anode impedance is usually ignored due to the fast rate of the HOR [21]. The more profound increase in the mid frequency arc diameter or charge transfer resistance at high CO concentrations indicate that the reaction in the anode contributes to the measurements. The active catalyst surface area decreases as the cell temperature is reduced due to the thermodynamic nature of the adsorption of CO onto the platinum. By operating the cell at higher temperatures, the adsorption rate is reduced and therefore will have a smaller effect on the EIS spectra. By increasing the current density and thus the gas flow rate, more CO is introduced into the gas stream thereby increasing the adsorption rate of the CO. This is demonstrated when comparing the 1% and 1.5% CO Nyquist plots in Fig. 5.7 and Fig. 5.8 as a significant increase in diameter between the two curves is evident. The low frequency arc becomes more visible once CO is introduced. Increasing the current density and CO concentration leads to an increase in the diameter of the arc. For healthy operation it is difficult to visually distinguish the low and mid frequency arcs. The low frequency arc may represent the mass transport limitations or the gas-phase diffusion resistance of the cell as stated in [7], [8] and [21]. The interpretation of the high frequency arc is still a debated issue in literature [7], [8], and it is generally

assumed that this element in the EEC can be associated with the electrode properties of the cell [21]. In the experimental analysis, the impedance of the anode electrode becomes visible in the high frequency arcs as the CO is introduced. It was found that the change in the equivalent circuit parameters for the high frequency arc were inconsistent due to interference in the measured signal and vary little when compared to the other components of the EEC.

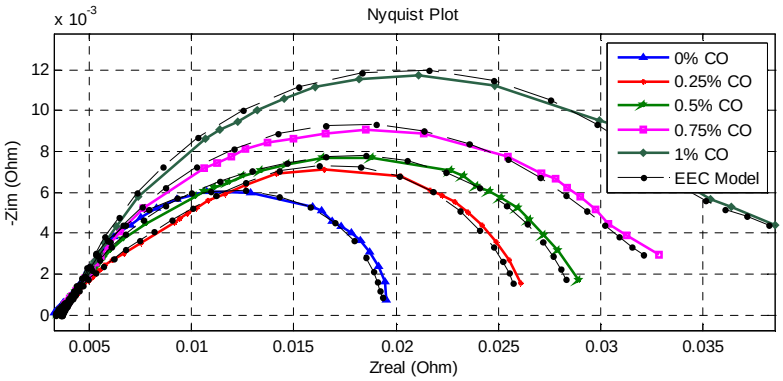

Figure 5.6. Nyquist plots generated at 160°C, 100mA/cm².

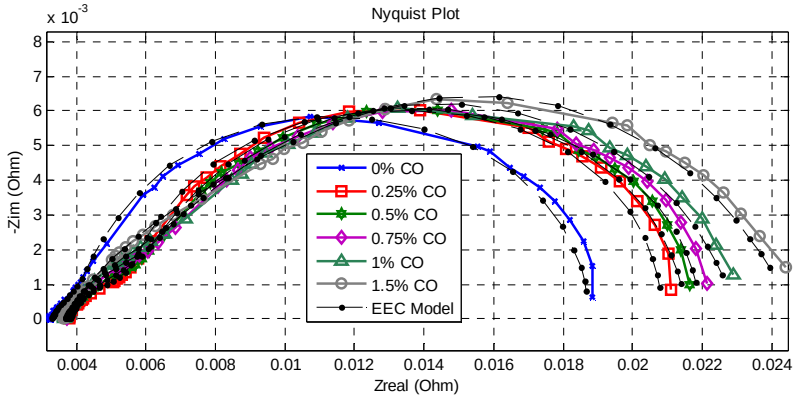

Figure 5.7. Nyquist plots generated at 180°C, 100mA/cm².

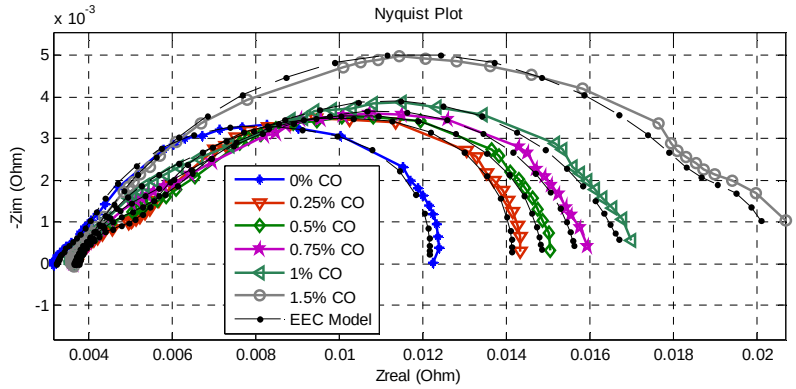

Figure 5.8. Nyquist plots generated at 180°C, 200mA/cm².

The phase and magnitude response at 160°C and 180°C are presented in Fig. 5.9 and 5.10 respectively. In the high frequency region, there is very little variation in the cell impedance for changes in CO concentration. There is, however, a small increase in impedance between the healthy and poisoned response. The cell impedance becomes more distributed in the medium and low frequency regions with greater variation under low temperature and high current densities. The slope in the response ($d|Z|/df$) increases as the CO concentration in the cell is increased. The same can be observed for a decrease in cell temperature and cell current density. Upon the introduction of CO in the gas stream, there is a drop in the peak of the phase response of the circuit. As the CO concentration is increased, the peak shifts towards a higher frequency region and starts to increase in magnitude. The same can be observed at higher temperatures.

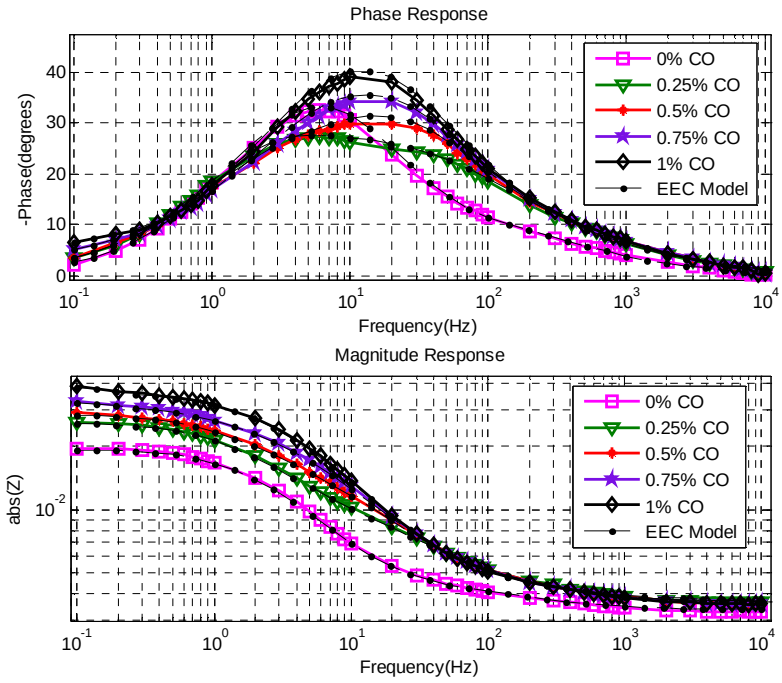

Figure 5.9. Bode plots generated at 160°C, 100mA/cm².

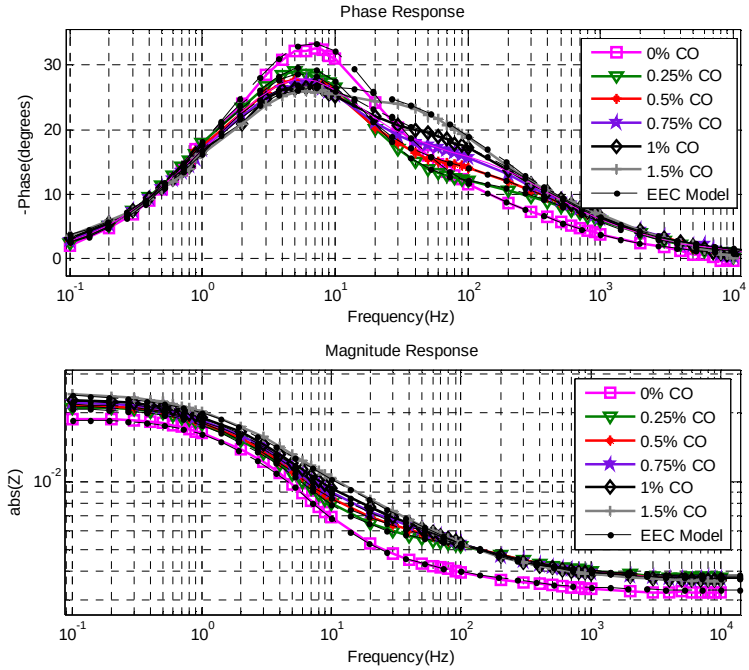

Figure 5.10. Bode plots generated at 180°C, 100mA/cm^2.

The variation of the imaginary parts on the impedance with frequency is presented in Fig. 5.11. For a specific temperature and current density, the curves peak at roughly the same frequency. Using this information, the peak capacitance of the system can be tracked by monitoring a single frequency in the fault detection system.

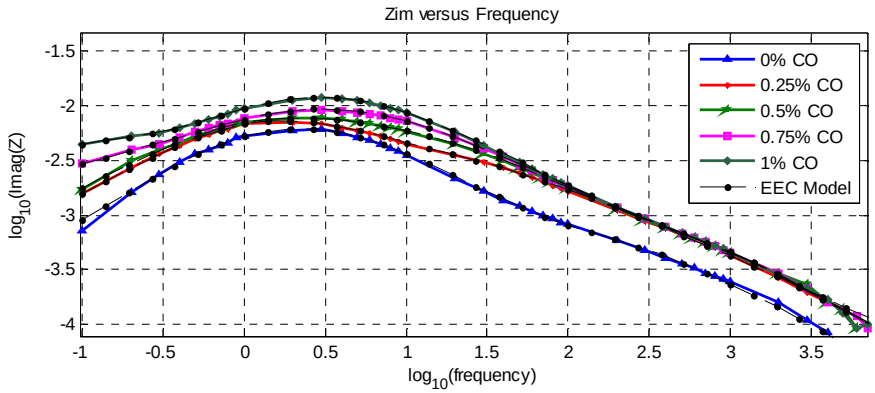

Figure 5.11. Variation of Zimag with frequency at 160°C, 100mA/cm^2.

5.5.2 Variation of Circuit Parameters

The equivalent electrochemical circuit (EEC) and the resulting fit to the Nyquist plots was presented in section 5.2.2 and 5.4.1 above. The corresponding values for the

parameters used in the model to fit the experimental data are presented in table 5.1. In order to obtain trends that can be tracked using an online condition monitoring system, the variation of the circuit parameters with changes in operating conditions was determined. The three main cell parameters that change during operation are the temperature, current density and the CO concentration. Changes in the flow control can also play an important part and were investigated. As observed from the Nyquist plots and the parameter values in table 5.1, the easiest parameter to track is the total resistance. This parameter can be determined from the low frequency real axis intercept on the Nyquist plots. For increased CO concentrations, this value could not be measured due to the low frequency measurement limit of 0.1Hz. The EEC and the fitting algorithm provide a way to extrapolate to this value from the experimental data. The value of the total resistance is directly proportional to the slope (*-dV/dI*) of the polarization curves [6]. The variation of the total resistance with current density for different CO content at a constant stoichiometry and temperature is presented in Fig. 5.12. As expected, the resistance decreases with current density for pure Hydrogen in the anode gas stream. As the CO concentration is increased, the slope of the curves starts to change from that of a healthy cell. At higher concentrations and current densities, the change becomes more profound. It is thus possible to determine the amount of CO poisoning at a certain temperature and load by tracking this value. The minima of these curves are directly proportional to the maximum power point of the fuel cell.

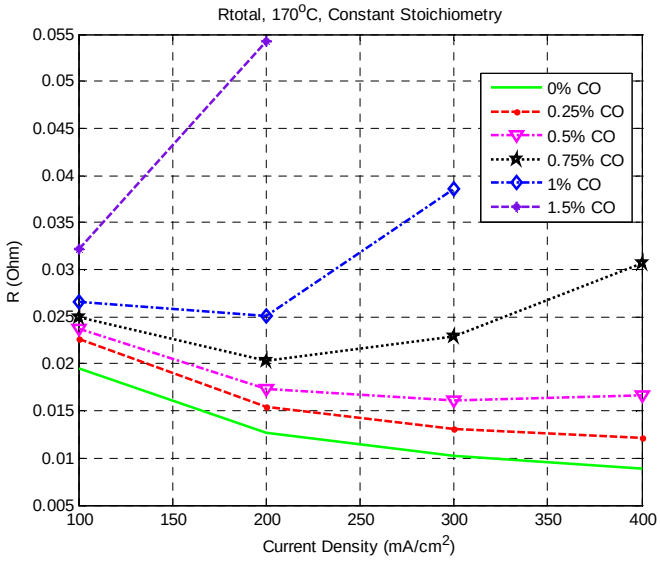

Figure 5.12. Total EEC resistance vs. current density at 170°C for constant stoichiometry.

TABLE 5.1
PARAMETERS FOR EEC MODEL

CO	*Rohm (Ω)*	*Rel (Ω)*	*Qel*	*Ael*	*Rct (Ω)*	*Qct*	*Act*	*Rgt (Ω)*	*Qgt*	*Agt*	*Rtot (Ω)*
					160°C 100mA/cm^2						
0	0.003358	0.000723	3.622369	0.826108	0.012698	6.357734	0.870299	0.002698	53.24084	1.000000	0.019477
0.25	0.003659	0.006834	6.570968	0.665274	0.011963	11.10966	0.85135	0.003815	42.3054	0.912549	0.026271
0.5	0.00365	0.000394	1.409801	0.909175	0.008739	4.276103	0.784477	0.016242	9.658566	0.822138	0.029024
0.75	0.003642	0.000196	0.565075	1.000000	0.027692	3.944404	0.742089	0.004009	507.5812	0.676595	0.035538
1	0.003648	0.000427	1.397141	0.910926	0.032297	2.85337	0.804731	0.004777	318.3242	1.000000	0.041149
					160°C 200mA/cm^2						
0	0.003273	0.000858	5.642451	0.782465	0.006569	5.849723	0.927193	0.001942	35.83889	1.000000	0.012642
0.25	0.00356	0.002439	7.353604	0.946575	0.011875	9.540984	0.613397	0.002118	25.92836	1.000000	0.019992
0.5	0.003626	0.000478	1.558952	0.902048	0.023275	2.82925	0.818452	0.002206	364.4863	1.000000	0.029585
0.75	0.003634	0.000542	0.99584	0.949805	0.041862	2.508464	0.847585	0.008924	116.6834	1.000000	0.054962
1	0.003602	0.000468	0.874954	0.980849	0.067143	2.863002	0.831459	0.010837	98.38071	1.000000	0.08205
					180°C 100mA/cm^2						
0	0.003288	0.000892	6.598668	0.755096	0.010632	5.667436	0.913321	0.003951	39.13417	1.000000	0.018763
0.25	0.003815	0.001845	2.274542	0.789086	0.008658	5.460542	0.951727	0.006547	24.35564	1.000000	0.020865
0.5	0.003753	0.002729	4.013886	0.710006	0.008821	5.971042	0.949729	0.006217	28.83158	0.983061	0.021521
0.75	0.00375	0.002545	2.766033	0.775067	0.013546	6.327031	0.869035	0.00218	102.3982	1.000000	0.022022
1	0.003691	0.003127	4.338509	0.719275	0.011446	7.982536	0.836636	0.004722	41.53664	0.885091	0.022986
1.5	0.003666	0.00286	9.092817	0.687959	0.012926	11.35886	0.673697	0.005321	20.75314	0.934973	0.024773
					180°C 200mA/cm^2						
0	0.003228	0.000812	6.000855	0.780189	0.006258	5.727367	0.928347	0.00186	37.25746	1.000000	0.012157
0.25	0.003754	0.001708	2.077914	0.804896	0.005284	5.932661	0.949682	0.003377	26.2102	1.000000	0.014124
0.5	0.003708	0.002685	2.879556	0.760369	0.003748	6.253552	0.994818	0.004706	19.92056	0.996364	0.014847
0.75	0.003683	0.002407	3.388018	0.761773	0.005929	8.285955	0.819585	0.003682	26.66327	0.965378	0.015702
1	0.003662	0.000135	0.500819	1.000000	0.003577	4.253577	0.766553	0.009535	9.638795	0.792177	0.016908
1.5	0.003647	8.87E-05	0.605249	1.000000	0.016028	4.627707	0.711631	0.000685	1076.992	1.000000	0.020449

The variation of the total resistance with cell temperature is presented in Fig. 5.13. The reduction in resistance with increased cell temperature is evident. From the curves it is also evident how great an influence temperature has on the adsorption of CO onto the platinum catalyst and the resulting drop in performance. Very high temperatures result in the smallest change to resistance and subsequently the corresponding polarization and power curves. If the fuel cell power system is fed from a reformer and the scrubbing phase is removed, the fuel cell should be started up at higher temperatures to avoid the initial poisoning that can occur as the reformer starts up and the CO concentration is high. Cell temperature can then gradually be lowered to optimal levels as soon as the Hydrogen and CO concentrations in the gas stream have stabilized.

The variation of charge transfer resistance with cell temperature is presented in Fig.

5.14. As can be seen it behaves in a similar manner as the total resistance. It was also found that the greatest change occurs in this element when tracking the four resistive elements in the EEC. To reduce computational effort when implementing in a real time diagnostic tool, the charge transfer resistance can be tracked by focusing on the mid frequency range (1Hz to 100Hz). This not only reduces measurement time but also reduces the load on the embedded processor in the diagnostics system.

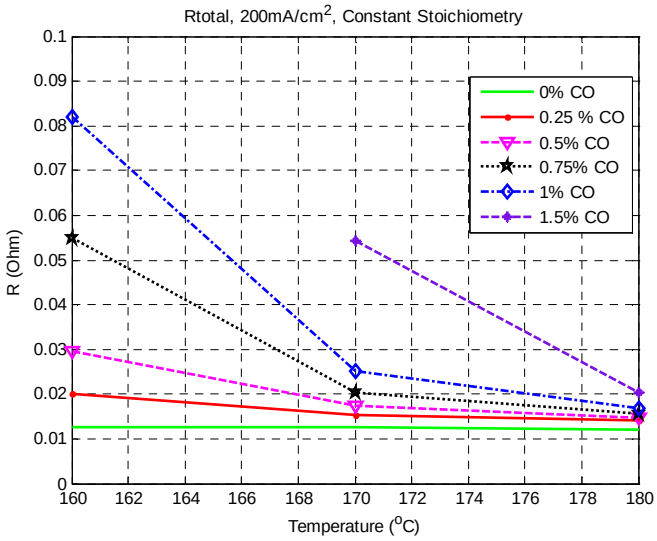

Figure 5.13. Total EEC resistance vs. temperature at 200mA/cm2 for constant stoichiometry.

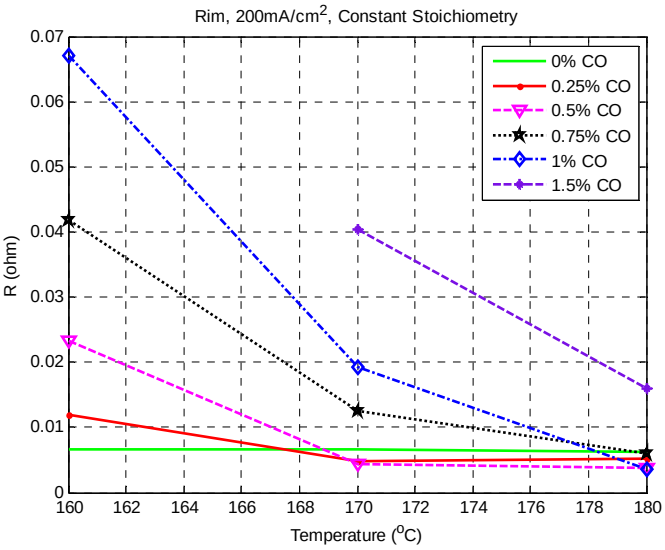

Figure 5.14. Charge transfer resistance (Rct) vs. temperature at 200mA/cm2 for constant stoichiometry.

The experimental polarization curves and the results from the circuit model of Fig. 5.2 at 160°C and 180°C are presented in Fig. 5.4 and Fig. 5.5. The parameters used in the model to simulate these curves are presented in table 5.2 where I_s represents the saturation current of the diodes and can be related to the exchange current density in (5.9). The additional activation loss and linear ohmic loss is simulated with the additional diode resistor pair with acceptable error. As the saturation current for the diodes is kept constant for each CO concentration in the polarization curve model, the difference between the curves will increase at low temperatures and high CO concentrations for high current densities. The error is acceptable considering the complex nature of CO poisoning and the simplicity of the circuit used to model the phenomenon. The model is thus well suited for condition monitoring in online systems and will perform effectively when combined with the Nyquist EEC trends.

The derivative of the experimental polarization curve, the simulated curve as well as the EIS data that corresponds to the 0.75% CO plot at 180°C is presented in Fig. 5.15. The total resistance from the EIS EEC model is directly proportional to the derivatives of both the experimental and simulated polarization curves as shown in the figure.

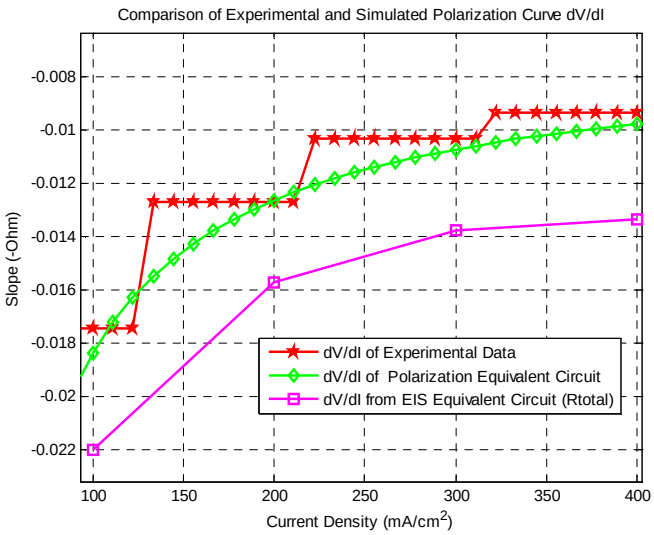

Figure 5.15. Comparison of the simulated and experimental slopes and EEC resistance.

TABLE 5.2
PARAMETERS FOR POLARIZATION CIRCUIT MODEL

CO	Is (A/m^2)	Rohm (Ω)	Isco (A/m^2)	Rco(Ω)
		160°C		
0	4.50E-13	0.00415	4.500E-11	0
0.25	4.50E-13	0.00415	4.473E-11	0.0061
0.5	4.50E-13	0.00415	4.462E-11	0.0085
0.75	4.50E-13	0.00415	4.451E-11	0.011
1	4.50E-13	0.00415	4.442E-11	0.013
		180°C		
0	4.50E-13	0.003778	4.500E-11	0
0.25	4.50E-13	0.003778	4.492E-11	0.001778
0.5	4.50E-13	0.003778	4.490E-11	0.002222
0.75	4.50E-13	0.003778	4.486E-11	0.003111
1	4.50E-13	0.003778	4.484E-11	0.003556
1.5	4.50E-13	0.003778	4.480E-11	0.004444

5.5.3 Dynamic Results

In order to gain a better understanding of CO poisoning and the effects it has on the fuel cell performance, dynamic tests were conducted by pulsing the fuel cell between two CO concentration set points. The tests were performed for both increasing and decreasing CO concentrations to determine the rates at which the CO adsorbs and desorbs onto and from the catalyst sites. The tests were conducted for cell temperatures of 140°C to 180°C to quantify the CO response to temperature. The tests were repeated at different flow rates and current densities to gain a better understanding of the phenomena and the impact on the deliverable output power under varying conditions.

The voltage response of the cell for a CO step of 0% to 0.5% at different cell temperatures is presented in Fig. 5.16. The set point change was sent to the mass flow controllers at the 5s mark. As can be seen, the CO rich gas takes a finite amount of time to enter the mixture in the gas stream. At a time of 18s the voltage starts to drop for all three the temperature set points. The introduction of CO has a smaller effect on the output voltage at the higher operating temperatures as expected. The lowest set point of 140°C resulted in a significant drop in voltage. It can also be concluded that the voltage loss follows a non-linear trend with respect to the cell temperature and corresponds to the results presented in the previous section.

To evaluate the effect of the CO concentration on the rate of platinum coverage, the anode was subjected to step changes from 0% to 0.5%, 1% and 1.5%, as shown in Fig. 5.17. There is a small difference between the initial voltages at the start of the test. This may be as a result of the system not reaching steady state conditions despite giving the system

ample time to recover between the individual tests. It can also indicate that there is a permanent degradation in performance and that the platinum surface area is not completely recovered after the CO is removed from the gas stream. The resulting drop in voltage for the step changes in CO concentration increases in magnitude as the CO concentration is increased. The settling time required to reach steady state remains fairly constant and indicates that it is not a function of temperature or current density but rather the gas flow rate.

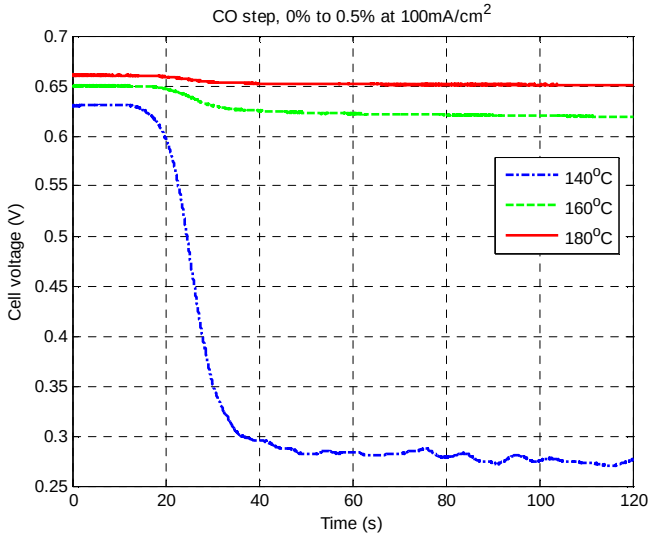

Figure 5.16. Voltage response for 0% to 0.5% CO steps.

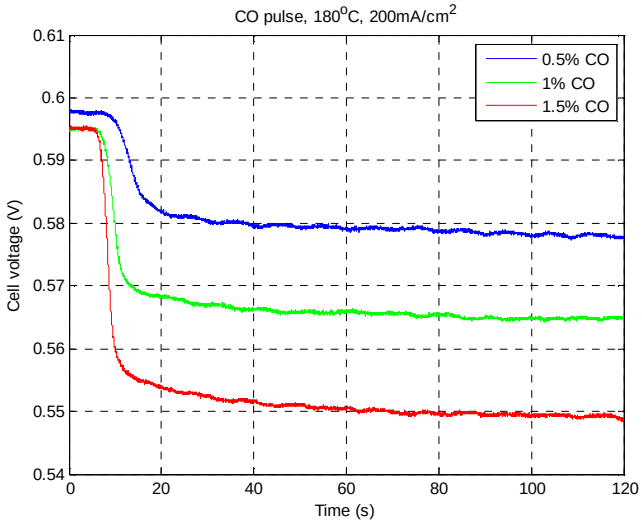

Figure 5.17. Voltage response for CO steps at 180°C.

The coverage of CO onto the platinum sites for these step changes in CO concentration can be modelled as follows [2]:

$$\rho_{pt}\frac{\partial\theta_{CO}(t)}{\partial t} = n_i\left[q_{ads,CO}(t) - q_{des,CO}(t)\right] - q_{ox,CO}(t) \tag{5.10}$$

Where θ_{CO} represents the time dependant catalyst coverage of CO, $q_{ads,CO}$, $q_{des,CO}$, $q_{ox,CO}$ the respective adsorption, desorption and electro-oxidation of CO and n_i the number of occupied catalyst sites per adsorbing molecule.

From the above relationship, it can be concluded that the equivalent circuit parameters change with time depending on the adsorption and desorption rate of the CO and as such it can be difficult to interpret for diagnostic purposes.

5.6 Performance Degradation and Recovery methods

The drop in performance during CO poisoning and the developed circuit models that can be used to track fuel cell state of health was presented in the previous sections. It is of interest to study the long term effects on performance and to develop possible mitigation strategies, specifically those that can be implemented in the power conditioning hardware where the detection algorithm is integrated with the system.

In order to test the long term stability of the cell after CO has been introduced and degraded performance, a series of tests were conducted at two different operating temperatures. The cell was subjected to CO poisoning at a constant current density of 200mA/cm^2 for a period of one hour in order to simulate a poisoning event that can occur. After this period, the CO was removed and the cell fed with pure hydrogen and polarization curves recorded after performance had stabilized. The polarization curves and power density curves for both 160°C and 140°C are presented in Fig. 5.18 before and after poisoning occurred. It is clear that there is a permanent drop in performance and that a percentage of the catalyst surface area did not recover after the CO was removed from the gas stream.

From the work in [23], it is known that stepping the fuel cell between two current set points promotes the oxidization of the CO and can recover performance. It is, however,

not ideal for the catalyst to undergo such aggressive load changes as this can enforce catalyst degradation. In order to determine a more optimal and natural waveform that can be implemented in the current control of the power conditioning hardware control loops, a series of tests were conducted on the setup. The test procedure was as follows: first, the cell is subjected to a 0.5% CO balance hydrogen mixture for a period of one hour. After this period, the cell was run at a constant current density with pure hydrogen for another hour and performance monitored to determine power loss. After this period, the cell was subjected to one of the active current control methodologies selected to try and recover performance. Once the recovery has been measured the complete procedure was repeated for the next current control method.

The first current profile tested was the hard switching between two load current set points that has been implemented in other works [9], [22] and [23]. The switching period of the load pulses was varied in order to determine what effect it will have on performance recovery. The voltage response for a 20s period is depicted in Fig. 5.19. The second load profile was a triangular wave with the same peak to peak current as the square pulse. This waveform most commonly represents that of a load ramp that may be employed in a dual input fuel cell system where batteries or super capacitors supply instantaneous current to the load while the fuel cell, acting as the base supply, is slowly ramped up. Finally, a more natural sinusoidal waveform was selected as this load profile produces the least amount of stress on the system.

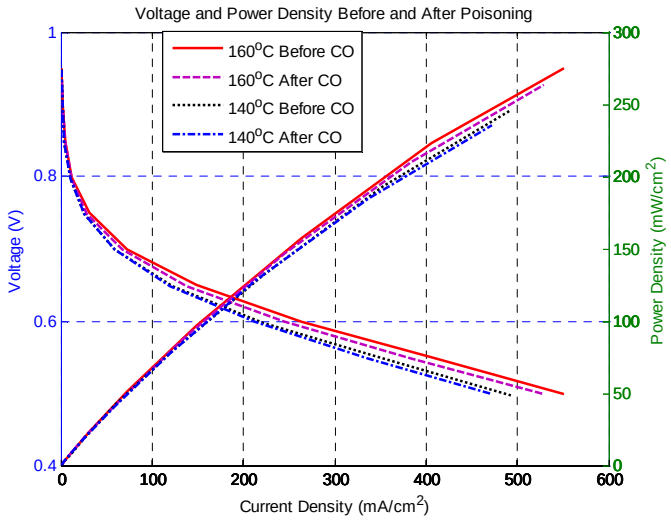

Figure 5.18. Drop in performance before and after CO poisoning.

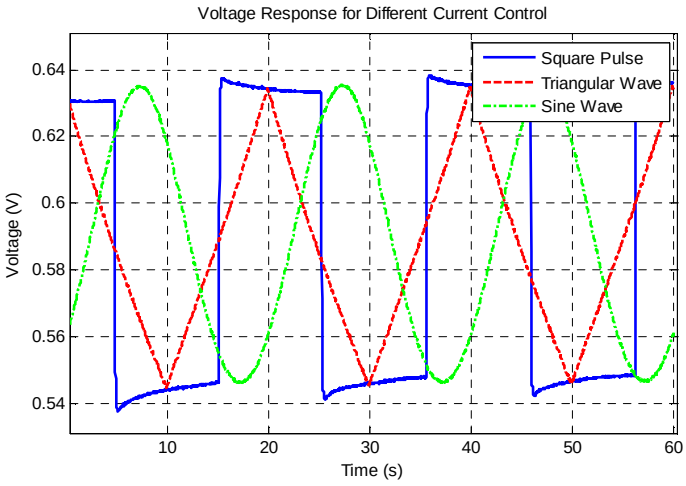

Figure 5.19. Voltage response for the selected current profiles.

The voltage responses for all the load current profiles are presented in Fig. 5.19. It is clear that the most aggressive waveform is the hard switched square pulse as it generates significant under and overshoots resulting in overpotentials on the electrodes that can cause permanent catalyst degradation. These types of load profiles are generally avoided in fuel cell systems and despite the proven ability to oxidize the CO and recover the platinum area, should not be implemented. The responses for the triangular and sinusoidal waveforms are less aggressive and will not enforce catalyst degradation to the same extent as the square pulses. As expected, the voltage responses do not produce significant over and undershoots and follow the corresponding current to a great extent.

The ability of the individual profiles to recover performance is illustrated in Fig. 5.20. As expected, there is a permanent drop in performance that cannot be recovered unless active current control is implemented with a set current profile. As illustrated in the figure, running the cell without CO for an hour did not have a significant impact on performance recovery. The increase in output power after the hard switched square pulse current profile was implemented demonstrates acceptable recovery with the saw tooth waveform showing similar performance recovery. It is clear from the experimental results that the sinusoidal waveform produced the greatest increase in power density with a total peak power increase of 5.65% when compared to the poisoned curves, as shown in Fig. 5.21. The triangular waveform achieved 3.67% and the square pulse 3.82% respectively. The sinusoidal waveform not only produced the best overall results for the oxidation of CO but is also the optimal waveform that will have the least effect on catalyst degradation, thus

not only recovering performance but also increasing life expectancy of the fuel cell.

The ability of the HT-PEM fuel cell to tolerate CO after each load control tested was investigated. The voltage profiles are presented in Fig. 5.22. Initially the cell behaved poorly with voltage and power dropping off significantly. After the mitigation strategies were implemented, the cell exhibited better performance retention after CO was introduced, with the sinusoidal waveform again delivering the best results.

The variation of applied current trajectory magnitude and frequency was evaluated. Higher current peak to peak amplitudes resulted in higher performance recovery as electro-oxidation of CO to CO_2 was improved. Higher frequencies resulted in lower performance recoveries and should be avoided as catalyst degradation can occur. The optimal performance recovery was obtained at the operating points presented in this chapter.

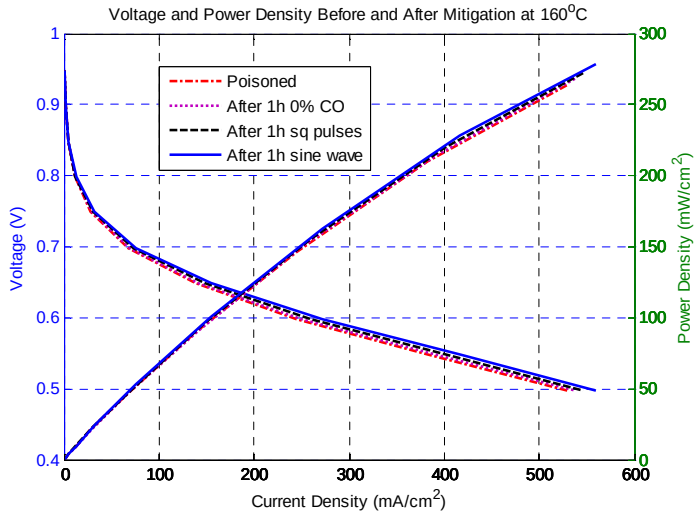

Figure 5.20. Performance recovery for the selected current profiles.

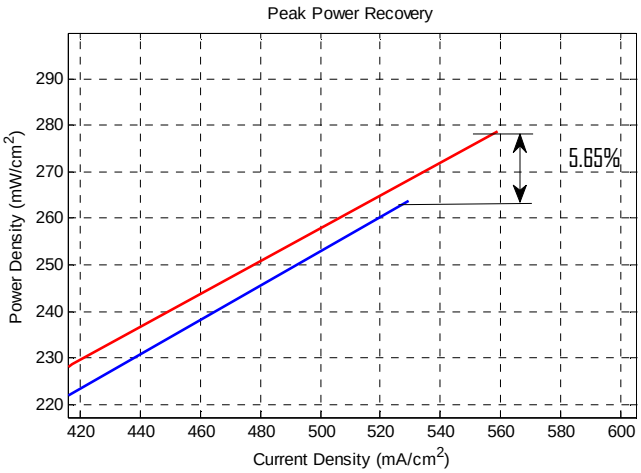

Figure 5.21. Maximum performance recovery achieved.

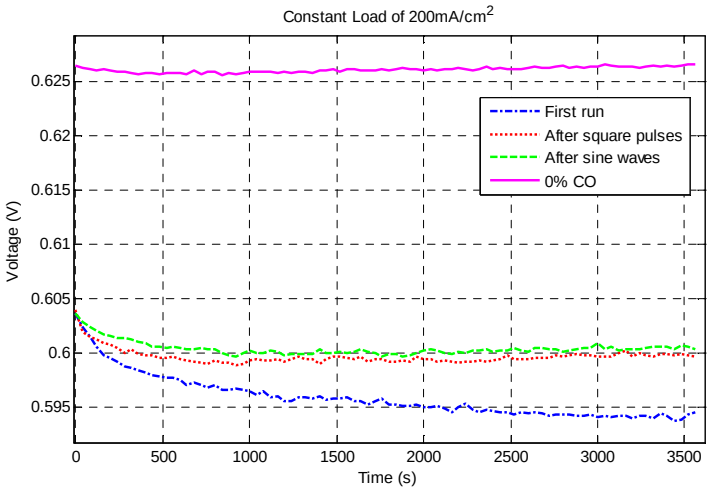

Figure 5.22. Voltage profiles during CO poisoning.

Conclusion

This chapter presents the results captured during a detailed study on the effect of CO poisoning on HT-PEM fuel cell performance. The cell performance was characterized using polarization curve analysis and EIS to determine the variation in steady state parameters for a wide range of operating conditions. The dynamic performance of the cell was investigated during the introduction of CO into the anode gas stream. Simple equivalent circuit models are used to model both the polarization curves and the EIS data and the circuit parameters that can be monitored by using diagnostic hardware in the power conditioning system are identified. The changes of these circuit parameters with variation in CO content are investigated and provide patterns for observer based control systems to diagnose the fuel cell condition of health. Based on the results, mitigation strategies were investigated to recover performance after CO poisoning has occurred. It is shown how a natural sinusoidal load profile provides better recovery results when compared to traditional hard switched load current profiles that have been proposed in previous work.

References

[1] J. J. Baschuk and Xianguo Li, "Carbon monoxide poisoning of proton exchange membrane fuel cells", *Int. J. Energy Res.*, vol.25, pp. 695- 713, 2001.

[2] A. Bergmann, D.Gerteisen, T. Kurz, 'Modelling of CO Poisoning and its Dynamics in HTPEM Fuel Cells", *Fuel Cells*, Vol. 10, No. 2, pp. 278-287, 2010.

[3] Søren Juhl Andreasen, Jakob Rabjerg Vang, Søren Knudsen Kær, "High temperature PEM fuel cell performance characterization with CO and CO2 using electrochemical impedance spectroscopy", *International Journal of Hydrogen Energy*, vol. 36, pp. 9815-9830, 2011.

[4] Jianlu Zang et al., "High Temperature PEM Fuel Cells", *Journal of Power Sources*, Vol. 160, pp. 872-892, 2006.

[5] Amrit Chandan et al., "High temperature (HT) polymer electrolyte membrane fuel cells (PEMFC) - A review", *Journal of Power Sources,* vol. 231, pp. 264-278, 2013.

[6] N. Wagner, "Characterization of membrane electrode assemblies in polymer electrolyte fuel cells using a.c. impedance spectroscopy", *Journal of Applied Electrochemistry*, vol. 32, pp. 859–863, 2002.

[7] Jinfeng Wua, Xiao Zi Yuan, Haijiang Wang, Mauricio Blanco, Jonathan J. Martin, Jiujun Zhang, "Review - Diagnostic tools in PEM fuel cell research: Part I Electrochemical techniques", *International Journal of Hydrogen Energy*, vol. 33, pp. 1735-1746, 2008.

[8] Seyed Mohammad Rezaei Niya, Mina Hoorfar, "Study of proton exchange membrane fuel cells using electrochemical impedance spectroscopy technique – A review", *Journal of Power Sources*, vol. 240, pp. 281-293, 15 October 2013.

[9] Abraham Gebregergis, Pragasen Pillay and Raghunathan Rengaswamy, "PEMFC Fault Diagnosis, Modeling and Mitigation", *IEEE Transactions on Industry Applications*, Vol. 46, No.1, pp. 295-303, 2010.

[10] Dhirde A.M., Dale N.V., Salehfar H., Mann M.D. and Han T.H., "Equivalent Electric Circuit Modeling and Performance Analysis of a PEM Fuel Cell Stack Using Impedance Spectroscopy," *IEEE Transactions on Energy Conversion*, vol.25, no.3, pp.778-786, Sept. 2010.

[11] Kim, J.; Lee, J.; Cho, B.H., "Equivalent Circuit Modeling of PEM Fuel Cell Degradation Combined With a LFRC," *IEEE Transactions on Industrial Electronics*, vol.60, no.11, pp.5086,5094, Nov. 2013

[12] Forrai, A.; Funato, H.; Yanagita, Y.; Kato, Y., "Fuel-Cell Parameter Estimation and Diagnostics," *IEEE Transactions on Energy Conversion*, vol.20, no.3, pp.668-675, Sept. 2005.

[13] Gebregergis, A.; Pillay, P., "Implementation of Fuel Cell Emulation on DSP and dSPACE Controllers in the Design of Power Electronic Converters," *IEEE Transactions on Industry Applications*, vol.46, no.1, pp.285-294, Jan.-feb. 2010.

[14] Raga, C.; Barrado, A.; Lazaro, A.; Fernandez, C.; Valdivia, V.; Quesada, I.; Gauchia, L., "Black-Box Model, Identification Technique and Frequency Analysis for PEM Fuel Cell with Overshooted Transient Response," *Power Electronics, IEEE Transactions on* , Available Online IEEE Xplore early access.

[15] Restrepo, C.; Konjedic, T.; Garces, A.; Calvente, J.; Giral, R., "Identification of a Proton-Exchange Membrane Fuel Cell's Model Parameters by Means of an Evolution Strategy," *Industrial Informatics, IEEE Transactions on*, Available Online IEEE Xplore early access.

[16] C. de Beer, P.S. Barendse and M.A. Khan, "Development of an HT PEM Fuel Cell Emulator Using a Multiphase Interleaved DC–DC Converter Topology," *IEEE Transactions on Power Electronics*, vol.28, no.3, pp.1120-1131, March 2013.

[17] Fei Gao, B. Blunier,D. Chrenko, D. Bouquain, A. Miraoui, "Multirate Fuel Cell Emulation With Spatial Reduced Real-Time Fuel Cell Modeling," *Industry Applications, IEEE Transactions on* , vol.48, no.4, pp.1127-1135, July-Aug. 2012.

[18] C. de Beer, P. Barendse, P. Pillay, B. Bullecks and R. Rengaswamy, "Online Fault Diagnostics and Impedance Signature Mapping of High Temperature PEM Fuel Cells Using Rapid Small Signal Injection", *Industrial Electronics Society, IECON 2013 - 39th Annual Conference of the IEEE* , pp.1798-1803, 10-13 Nov. 2013.

[19] R. Petrone et. Al, "A review on model-based diagnosis methodologies for PEMFCs", *International Journal of Hydrogen Energy*, vol.38, pp. 7077 -7091, 2013.

[20] Dachuan Yu, S. Yuvarajan, "Electronic circuit model for proton exchange membrane fuel cells", *Journal of Power Sources*, vol. 142, pp. 238-242, 2005.

[21] Ji-Rae Kim, Jung S. Yi, Tae-Won Song, "Investigation of degradation mechanisms of a high-temperature polymer-electrolyte-membrane fuel cell stack by electrochemical impedance spectroscopy", *Journal of Power Sources*, vol. 220, pp.54-64, 2012.

[22] Palma, L.; Enjeti, P., "A cost effective power converter to improve CO tolerance in PEM fuel cell power systems," *IEEE Power Electronics Specialists Conference*, PESC 2008, pp.210-215, 15-19 June 2008.

[23] Arthur H. Thomason, "Increasing The CO Tolerance of PEM Fuel Cells Via Current Pulsing and Self-Oxidation", Master's Thesis, Texas A&M University, 2004.

Chapter 6

Online Diagnostics of HT-PEM Fuel Cells Using Small Amplitude Transient Analysis

6.1 Introduction

Diagnostic systems have been the focus of recent research in order to increase system performance, life expectancy and reduce down time. Many model based diagnostic strategies for LT-PEM fuel cells have been proposed [1], [2]. These include highly complex multidimensional electrochemical models and black box approaches that use neural networks to estimate the state of health [3], [4], [5]. The drawback of these types of models and diagnostic algorithms is the high computational requirement making it difficult to employ in low cost controllers. A simpler approach is to make use of certain signal processing algorithms to try and isolate fault markers from the recorded voltage and current output of the fuel cell. These include standard harmonic analysis by using FFT [6] or discrete wavelet packet analysis [7], each yielding varying degrees of accuracy depending on the method and the transients analyzed.

The most widely recognized method for circuit parameter estimation and subsequent marker identification is electrochemical impedance spectroscopy (EIS) [8]-[12]. The

generated Nyquist plot is then typically fitted by means of an electrochemical equivalent circuit (EEC) as covered in the previous chapters. The total EIS measurement process takes upwards of several minutes to complete and requires dedicated hardware, such as a frequency response analyzer (FRA) to perform [13]. In order to reduce the measurement time, other methods have been proposed and include the use of PRBS and other signals [10]. These methods are still relatively complex and require a large data set to be effective.

The use of a small amplitude step response for parameter identification can be performed online with minimal change to the existing hardware and control in the power conditioning stage. The required measurement time for the response can be greatly reduced when compared to other diagnostic methods [6], [7]. In previous works, the transients were analyzed using curve fitting methods that are dependent on the selected circuit employed to model the response [14], [15].

Very little has been done to quantify the changes in transient voltage output in HT-PEM fuel cells and evaluate their use for fault marker identification. This chapter presents the voltage responses for a current pulse for varying operating conditions. A fault condition in the form of CO poisoning is introduced and the variation in the transient response is presented for variations in CO concentration. The S-transform is then used as a first step to extract fault markers from the transients. The S-transform has recently been used in electrical problems where the standard FFT, STFT and wavelet transform perform poorly [16], [17] as it has a number of advantages including better noise tolerance and fast computation times. The S-transform is a variation of the STFT as the Gaussian window is no longer fixed in width but dilates and translates [18].

The second step involves the extraction of parameters from the voltage response by employing non-linear least squares fitting based on a PBIL algorithm. The circuit and the associated transfer functions used to fit the experimental data are presented along with the variation in circuit parameters. The Nyquist plots derived from the step response are compared with those obtained from experimental EIS at the same operating conditions to verify performance.

6.2 HT-PEM Fuel Cell Diagnostics

6.2.1 Transient Response for Small Current Variations

In electrochemical system diagnostics, one of the primary tools available is EIS. This involves the connection of an FRA with a programmable electronic load to perform measurements. The equipment can be replaced by smaller power electronic circuits to reduce cost and ease of implementation [8]. A full spectrum EIS can take a number of minutes to perform and is not suited for fast online measurements [12]. As a result, other methods have been employed to reduce the measurement time and extract similar information from the measurements. Current interrupt (CI) has been used as an alternative to EIS to address some of the shortcomings [15], [19]. This method involves the loading of the fuel cell at a certain operating point and then disconnecting the load after which the voltage response is then measured and analyzed. The drawback of this method is that it cannot be performed while the fuel cell is in operation. Other methods were developed based on EIS and CI and include the use of PRBS excitation and associated analysis [13]. These require that the system operating parameters be kept constant, which may not always be possible. For online condition monitoring a more rapid measurement technique is required that will not significantly influence the cell operation. Existing fuel cell diagnostic methods, such as Current Interrupt and Cathode Discharge are thus not suitable.

As an alternative to the above methods, small current pulses have been used in PEM fuel cells to evaluate performance [1], [14], [20], [21]. Most of the studies, however, were performed under healthy conditions and very little work has been done on faulted or degraded systems. For HT-PEM fuel cells, limited studies are available due to the technology still being in development. In this chapter, the step responses of HT-PEM fuel cells will be analyzed for a range of operating conditions. To analyze the variation in the transient voltage under non-healthy conditions, the cell was subjected to various degrees of CO poisoning in the anode gas stream. It will be shown that there is a distinct variation in response as the fault mechanism is introduced, and in the following section methods will be employed to generate fault markers and track circuit parameter changes.

Typical voltage responses for a fuel cell that can be expected for a downward step in current are presented in Fig. 6.1. Similar to LT-PEM fuel cells, we can expect either an underdamped or overdamped response to the step change in current depending on the state of health. The first rise in voltage, which occurs almost instantaneously with the drop in current, represents the voltage drop across the ohmic resistance of the fuel cell. This is similar to the current interrupt method and the same analysis can be used for the smaller

amplitude transient. After the initial rise, the first stage of the transient state takes place and represents the change in concentration gradient at the surface of the catalyst layer in the electrode [22]. Depending on the system parameters, such as flow, temperature and gas composition, this part of the response will determine if the transient will have an overshoot. For healthier operation, it is expected that there will be an abundance of reactants at the catalyst layer and the voltage will rise above the final steady state value. Once all the reactants have been depleted, the response will enter the second transient state that will gradually drop or rise to the final steady state value. The initial transient typically takes place within the first second of the response while the second stage can take up to 10 seconds to complete [20]. Operation at higher temperatures increased the kinetic rate of the fuel cell reactions and it will be shown in the following sections that a 4 second response in HT-PEM fuel cells is adequate for diagnostic purposes.

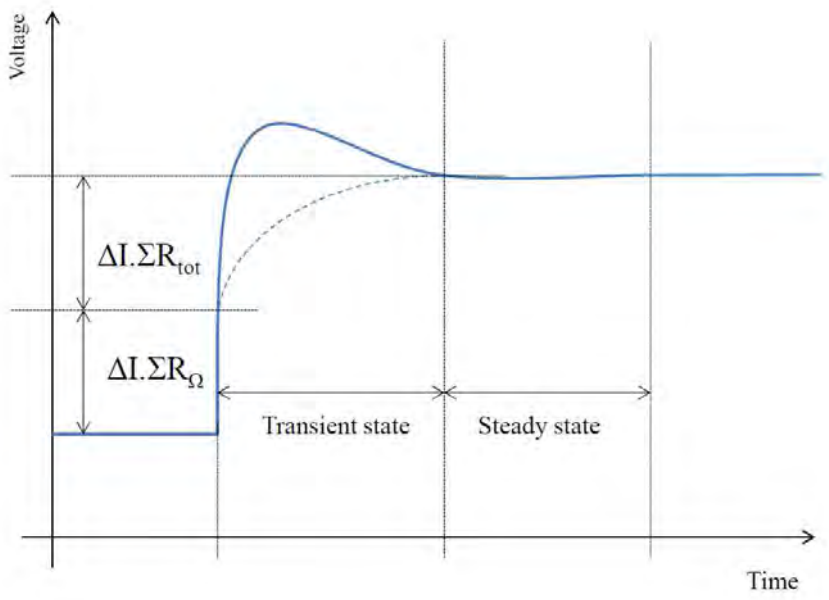

Figure 6.1. Transient voltage response.

6.2.2 Equivalent Circuit Representation

The analysis of the response requires that a model be fitted to the experimental data. For EIS and current interrupt, many electrochemical equivalent circuit models have been developed for PEM fuel cells, [10], [11] and more recently these have been adapted for HT-PEM systems [9]. Most fuel cells can be represented by a standard Randle's equivalent

circuit with a resistor and parallel resistor capacitor pair. To incorporate the diffusion of the reactants a Warburg element can be introduced, as shown in Fig. 6.2. This impedance element can be related to the mass transport resistance in EIS and is represented as follows:

$$\mathrm{Z_W} = \mathrm{Z_{W0}} \frac{tanh\sqrt{k\omega}}{\sqrt{k\omega}} \tag{6.1}$$

$$\mathrm{Z_{W0}} = \frac{RT\delta}{n^2F^2Sc^0D} \tag{6.2}$$

$$k = j\frac{\delta^2}{D} \tag{6.3}$$

Where R is the universal gas constant, T is the temperature in Kelvin, δ is the diffusion length, D is the diffusion coefficient in m^2/s, S is the active area in m^2, n is the electron number, F is the Faraday constant and c^0 is the concentration of the diffusion species. The Warburg element can be approximated by a series of parallel resistor capacitor pairs, as shown in the second circuit of Fig. 6.2.

To reduce complexity, the circuit can be simplified to a single resistor capacitor pair that is connected in series with the charge transfer elements, as shown in the last circuit of Fig. 6.2. To account for the change in surface concentration a pseudo inductive element must be introduced [22]. This is accomplished by placing a series inductor/resistor pair in parallel with the charge transfer circuit [23]. This represents the surface relaxation properties of the reactants and accounts for the underdamped behaviour in the transient response. Typically, in circuits used to reproduce the underdamped response, the inductor is placed in parallel with a resistor and in series with the other elements [9], [14]. This can only be done if the element represents a small amount of parasitic cable inductance in the circuit as this will influence the calculation and interpretation of the ohmic resistance in the circuit and analysis. As a consequence, the effect of the surface concentration gradient on the response is not properly analyzed and can influence the analysis of certain effects, especially mechanisms such as CO poisoning. The final circuit used to analyze the results in the following sections of this chapter is presented in the last diagram of Fig. 6.2.

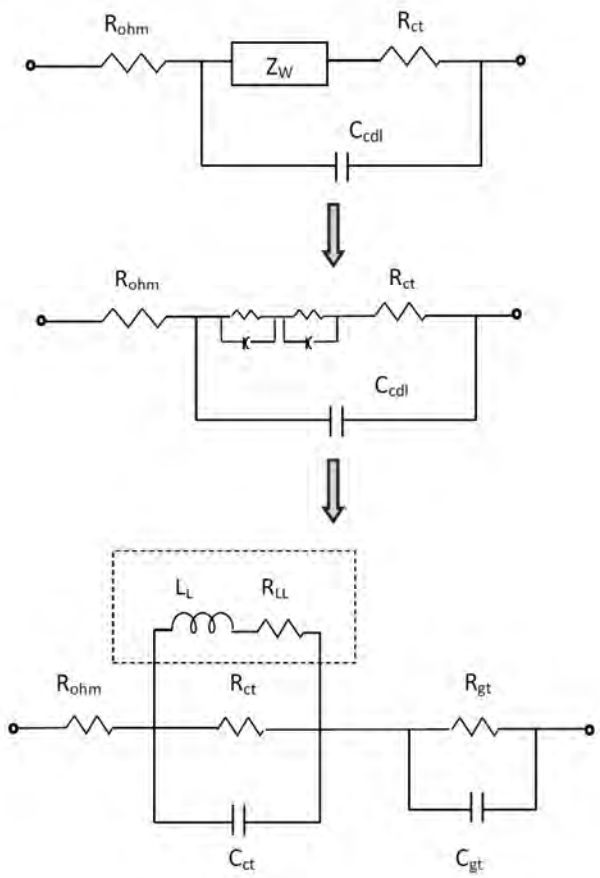

Figure 6.2. Derivation of the electrochemical equivalent circuit.

The series inductor/resistor pair represents the surface relaxation impedance during non-equilibrium state. The impedance can be represented with a potential dependant transfer reaction rate, *k*, and associated time dependant relaxation as follows [23]:

$$Z_L = \frac{1 + s\tau_K}{I_F d\frac{\ln k}{d\varepsilon}} \tag{6.4}$$

$$R_{LL} = \frac{1}{I_F d\frac{\ln k}{d\varepsilon}} \tag{6.5}$$

$$X_L = s\tau_K R_{LL} = sL_L \tag{6.6}$$

Where τ_K is the relaxation time constant, I_F the Faraday current and ε the relaxation potential. The total impedance for the selected circuit can be represented as follows:

$$Z_{tot} = R_{ohm} + \frac{Z_L R_{ct}}{Z_L + sC_{ct}R_{ct}Z_L + R_{ct}} + Z_{gt} \tag{6.7}$$

$$Z_{gt} = \frac{R_{gt}}{1 + sC_{gt}R_{gt}} \tag{6.8}$$

6.3 Embedded Diagnostic Hardware

Fig. 6.3 shows a typical online diagnostic and mitigation scheme for fuel cell systems, whereby the voltage and current is continuously monitored. Small load transients are then used to identify and classify possible fault conditions. This is accomplished by employing the proposed marker and parameter identification system presented in the following section. Fault marker calculation is performed as a first step by using appropriate time frequency resolution signal processing techniques. If certain marker thresholds are breached, the system will calculate the EEC parameters. This step provides detailed information regarding the fuel cell state of health and is used to perform fault classification whereupon mitigation strategies can be employed to reduce the effects on performance.

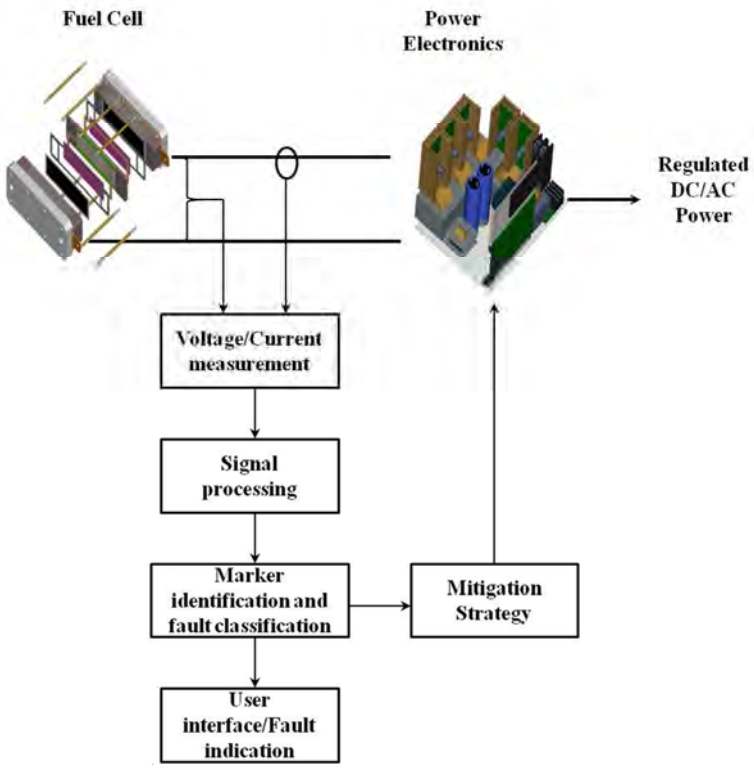

Figure 6.3. Typical fault detection/mitigation system.

A single fuel cell can be used to power certain devices that do not have a large voltage or power requirement, such as cellular phones. There does, however, need to be a power conditioning stage that will regulate the input voltage to the device. For a single cell, the open circuit voltage will be close to 1V, depending on the operating conditions. As the current density of the fuel cell increases, the output voltage will drop due to the internal loss mechanisms. As shown in chapter 4, the output voltage of a fuel cell can be represented by the reversible cell potential and the voltage loss components. Typical operating voltages of a single cell may range from 0.4V to 0.7V depending on the system. To increase the output voltage from the system, the cells can be placed in series. This arrangement is called a fuel cell stack and requires significant design and implementation expertise in order to ensure that operational problems, such as improper temperature distribution and gas distribution through the stack, are avoided. In comparison, the implementation of a single cell is less complex and the diagnostics easier to perform due to the reduced number of system variables.

The low voltages from a single cell present a challenge to most power converter designs as the parasitic losses in the converter hardware further reduces the voltage of the system as well as the efficiency. In order to minimize these losses, normal synchronous boost converters are typically employed and are designed whereby all parasitic elements are accounted for as shown in Fig. 6.4. For the converter to function, the selected switches must be able to operate below the 1V range and have an extremely low on-resistance. Other factors that must be taken into account are the start-up of the control circuitry and the design of the inductor [24]. For a given converter design, there will exist a maximum output power that the system can deliver. Operating beyond this value will lead to voltage collapse.

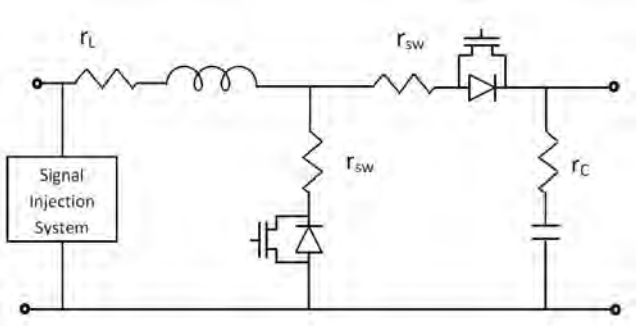

Figure 6.4. Synchronous boost converter with parasitic elements.

The maximum input current that can be drawn for a given output power before voltage collapse occurs can be calculated by solving the following quadratic equation [24]:

$$0 = RI_{in}^2 + \left(K + r_c \frac{P}{V_{out}} - V_{in}\right) I_{in} + P_{cc} + P - r_c \left(\frac{P}{V_{out}}\right)^2 \quad (6.9)$$

Where R is the sum of the trace resistances, the MOSFET on resistances and the inductor resistance. P is the output power, r_c is the capacitor series resistance and P_{cc} is the power required by the control circuit. K represents the switching losses of the MOSFETs.

If the signal injection system is required to operate in parallel with the DC-DC converter, as shown in Fig. 6.4, the power loss must be kept to a minimum in order to satisfy the relationship set out in (6.9).

6.4 Fault Marker Identification and Classification

A flow chart for the implementation of the proposed diagnostic system is presented in Fig. 6.5. The transient can be generated by the power electronic control system or by load variations and the voltage and current data recorded. After data acquisition, the S-transform (ST) is computed from the voltage data and the standard deviation of the ST amplitude matrix is determined, further details to be discussed in the proceeding section. The maximum standard deviation serves as the required fault marker and is compared with the expected value for a healthy cell at the same operating conditions. The deviation from the healthy value must fall within an acceptable tolerance band. Minor deviations that can arise from measurement inconsistencies are accounted for in this step. If the marker indicates a possible fault condition, the second phase of the algorithm can be executed. In the case of a severe system fault, whereby the marker is located in the upper range of measurement band, the master control can be forced to shut the fuel cell down to limit permanent damage. In the second stage of the system, the EEC parameters are estimated using the PBIL algorithm and compared against those of the healthy cell. The EEC gives significantly more information than the ST marker at the cost of calculation time. As such, it is only executed if the ST marker indicates a possible fault condition in order to avoid unnecessary computations. If the deviations for the critical EEC parameters are above the

thresholds, they can be compared to a database in order to diagnose the possible fault conditions. Once this has been done, a recommendation is made to the master control whereby appropriate action can be taken to limit system degradation and failure.

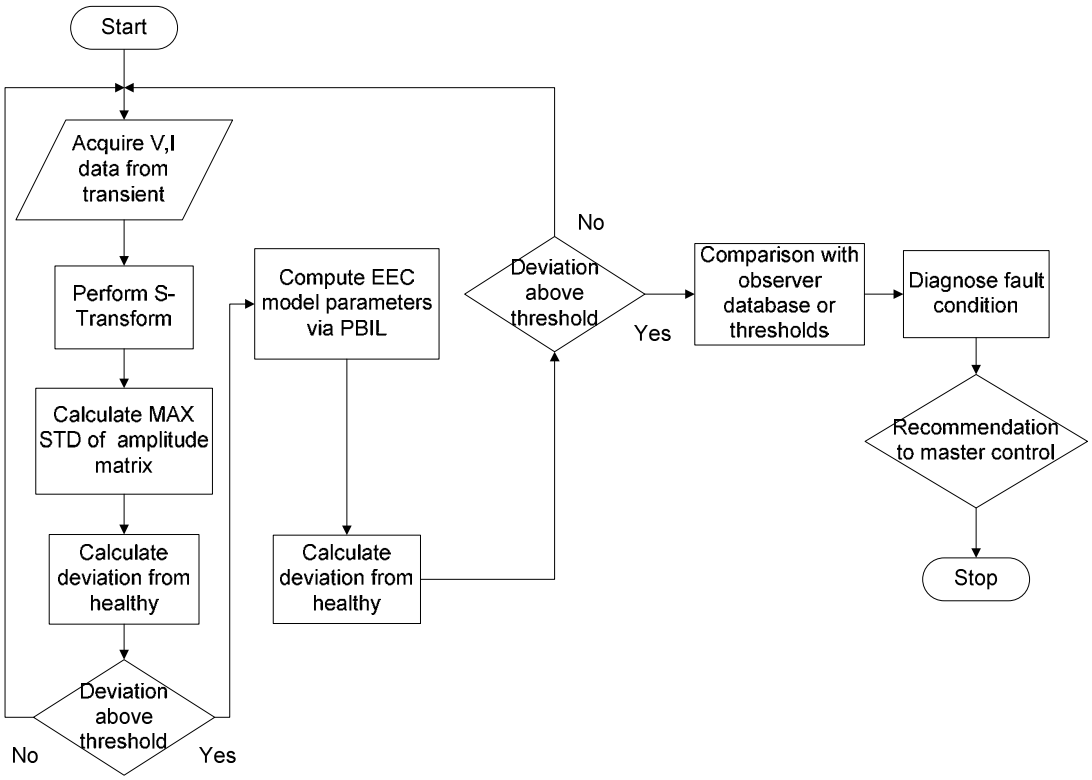

Figure 6.5. Flow chart of proposed diagnostic system.

6.4.1 Fault Marker Detection Using the S-Transform

The analysis of fuel cell state of health can be achieved by using signal processing methods. The most popular of these include the standard FFT and STFT. In the use of FFT, acceptable results can only be achieved if the signals that are being analyzed are stable and periodic. This method is thus not suitable for transient analysis in fuel cell diagnostics. Other methods that can perform time frequency localization can be used. These include the STFT and the wavelet transform.

The drawback of STFT is the fixed window size that limits the time frequency resolution, therefore the wavelet transform has been employed in fuel cell diagnostics to overcome these problems [7]. The wavelet transforms have some inherent drawbacks that can limit performance, which includes the computational complexity, sensitivity to noise

and the dependency on the chosen mother wavelet [17].

The ST can be used to resolve some of these limitations and has been applied in power quality analysis and fault detection [16], [17]. This transform has not been applied to fuel cell diagnostics and it will be shown how this transform can accurately calculate fault markers from the small amplitude step response. One of the advantages of the ST is its direct connection with the FFT, making it simple to implement and reduce computational effort that might be a requirement for implementation on a DSP. The ST allows the use of multiresolution strategy, similar to the wavelet transform by making use of a variable Gaussian window [25], [26]. It resembles the wavelet transform more closely than the STFT while maintaining the use of FFT in the calculations. For a continuous time signal *h(t)*, the ST can be defined as follows [18]:

$$S(\tau, f) = \int_{-\infty}^{\infty} h(t) w(\tau - t, f) exp(-i2\pi f t) dt \tag{6.10}$$

where the positive Gaussian window w is given as:

$$w(\tau - t, f) = \frac{|f|}{k\sqrt{2\pi}} exp\left(-\frac{1}{2}\left(\frac{(\tau - t)f}{k}\right)^2\right) \tag{6.11}$$

If the signal is sampled with a sampling time of T, the discrete form of $h(t)$ is given as $h(kT)$. The discrete FT of the signal is given as:

$$H\left[\frac{n}{NT}\right] = \frac{1}{N}\sum_{k=0}^{N-1} h(kT) exp\left(\frac{-j2\pi nk}{N}\right) \tag{6.12}$$

Where $n,k = 0,1,2,\ldots\ldots\ldots\ldots,N-1$ and N is the total number of samples in the data set. The discrete ST (DST) can be calculated as follows for the signal $h(kT)$:

$$S\left[kT, \frac{n}{NT}\right] = \sum_{m=0}^{N-1} H\left[\frac{m+n}{NT}\right] \exp\left(-\frac{2\pi^2 m^2}{n^2}\right) exp\left(\frac{j2\pi mk}{N}\right), n \neq 0 \tag{6.13}$$

For the zero voice $n = 0$, the DST is calculated as follows:

$$S[kT, 0] = \frac{1}{N}\sum_{m=0}^{N-1} H\left[\frac{m}{NT}\right] \tag{6.14}$$

The phase information of the ST is always referenced to time = 0, enabling the transform to combine the frequency dependant resolution with the absolute reference phase. The time average of the ST will thus equal the Fourier spectrum.

6.4.2 Fault Classification Using EEC Parameter Estimation

By using the small amplitude step response and the electrochemical equivalent circuit the parameters may be calculated to evaluate fuel cell performance and perform diagnostics. The transfer function presented in (6.7) can be used and the problem reduced to a control system parameter identification problem. In order to estimate the parameters the step response is calculated by using (6.7) and a fitness function *J*, defined in (6.15), is used:

$$J = \frac{1}{N}\sum_{i=0}^{N-1}(h(iT) - y(iT))^2 \tag{6.15}$$

Where N is the number of samples captured, $h(iT)$the discrete value of the captured signal and $y(iT)$ the calculated output of the estimator. The parameters of the impedance transfer function can be estimated by optimizing the presented least squares error function. A number of algorithms exist to perform function optimization of which the genetic algorithm (GA) is commonly used [27]. The standard GA relies strongly on the selection, mutation and crossover of the operators employed and can be complex to implement. More recently particle swarm optimization (PSO) and differential evolution (DE) has been employed specifically for fuel cell parameter estimation [28], [29], [30]. These still suffer from local minimization problems and therefore variations of the algorithms that are more complex to implement have been proposed. In this chapter, the use of a combination of the GA and simple competitive learning in the form of a population based incremental learning algorithm (PIBL), for fuel cell EEC parameter identification is proposed. The PBIL is very simple to implement and produces acceptable results when compared to other stochastic optimization methods.

In the PBIL, candidate solutions in the form of binary chromosomes are produced by

randomly sampling a probability vector (PV). At the start of the optimization, the elements of the PV are initialized to 0.5 for unbiased bit generation. For each iteration, the PV is updated by using a learning rate (LR) and the best solution (BS) of the population as follows:

$$PV = (1 - LR)PV + LR \times BS \tag{6.16}$$

To maintain diversity and reduce the chance for convergence to local minima, the probability vector must be relaxed. This is done by introducing a forget factor (FF) and relaxing the PV around a neutral value of 0.5. The relaxation is done as follows:

$$PV = PV - FF(PV - 0.5) \tag{6.17}$$

The implementation of the PBIL is done as set out below [31], with the control parameters and the individual circuit parameters in the solution vector set according to values and ranges as presented in table 6.1. Once the algorithm has determined the variation in the values, fault classification can be performed.

```
PV⟵ initialize probability vector. (Initially 0.5's)
loop # GENERATIONS

# Generate Trials
i⟵ loop #TRIAL
        trialᵢ⟵ generate sample vector according to probabilities in P
        evaluationᵢ⟵ evaluate (trialᵢ)

# Find Best Solution
max ⟵ find vector corresponding to maximum evaluation

# Update Probability Vector
I⟵ loop #LENGTH
        PI⟵ PI * (1.0 - LR) + maxI * (LR)

# Relax Probability Vector
I⟵ loop #LENGTH
if (random (0,1) < FF
        PI⟵ PI - FF*(PI -0.5)
```

TABLE 6.1
PBIL ALGORITHM PARAMETERS

Parameter	Unit	Value	Max
Population size	-	100	-
Generations	-	Variable	60
Resolution	bits	12	-
Learning Rate	-	0.1	-
Forget Factor	-	0.005	-
Rll	mΩ	Variable	100
Rct	mΩ	Variable	100
Rgt	mΩ	Variable	100
Cct	F	Variable	10
Cgt	F	Variable	100
Ll	H	Variable	10

6.5 Experimental Setup

The experimental setup used for this chapter was presented in chapter 3. The HT-PEM MEA was housed in a fuel cell technologies test fixture with integrated cartridge heaters. A temperature controller was connected to the cartridge heaters and tuned for precise set-point control. The individual test protocols were integrated with the global cell control algorithm in MATLAB. Chapter 5 presented the results and analysis of the polarization cures and EIS for CO poisoning. In this chapter, the focus will be on the small current load step response and the analysis thereof for the purpose of rapid diagnostics.

6.6 Results and Discussion

6.6.1 HT-PEM Fuel Cell Operation

The inherent advantages of operating the PEM fuel cell at higher temperatures are discussed in previous chapters. Fig. 6.6 presents the performance curves for three different operating temperatures as shown. For an increase in temperature, the proton conductivity of the membrane and the electrochemical kinetics are increased leading to greater power outputs. The other major advantages include the absence of liquid water and the increased tolerance towards contamination in the gas streams. For reformer fed operation the most likely contaminant is CO and the resulting drop in performance for a change in concentration can occur rapidly.

Fig. 6.7 presents the output voltage of the cell at two operating temperatures for a

change in CO concentration in the anode. The step command to the mass flow controllers was executed at 5s for a 0% to 0.5% CO concentration step. As expected it takes some time for the CO to enter the flow fields and diffuse through the gas diffusion layer to the reaction sites.

The voltage starts to drop rapidly as the CO is adsorbed onto the catalyst reducing the active surface area that can take part in the reaction. For an increase in temperature, the loss in performance is less profound. This is mainly due to the decrease in adsorption kinetics at increased temperatures for CO onto platinum. It is clear that the drop in performance for a change in CO concentration can occur quickly. For online diagnostics it is required that the technique be able to extract fault markers within a few seconds to enable proper control and minimize degradation effects. Standard methodologies such as EIS, polarization curve analysis and current interrupt are thus not adequate.

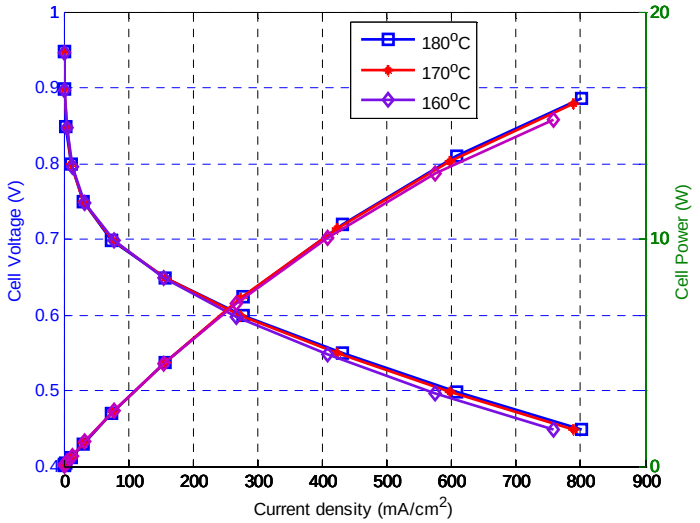

Figure 6.6. Polarization curves for temperature variation.

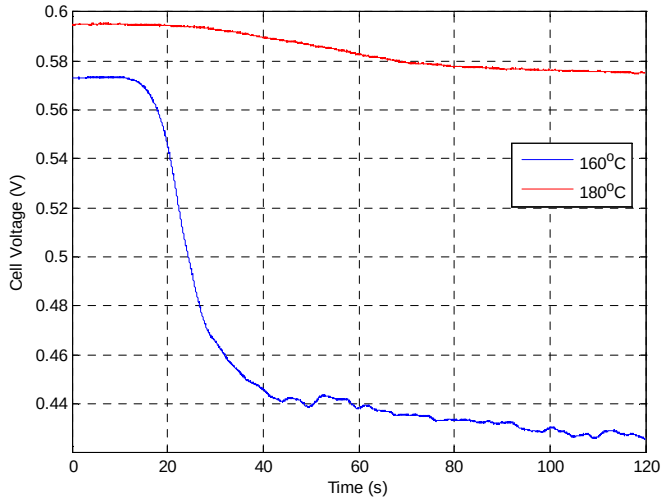

Figure 6.7. Cell voltage for 0% to 0.5% CO step.

6.6.2 Step Response Results

The step response tests were conducted under various operating conditions. A typical voltage response under healthy conditions for a step in load is presented in Fig. 6.8. The cell was allowed to reach steady state before a square pulse of 4s duration was applied to the load current. The voltage was then recorded for both the 4s pulse duration and an additional 4s after the pulse to produce an upward and downward curve, as shown in Fig. 6.8. The magnitude of the square pulse was set to 10% of the DC current operating point. This ensured that adequate signal to noise ratio was achieved while minimizing the effect on cell output. The response exhibits an underdamped response for both a step up and step down in load current. The initial change in voltage related to the ohmic voltage loss is visible and can be used to directly calculate the resistance by dividing by the magnitude of the current step. A two stage transient is present in the response. As stated in section 6.2.2, the drop/rise to the minima or maxima of the response can be related to the change in surface concentration at the reaction site due to the variation in load current and subsequent variation in the reaction rate. After the maxima or minima has been reached, the voltage will rise or drop to the final steady state value. The minimum amount of time that must be recorded to enable the cell voltage to reach steady state was determined to be 4s for both healthy and poisoned conditions.

To enable a direct comparison between the responses at varying load conditions, the cell voltages were normalized with respect to the magnitudes of the current steps. The voltage

data used in the following sections for variations in DC current set points are presented in Fig. 6.9. From the results it is clear that all the responses still exhibit and overshoot during the initial transient state. For an increase in load current, the difference between the peak voltage and the final steady state voltage magnitudes is reduced. This is to be expected as the reaction rate at the lower current densities is much lower and thus creates a greater gradient in surface concentration of the reactants. The same number of samples was recorded equating to 4s of data after the step change for all the tests. A sampling frequency of 500Hz was used and produced acceptable results in the calculations.

The results for the transient response of the voltage at different CO concentrations are presented in Fig. 6.10 at 160°C at an initial current of 200mA/cm^2. The change in magnitude from initial steady state to final steady state increases significantly for higher values of CO concentration. The response changes from underdamped to overdamped as the CO in the anode starts becoming significant. As more CO is introduced to the gas stream, the number of catalyst sites that are restricted increases as more CO is adsorbed. This reduces effective surface area and causes a drop in the reaction rate. This is evident from the time it takes the voltage response to reach new steady state conditions. The increased magnitudes give an indication that the resistive components in the equivalent circuit have significantly changed and will be shown in the following sections.

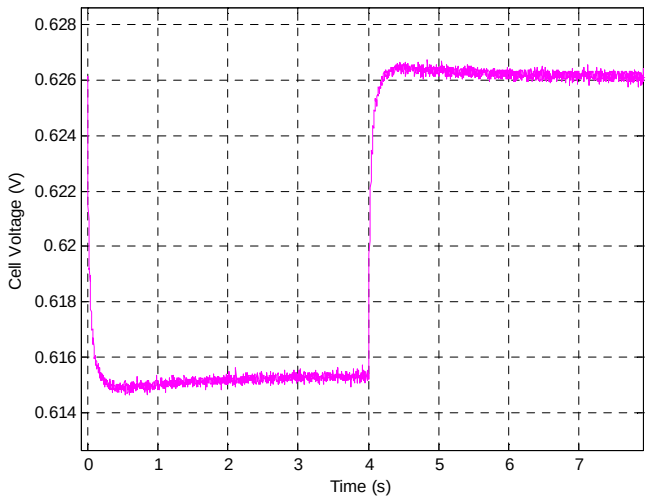

Figure 6.8. Voltage response for a current pulse.

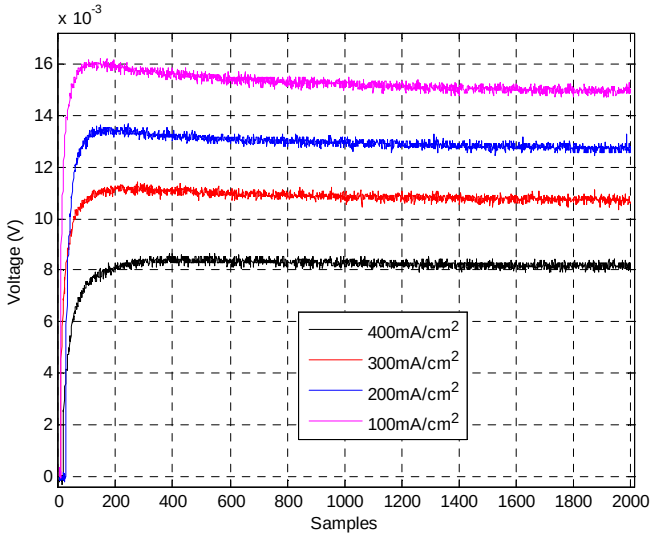

Figure 6.9. Normalized voltage response for different current densities.

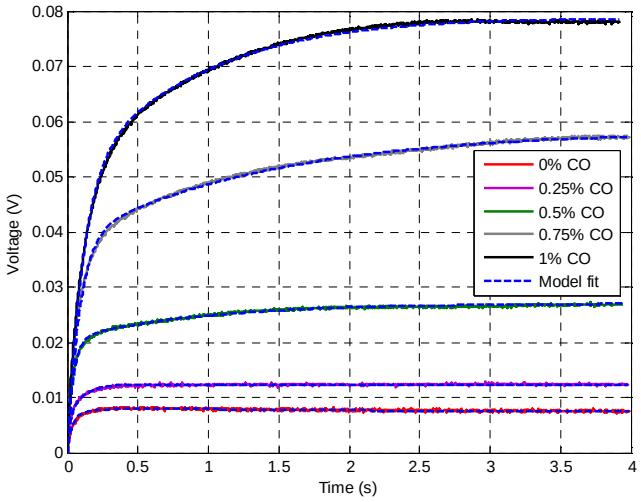

Figure 6.10. Normalized voltage response for different CO concentrations.

6.6.3 S-Transform Marker Calculation

Once the voltage response has been captured, the DST, as outlined in section 6.4.1, can be calculated. The DST is applied to the voltage transient for a CO concentration of 0.5% at 160°C and 200mA/cm² with the amplitude spectrum presented in Fig. 6.11. The high frequency components are concentrated within the first 100ms as expected for a step and the low frequency components are spread across the rest of the time range with decreasing magnitudes. Since the raw data of the DST matrix is difficult to interpret, statistical methods can be applied to generate results that are more meaningful. The standard deviation of the DST matrix across the 4s time range for the voltage responses shown in Fig. 6.10 is presented in Fig. 6.12. The standard deviation will be higher at the lower

frequencies, where the greatest voltage variation occurs as a result of the gas transport dynamics and associated impedances. This results in higher dispersion of the magnitudes of the low frequency components in the DST and produces low frequency peaks in the curves that can be related to the low frequency intercept on the Nyquist plot or total resistance of the EEC. The magnitude of these peaks for variation in CO concentration and cell temperature are presented in Fig. 6.13 and for healthy operation in Fig. 6.14. The trends produced are similar to those of the resistive components for the EEC estimated by the PBIL algorithm in the following section. It is clear that these markers are suitable to distinguish normal cell operation from more extreme operation and can act as the first fault marker in the condition monitoring system.

Higher cell temperatures clearly demonstrate an increased tolerance towards CO contamination as seen in the trends. Other fault mechanisms including flooding and drying in low temperature PEM fuel cells will produce similar usable markers from the DST for fault evaluation. If thresholds are set using the trends in the figures, it is clear that the cell can handle significantly more CO at higher temperatures before a fault condition is declared by the system. A simple observer based diagnostic system based on the DST and the associated standard deviation should be able to deliver adequate performance. For fault classification further information from the transient must be extracted, as will be discussed in the proceeding section.

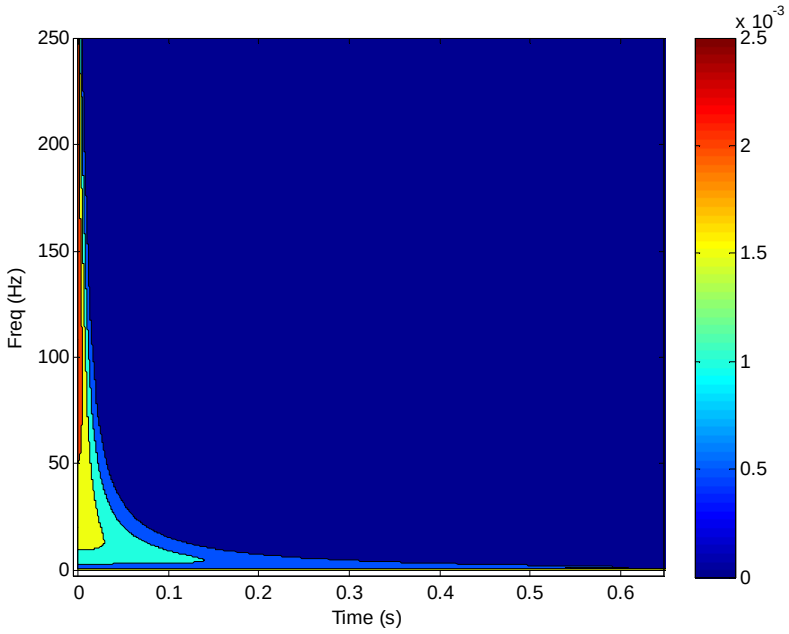

Figure 6.11. Amplitude spectrum of the S-transform applied to a downward voltage transient.

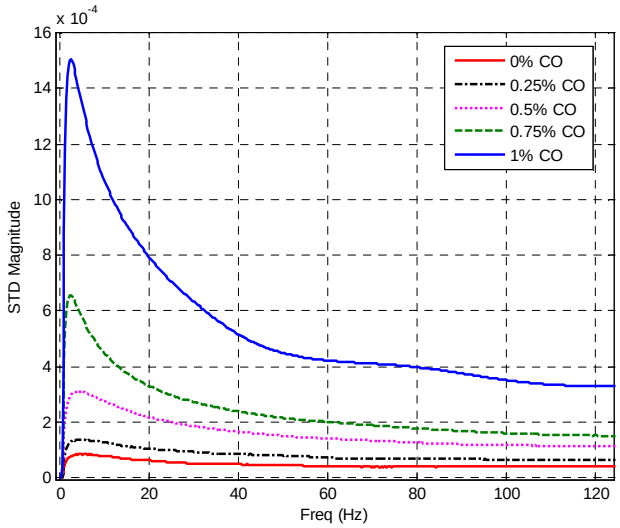

Figure 6.12. Standard deviation of S-transform matrix.

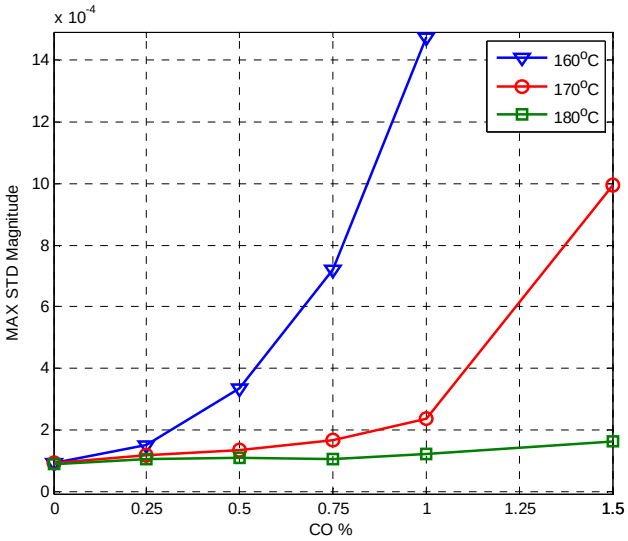

Figure 6.13. Variation of maximum STD of S-transform for CO.

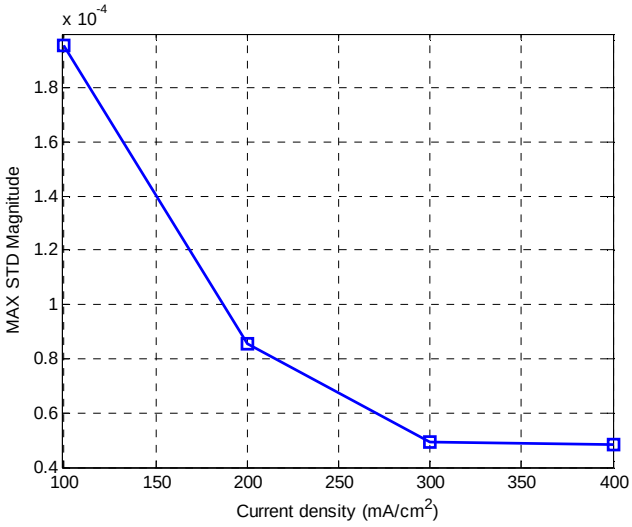

Figure 6.14. Variation of maximum STD of S-transform for current variation.

6.6.4 PBIL Based Parameter Estimation

The PBIL algorithm described in section 6.4.2 was implemented to determine the circuit parameters for the EEC. The forget factor in the algorithm was appropriately tuned to ensure the possibility for convergence to a local minima was reduced. One of the termination criteria for the algorithm was to fit the step response of the EEC to the experimental transient response with less than 2% error. Resulting fits from the algorithm to the experimental data for healthy and poisoned conditions are presented in Fig. 6.10. The model captures the initial overshoots well and then progresses to the undershooted behaviour exhibited by the poisoned response of the cell transients. In particular, the initial transient that occurs within the first second and the slower transient that takes place up until steady state is reached is matched, and confirms the viability of the applied EEC topology to capture the small amplitude transient behaviour for subsequent interpretation. The selected EEC does not capture very high frequency data that relates to the electrode structure. This can be included in the form of a third parallel RC circuit combination in series with the selected EEC topology. It was found that the inclusion of this additional element into the circuit does not give additional information on the state of health of the cell and causes unwanted variations in the calculated values of the other circuit parameters. The removal of the electrode circuit also ensures that the algorithm has fewer parameters to calculate and reduces calculation time.

The progression of the PBIL algorithm to convergence for two different operating points is shown in Fig. 6.15. For the healthier condition, the value of the fitness function is smaller when compared to the poisoned condition due to the smaller ranges of the parameters involved. It was found that the algorithm converged within 80 generations for the most extreme conditions with acceptable variation in EEC parameter values. For healthy conditions convergence took place within 40 generations. After termination of the algorithm, the Nyquist plots of the impedance were generated for the selected frequency band. The experimentally generated Nyquist plots from standard EIS, along with the calculated approximations from the transient responses, are presented in Fig. 6.16 for variations in current density under normal operating conditions. Good correlation exists between the plots generated by the two techniques and confirms the viability of the proposed EEC and parameter approximation method to perform diagnostics. As stated

previously, minor discrepancies exist in the high frequency region due to the removal of the equivalent electrode circuit from the EEC. Good approximations of the high frequency intercept relating to the ohmic resistance of the membrane of the fuel cell is made with minor variations due to the resolution of the DAQ and the small magnitudes involved in the transients.

The EIS Nyquist plots and the generated Nyquist plots from the small amplitude transient analysis for the poisoned conditions are presented in Fig. 6.17 and 6.18 for 160°C and 180°C respectively, with the associated parameter values presented in table 6.2. The trends exhibit very similar characteristics and the diameters of the respective arcs observed are in good agreement. It should be noted that in EIS curve fitting constant phase elements are usually employed in the equivalent circuits to improve the fit of the frequency response of the captured EIS data. Since normal capacitive elements are used in the transient response approximation presented in this work, the error between the plots is slightly increased. The extreme non-linear behaviour of CO poisoning causes unwanted effects on the captured responses in the EIS data sets. This causes difficulty in the interpretation of the arcs at the lower frequencies, as visually distinguishing the semicircles is limited by the resolution of the chosen frequency vector in the test. By using the transient analysis and the generated Nyquist plots, the semicircles become more apparent and assist with the diagnostics of the cell.

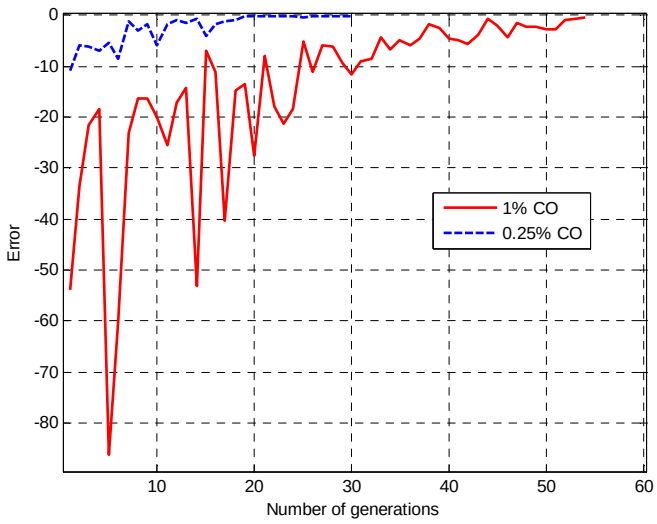

Figure 6.15. PBIL algorithm progression.

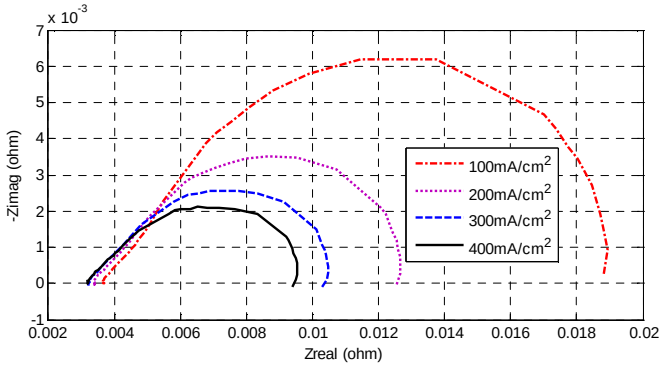

Figure 6.16a. Nyquist plots generated by EIS for current variation at 160°C.

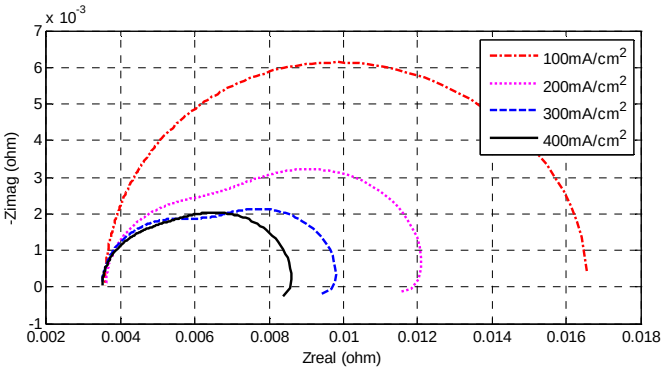

Figure 6.16b. Nyquist plots generated by PBIL EEC for current variation at 160°C.

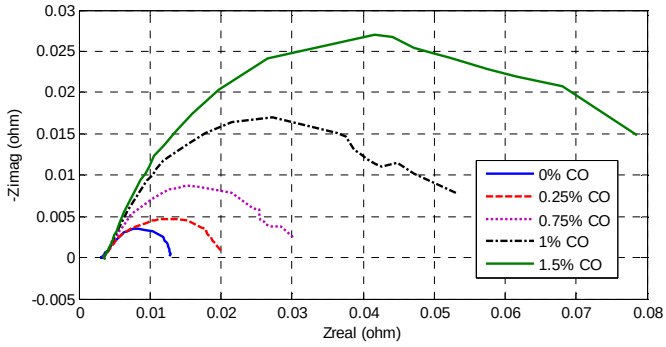

Figure 6.17a. Nyquist plots generated by EIS for CO variation at 160°C.

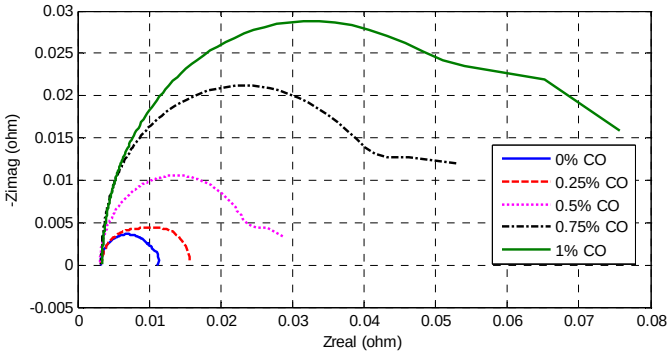

Figure 6.17b. Nyquist plots generated by PBIL EEC for CO variation at 160°C.

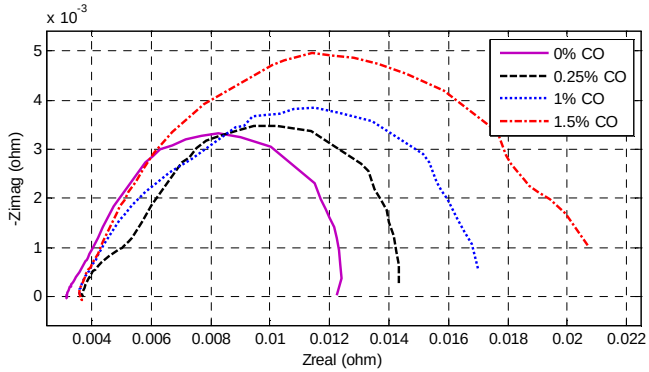

Figure 6.18a. Nyquist plots generated by EIS for CO variation at 180°C.

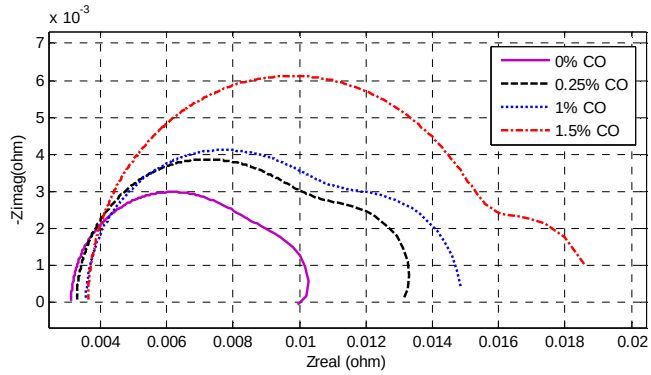

Figure 6.18b. Nyquist plots generated by PBIL EEC for CO variation at 180°C.

The calculated resistor values for the gas transport element and the total equivalent resistance in the EEC are presented in Fig. 6.19 and 6.20 respectively. As expected, the addition of CO has a small effect at very high temperatures on the magnitudes. At lower temperatures, where the addition of the impurity in the gas stream has a negative impact on the state of health, the increase in resistance is very prominent. The trends observed are similar to those obtained for the S-transform results. The max STD of the ST corresponds more closely with the variation of R_{tot} calculated by the PBIL algorithm while the variation of R_{gt} and other parameters provide more detail relating to specific fault mechanisms. Variation in current density during CO poisoning produced similar trends to those obtained in this chapter and chapter 5. Individual thresholds based on operational knowledge of the cell can be set on the values in an online condition monitoring system for SOH estimation and diagnostic purposes. For the CO poisoning condition presented in this chapter, the ohmic resistance varies very little as it does not have a significant effect on the membrane resistance. For other fault mechanisms such as acid leaching, or flooding and drying in low temperature PEM cells, this value will vary significantly and aids the

diagnostic system in distinguishing the individual fault when analyzing all the data presented in this chapter for the small amplitude transient response. The nature of the method allows for the use of natural load transients caused by loads switching or the use of the control in the power electronics to generate the small response for fault analysis and SOH estimation.

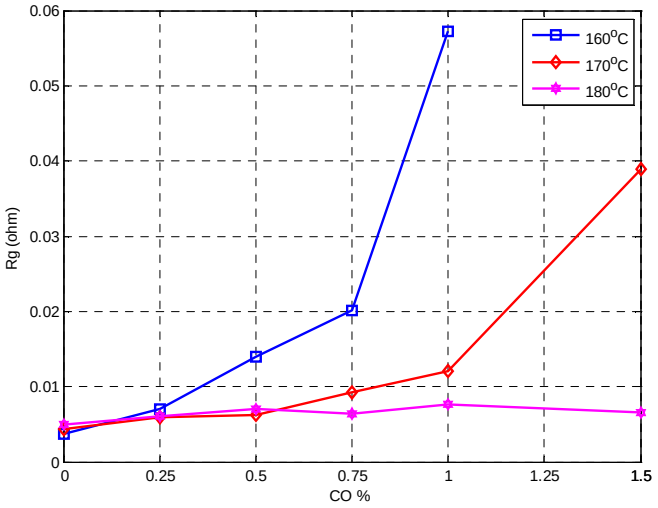

Figure 6.19. Variation of Rg for CO at different cell temperatures.

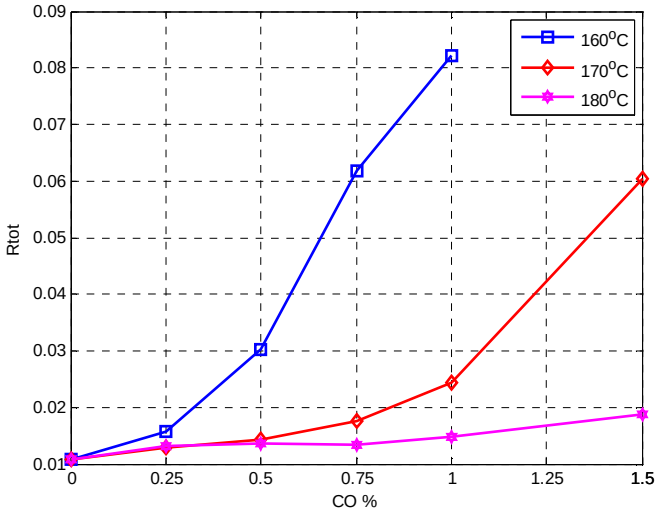

Figure 6.20. Variation of Rtot for CO at different cell temperatures.

TABLE 6.2
CALCULATED EEC PARAMETERS FROM STEP RESPONSE

CO	Icell (mA/cm^2)	Rohm (Ω)	Rk (Ω)	Lk (H)	Rct (Ω)	Cct (F)	Rgt (Ω)	Cgt (F)	Reff (Ω)	Rtot (Ω)
					160°C					
0	200	0.003256	0.0099	0.0087	0.0064	5.0757	0.0037	78.2227	0.003887	0.010843
0.25	200	0.003357	0.0896	0.0133	0.0057	3.0078	0.007	14.6729	0.005359	0.015716
0.5	200	0.003153	0.0389	0.0647	0.02	2.0532	0.0139	72.6563	0.013209	0.030262
0.75	200	0.003357	0.0974	0.0028	0.0631	2.5049	0.0201	69.3848	0.038292	0.061749
1	200	0.003456	0.0462	0.0462	0.0404	2.5146	0.0572	11.9385	0.021553	0.082208
					170°C					
0	200	0.002917	0.0078	0.0091	0.0071	4.6436	0.0043	91.6992	0.003717	0.010933
0.25	200	0.003459	0.0086	0.0051	0.0062	4.5874	0.0059	38.3789	0.003603	0.012962
0.5	200	0.003628	0.0096	0.0078	0.0085	5.0537	0.0063	67.6514	0.004508	0.014436
0.75	200	0.003662	0.0091	0.0078	0.0097	2.8271	0.0092	43.6279	0.004695	0.017557
1	200	0.003696	0.0193	0.0138	0.0157	2.5	0.0121	39.4043	0.008657	0.024453
1.5	200	0.003628	0.0406	0.0216	0.0316	2.4536	0.0389	15.5029	0.01777	0.060297
					180°C					
0	200	0.00312	0.0062	0.0043	0.0051	4.1211	0.005	34.3018	0.002798	0.010918
0.25	200	0.003289	0.0083	0.0053	0.0067	2.4927	0.0061	32.959	0.003707	0.013096
0.5	200	0.00356	0.0047	0.0082	0.0081	3.7695	0.007	77.4658	0.002974	0.013534
0.75	200	0.003696	0.0061	0.0096	0.0077	2.9639	0.0064	71.3623	0.003404	0.013499
1	200	0.00356	0.0089	0.0017	0.0064	2.4023	0.0076	16.9922	0.003723	0.014883
1.5	200	0.003628	0.0343	0.0253	0.0117	1.8457	0.0065	77.8809	0.008724	0.018852
					160°C					
0	100	0.003527	0.0072	0.0036	0.0084	4.7778	0.0091	20.4346	0.003877	0.016504
0	200	0.003594	0.005	0.005	0.0031	2.2607	0.0059	11.7432	0.001914	0.011408
0	300	0.003301	0.0072	0.0095	0.0028	2.4463	0.0037	17.3828	0.002016	0.009017
0	400	0.003001	0.0023	0.0079	0.0018	5.7837	0.0034	16.748	0.00101	0.007411

Conclusion

This chapter presents a new method for performing online diagnostics of a HT-PEM fuel cell using small amplitude transient analysis. The voltage responses for small current pulses of the HT-PEM fuel cell are presented for healthy and non-healthy conditions. CO poisoning of the anode gas stream was selected as the fault condition presented in this chapter. It was shown that the introduction of CO that can occur in certain conditions such as the start-up of a reformer is a high impact, fast reacting fault mechanism. The variation in the transient response for healthy and poisoned conditions are presented and evaluated. A new two stage approach for diagnostics based on the discrete S-transform and parameter estimation via PBIL is presented. The DST can generate valuable fault markers quickly as it is based on the standard FFT available in most modern DSPs. The fault

markers can be used as an initial estimation of the state of health before parameter estimation is performed. The PBIL algorithm presents a simple and effective way for equivalent circuit parameter estimation using the small amplitude transient response. The equivalent circuit and the required relaxation coefficients that relate to the underdamped behaviour of the cell are presented. The equivalent circuits are used to generate Nyquist plots of the calculated HT-PEM fuel cell impedance and compared with those obtained from conventional EIS. It was found that good correlation exists for both healthy and non-healthy conditions. The trends for the calculated resistances are comparable with those obtained from the DST analysis and prove the viability of both proposed methods.

References

[1] Adzakpa, K. P.; Agbossou, K.; Dube, Y.; Dostie, M.; Fournier, M.; Poulin, A., "PEM Fuel Cells Modeling and Analysis Through Current and Voltage Transient Behaviors," *Energy Conversion, IEEE Transactions on* , vol.23, no.2, pp.581,591, June 2008.

[2] R. Petrone, Z. Zheng, D. Hissel, M.C. Péra, C. Pianese, M. Sorrentino, M. Becherif, N. Yousfi-Steiner, "A review on model-based diagnosis methodologies for PEMFCs", *International Journal of Hydrogen Energy*, Vol. 38, Issue 17, pp. 7077-7091, 10 June 2013.

[3] X. Kong and A.M. Khambadkone, "Modeling of a PEM fuel-cell stack for dynamic and steady-state operation using ANN-based submodels," *IEEE Trans. Ind. Electron.*, vol. 56, no. 12, pp. 4903–4914, Dec. 2009.

[4] S. V. Puranik, A. Keyhani, and F. Khorrami, "Neural network modelling of proton exchange membrane fuel cell," *IEEE Trans. Energy Convers.*, vol. 25, no. 2, pp. 474–483, Jun. 2010.

[5] S. Jemei, D. Hissel, M. C. Pera, and J. M. Kauffmann, "A new modelling approach of embedded fuel-cell power generators based on artificial neural network," *IEEE Trans. Ind. Electron.*, vol. 55, no. 1, pp. 437–447, Jan. 2008.

[6] Z. Zheng a, R. Petrone a,c, M.C. Pe´ra, D. Hissel, M. Becherif, C. Pianese, N. Yousfi Steiner, M. Sorrentino, "A review on non-model based diagnosis methodologies for PEM fuel cell stacks and systems", *International Journal of Hydrogen Energy*, Vol. 38, Issue 21, pp. 8914–8926, 17 July 2013.

[7] Nadia Yousfi Steiner, Daniel Hissel, Philippe Mocoteguy, Denis Candusso, "Non intrusive diagnosis of polymer electrolyte fuel cells by wavelet packet transform*", International Journal of Hydrogen Energy* Vol. 36, Issue 1, pp. 740–746, January 2011.

[8] Ordonez, M.; Sonnaillon, M.O.; Quaicoe, J.E.; Iqbal, M.T., "An Embedded Frequency Response Analyzer for Fuel Cell Monitoring and Characterization," *Industrial Electronics, IEEE Transactions on* , vol.57, no.6, pp. 1925-1934, June 2010.

[9] S. J. Andreasen, J. L. Jespersen, E. Schaltz1, and S. K. Kær, "Characterisation and Modelling of a High Temperature PEM Fuel Cell Stack using Electrochemical Impedance Spectroscopy", *FUEL CELLS* , No. 4, pp. 463–473, 2009.

[10] Dhirde, A.M.; Dale, N.V.; Salehfar, H.; Mann, M.D.; Han, T.H., "Equivalent Electric Circuit Modeling and Performance Analysis of a PEM Fuel Cell Stack Using Impedance Spectroscopy," *Energy Conversion, IEEE Transactions on* , vol.25, no.3, pp. 778-786, Sept. 2010.

[11] Jonghoon Kim; Jaemoon Lee; Cho, B.H., "Equivalent Circuit Modeling of PEM Fuel Cell Degradation Combined With a LFRC," *Industrial Electronics, IEEE Transactions on* , vol.60, no.11, pp. 5086-5094, Nov. 2013.

[12] Xiaozi Yuan, Haijiang Wang, Jian Colin Sun, Jiujun Zhang, "AC impedance technique in PEM fuel cell diagnosis—A review", *International Journal of Hydrogen Energy*, Vol. 32, Issue 17, pp. 4365-4380, December 2007.

[13] M.A. Rubio, A. Urquia, R. Kuhn, S. Dormido, "Electrochemical parameter estimation in operating proton exchange membrane fuel cells", *Journal of Power Sources*, Vol. 183, Issue 1, pp. 118-125, 15 August 2008.

[14] Raga, C. ,Barrado, A., Lazaro, A., Fernandez, C.,Valdivia, V., Quesada, I., Gauchia, L., "Black-Box Model, Identification Technique and Frequency Analysis for PEM Fuel Cell with Overshooted Transient Response," *Power Electronics, IEEE Transactions on,* IEEE Xplore early access.

[15] M.Jung, M.D. Ashford, K.A. Williams, "Analysis of a fuel cell system by a step response", *FUEL CELLS*, No.2, pp. 327-338, 2011.

[16] Ahmadimanesh, A.; Shahrtash, S.M., "Transient-Based Fault-Location Method for Multiterminal Lines Employing S-Transform," *Power Delivery, IEEE Transactions on* , vol.28, no.3, pp.1373-1380, July 2013.

[17] Fengzhan Zhao, Rengang Yang, "Power-Quality Disturbance Recognition Using S-Transform," *Power Delivery, IEEE Transactions on* , vol.22, no.2, pp.944,950, April 2007.

[18] R. G. Stockwell, L. Mansinha, and R. P. Lowe, "Localization of the complex spectrum: The S transform," *IEEE Trans. Signal Process.*, vol. 44, no. 4, pp. 998–1001, Apr. 1996.

[19] M.A. Rubio , A. Urquia, S. Dormido, "Diagnosis of PEM fuel cells through current interruption", *Journal of Power Sources*, Vol. 171, Issue 2, pp. 670–677, 27 September 2007.

[20] Junhyun Cho, Han-Sang Kim, Kyoungdoug Min, "Transient response of a unit proton-exchange membrane fuel cell under various operating conditions", *Journal of Power Sources*, Vol. 185, Issue 1, pp. 118-128, 15 October 2008.

[21] Marignetti, F.; Minutillo, M.; Perna, A.; Jannelli, E., "Assessment of Fuel Cell Performance Under Different Air Stoichiometries and Fuel Composition," *Industrial Electronics, IEEE Transactions on* , vol.58, no.6, pp. 2420-2426, June 2011.

[22] Sunil K. Roy, Mark E. Orazem, and Bernard Tribollet, "Interpretation of Low-Frequency Inductive Loops in PEM Fuel Cells", *Journal of The Electrochemical Society*, Vol. 154 no.12 pp. B1378-B1388, 2007.

[23] N Wagner, E Gülzow, "Change of electrochemical impedance spectra (EIS) with time during CO-poisoning of the Pt-anode in a membrane fuel cell", *Journal of Power Sources*, Vol. 127, Issues 1–2, pp. 341-347, 10 March 2004.

[24] Jonathan W. Kimball, Theresa L. Flowers and Patrick L. Chapman, "Low-Input-Voltage, Low-Power Boost Converter Design Issues", *IEEE Power Electronics Letters*, Vol. 2, no.3, September 2004.

[25] R.G. Stockwell, "A basis for efficient representation of the S-transform", *Digital Signal Processing*, Vol. 17, Issue 1, Pages 371–393, January 2007.

[26] Ventosa, S.; Simon, C.; Schimmel, M.; Danobeitia, J.J.; Manuel, A., "The S -Transform From a Wavelet Point of View," *Signal Processing, IEEE Transactions on* , vol.56, no.7, pp. 2771-2780, July 2008.

[27] Yang, S.Y.; Ho, S.L.; Ni, G.Z.; Machado, J.M.; Wong, K. F., "A New Implementation of Population Based Incremental Learning Method for Optimizations in Electromagnetics," *Magnetics, IEEE Transactions on* , vol.43, no.4, pp. 1601-1604, April 2007.

[28] Qi Li; Weirong Chen; Youyi Wang; Shukui Liu; Junbo Jia, "Parameter Identification for PEM Fuel-Cell Mechanism Model Based on Effective Informed Adaptive Particle Swarm Optimization," *Industrial Electronics, IEEE Transactions on* , vol.58, no.6, pp.2410-2419, June 2011.

[29] Alotto, P.; Guarnieri, M., "Stochastic Methods for Parameter Estimation of Multiphysics Models of Fuel Cells," *Magnetics, IEEE Transactions on* , vol.50, no.2, pp.701-704, Feb. 2014.

[30] Askarzadeh, A.; Rezazadeh, A., "An Innovative Global Harmony Search Algorithm for Parameter Identification of a PEM Fuel Cell Model," *Industrial Electronics, IEEE Transactions on* , vol.59, no.9, pp.3473-3480, Sept. 2012.

[31] Baluja Shumeet, "Population-based incremental learning: A method for integrating genetic search based function optimization and competitive learning". No. CMU-CS-94-163. Carnegie-Mellon Univ Pittsburgh Pa Dept of Computer Science, 1994.

Chapter 7

Fuel Cell Condition Monitoring Using Optimized Broadband Impedance Spectroscopy

7.1 Introduction

To ensure that the fuel cell is operating optimally, it is vital to monitor and evaluate the inner phenomena of the fuel cell for steady state and transient conditions. As discussed in the previous chapters, the most well known electrochemical methods used for diagnostic purposes include polarization curve analysis, current interrupt, cyclic voltammetry and electrochemical impedance spectroscopy (EIS) [1-[3].

EIS can be used while the fuel cell is operational. Standard EIS uses a frequency response analyzer (FRA) to induce the required perturbation over the frequency range of interest [4]. To reduce the cost of EIS implementation, a lower cost platform has been developed whereby the electronic load is used to control the current profile [5]. This was further improved by designing a low cost embedded analyzer in [6]. The EIS measurement procedure can take upwards of several minutes to complete as each frequency harmonic is individually introduced to the fuel cell to limit disturbance [7]. To overcome this

limitation, methods have been proposed whereby wider frequency band signals are used to measure the impedance response while minimizing measurement time. This includes the use of binary sequence signals such as PRBS and MLBS and chirps [8]-[14]. The disadvantages of many of these methods are that they require complex algorithms to compute the magnitude and phase of the frequency spectrum and loss of accuracy due to unwanted frequencies being excited. To overcome these problems, the broadband multisine signal has been used in the biomedical field to measure bioimpedance in living tissue [15], [16]. A short band multisine was used to reduce the measurement time of EIS in fuel cells in [5] but had a number of limitations including large peak to peak magnitudes of the injected signal profile.

This chapter proposes a new method for fuel cell condition monitoring by using optimized broadband impedance spectroscopy (OBIS). The designed OBIS is applied to the fuel cell by using a simple low cost hardware platform for embedded measurement and diagnostics. The system performance is compared with a commercial FRA using standard EIS. To prove viability for online condition monitoring, the system is tested on an LT-PEM fuel cell that is subjected to fast occurring, high impact fault conditions such as flooding, drying and reactant starvation. It is shown that under extreme non-linear conditions, such as flooding, the OBIS system is able to produce impedance measurements that are not obtainable using conventional methods. The following section evaluates the internal water transport mechanisms of LT-PEM fuel cells. Section 7.3 details the design procedure of the proposed OBIS signal. Section 7.4 presents the embedded hardware platform and the experimental test setup is presented in section 7.5. Section 7.6 presents the experimental results and discussions whereupon conclusions are drawn.

7.2 Water Transport in LT-PEM Fuel Cells

To enable adequate operation and performance, LT-PEM fuel cells require humidification of the membrane which is achieved by humidifying the reactant supplies or by direct liquid hydration [17]. This coupled with the internal water generation mechanism and water transport across the membrane can give rise to a number of operational problems [18]. The most common of these include the flooding and drying effects. This is strongly influenced by the reaction rates of the cells and the flow rates of

the gasses. High flow rates and low reaction rates can lead to under humidification of the membrane causing it to dry out and substantially decrease in ionic conduction and increase the resistive losses. Low flow rates coupled with a high reaction rate can cause an accumulation of water. The cathode side is particularly susceptible to this due to the Oxygen reduction. Large amounts of water accumulation can lead to flooding and can cause extreme non-linear behaviour and system instability. Other fault mechanisms can include fuel starvation due to insufficient gas supply rates from both the anode or cathode mass flow control systems and hydrogen crossover across the membrane.

Fig. 7.1 represents a typical schematic of an LT-PEM fuel cell and the internal water transport. The water transport dynamics are governed by three main mechanisms and include the water generated on the cathode side by the reaction, back diffusion, and electro-osmotic drag [17]. Back diffusion results from the water concentration gradient across the membrane with water diffusing from the high concentration (cathode) to the low concentration (anode). Water is transported from the anode to the cathode via eletro-osmotic drag caused by the migration of the hydrogen ions to the cathode side during the reaction.

The variation of water content in the LT-PEM fuel cells has a significant impact on performance. This can most easily be demonstrated by recording polarization curves for both an upward and downward sweep in current. As shown in Fig. 7.2, the curves do not overlay and can indicate either flooding or drying of the MEA. In the case of low relative humidity (RH), the cell will have low internal water content at the start of the upward sweep in current. At the end of the sweep, where the current density is high and water production is increased, membrane conductivity will improve, causing the curve for the downward sweep in current to produce higher output voltages.

The resistance of the cells is dependent on the characteristics of the membrane and is calculated in a similar manner as in (4.22). The membrane conductivity is dependent on the water content as follows:

$$k_m = b_1 exp\left[(b_2 \times \lambda_m - b_3)\left(\frac{1}{303} - \frac{1}{T_{cell}}\right)\right] \tag{7.1}$$

Where λ_m is the membrane water content and b are empirical parameters [2].

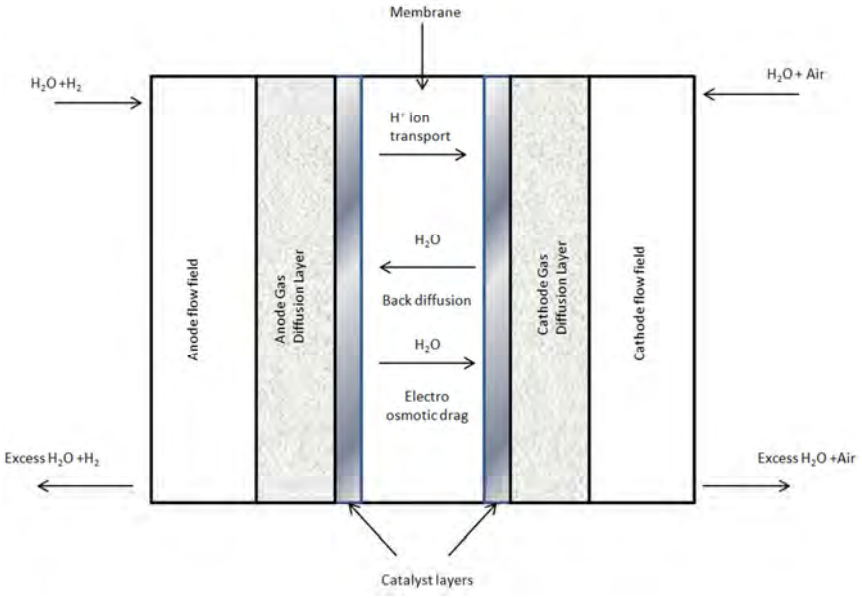

Figure 7.1. Schematic of water transport inside a PEM Fuel Cell.

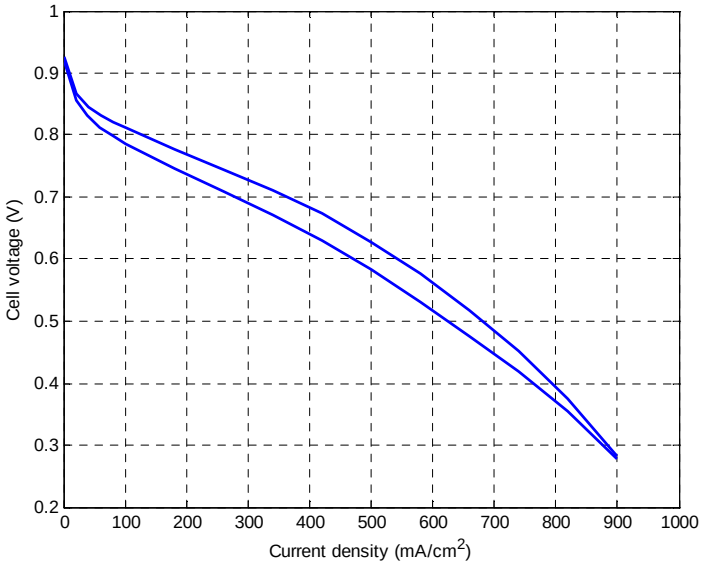

Figure 7.2. Polarization curve hysteresis of an LT-PEM Fuel Cell.

7.3 Optimized Broadband Signal Design

Classical EIS requires measurement time that makes it unsuited to monitor fuel cell state of health during non-linear operation, which typically occurs during fault conditions. For the measurements to be acceptable, conditions such as the Kramers-Kronig relations must be met. These include linearity, stability and causality [19]. Another aspect to consider is

the amplitude of the injected signal. In general, the larger the amplitude and signal power introduced, the greater the SNR of the measured data. For the fuel cell response to adhere to the Kramers-Kronig relations, the amplitude of the signals must be small enough to ensure that the response is still within the acceptable linear regions and to avoid any non-linearities that may occur. This requires that the excitation signal must be designed to maximize power at the frequencies of interest while minimizing system disturbance. The advantage of the multisine is that it maintains the characteristics of the regular sine wave and allows the user to control the amplitude and frequency spectrum such that only the desired frequency set is excited. Other broadband signals, such as binary length sequences and chirps have substantial amounts of spectral leakage and results in unwanted frequencies being excited.

For a real valued multisine, the time domain expression is a Fourier series of order *N*:

$$u(t) = \sum_{n=0}^{N-1} a_n cos(2\pi f_n t + \varphi_n) \tag{7.2}$$

Where N is the number of frequencies in the signal, a_n is the amplitude matrix, f_n the excited frequencies and φ_n the phase matrix. The standard random phase multisine can have very large peak to peak or crest factor magnitudes. The phase vector of the selected frequency set can be varied in order to optimize this value. In this chapter, the OBIS signal is optimized in three stages. The first is the frequency set distribution that will minimize signal time and maximize the resolution of the measured impedance. The second part determines the magnitudes of the harmonic spectrum at the selected frequencies to maximize signal energy. The last stage minimizes the magnitude of the signal in the time domain using the crest factor and non-linear optimization.

7.3.1 Frequency Distribution

For EIS to yield an acceptable impedance spectrum, the number of exciting frequencies must be selected to ensure that the resolution is adequate to distinguish the key features. Unlike bioimpedance, where the frequency range of interest is in the kHz to MHz range, fuel cell impedance contains significant information in the low Hz and sub Hz frequencies.

At these frequencies, the gas transport phenomena relating to various mechanisms in the electrochemistry become visible. For fuel cell EIS, the frequency band of interest lies within the 0.1Hz to 20kHz band [1]. For a periodic multisine, the minimum frequency will determine the signal length and must be kept to a minimum. Depending on the state of health of the system, the frequency where the impedance crosses the real axis may vary. Shorter signal times can be achieved if the lowest excited frequency is increased. If the impedance does not reach the real axis intercept, interpolation techniques can be applied to estimate the value. It was found in this work, that a minimum frequency of 0.25Hz was adequate to reach the intercept, as will be shown in the following sections. Consequently, a minimum signal length of four seconds is required to apply the Discrete Fourier Transform (DFT) on the OBIS signal.

To determine the frequency distribution, some prior knowledge regarding the magnitude response of the impedance is required. A typical magnitude response for a healthy cell is presented in Fig. 7.3. It is clear that the rate of change between 1Hz and 100Hz is significant when compared to the rest of the spectrum. To ensure that the Nyquist plot has acceptable resolution, a linear-logarithmic-linear distribution is proposed. The harmonic number and the corresponding exciting frequencies are presented in Fig. 7.4. In the sub Hz region, the distribution must ensure that aliasing and spectral leakage is minimized. This can be accomplished by appropriately distributing the lower frequency band to ensure that the DFT zeroes for each excited frequency in the spectrum. A linear distribution, with a minimum frequency selected as the inverse of the total signal time, can be used. While the linear distribution will ensure that maximum resolution will be obtained, non-linearities in the fuel cell can introduce second order harmonics at the fundamental frequencies [15]. For this reason, a logarithmic function for the excited frequencies is used in the centre frequency band where the greatest change in the magnitude response takes place. For the high frequency region, a linear distribution is again followed to minimize signal complexity. The employed frequency distribution can be determined as follows:

$$fn = \begin{cases} F_b + nF_0 & for\ 0 \le n < A \\ 10^{\left(F_b/\alpha\right)\times(n-\beta)} & for\ A \le n \le B \\ 100(n+2-B) & for\ B < n \le N-1 \end{cases} \tag{7.3}$$

$$A = \frac{2 - F_b}{F_0} \tag{7.4}$$

$$B = \frac{2.477\alpha}{F_b} + \beta \tag{7.5}$$

Where F_b = 1/(signal time), F_0 = 2×F_b and n = 0,1,2….N-1. The coefficients α and β are selected to ensure that the distribution does not repeat frequencies and that the piece wise derivative is greater than F_0 to ensure spectral leakage is minimized. For F_b=0.25Hz, α is selected as 2 and β as 0.5. The total number of frequencies, N, used in the OBIS signal should be chosen to minimize signal complexity while maximizing resolution and impedance information, as will be shown in the following sections.

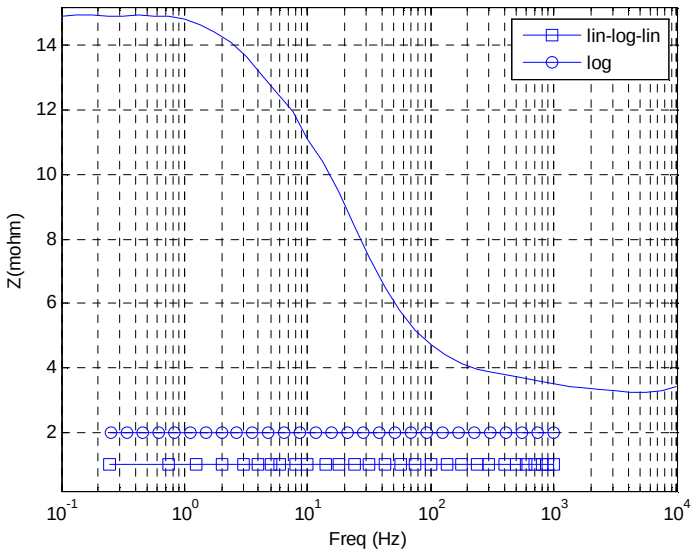

Figure 7.3. Fuel cell magnitude response and measurement distribution.

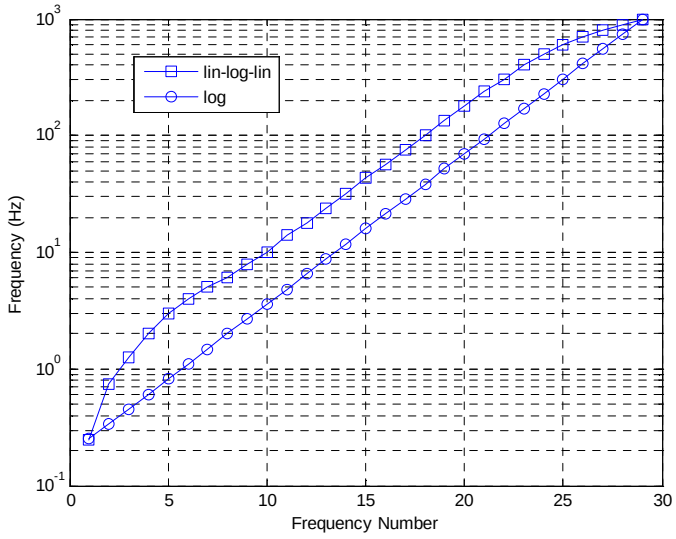

Figure 7.4. Exciting frequencies in the OBIS signal.

7.3.2 Magnitude Distribution

In previous work, where a short band multisine was applied, a constant amplitude spectrum was used [4]. The advantage of the multisine signal is the ability to vary the magnitude and control signal power, therefore optimal results can never be achieved with a flat magnitude spectrum. For bio-impedance, a number of methods have been proposed to optimize the magnitude at each frequency [15], [16]. The electrochemisty and gas transport dynamics of fuel cells, however, require that a different approach be followed. A standard approach is to use the inverse of the fuel cell magnitude response as a basis for determining the magnitudes of the individual frequency components. This will provide good signal to noise ratios throughout the measured frequency band while reducing the peak to peak magnitude of the total sum of sine signals. For a single tested cell, the normalized inverse distribution is presented in Fig. 7.5. While this spectrum is an improvement over the flat distribution, the fuel cell impedance response can incur an error at the lower frequencies. This results from using a single period of the lowest excitable frequency. The resultant signal power introduced is too low to enable the fuel cell gas transport dynamics to be accurately measured in the feedback signal. To overcome this problem, a new distribution is proposed based on an inverse Gaussian or Wald power distribution. The magnitude for the spectrum can be calculated as follows:

$$a_n = a_b - \varepsilon \sqrt{\frac{\gamma}{2\pi f_n^3}} exp\left[\frac{-\gamma(f_n - \mu)^2}{2u^2 f_n}\right] \tag{7.6}$$

Where a_b is the maximum harmonic amplitude, ε is the weighting parameter, $\mu > 0$ is the mean and $\gamma > 0$ is the shape parameter. The calculated amplitude spectrum using the above relationship and a mean frequency μ = 500Hz is shown in Fig. 7.6. In the lower frequency band, the amplitudes are maximized to ensure that sufficient energy is introduced to determine the dynamic gas transport impedance. In the mid frequency band, the amplitude is reduced following (7.6) and allows for a reduced peak to peak amplitude in the final signal while maintaining acceptable SNR. At high frequencies, where the magnitude response of the fuel cell is small, the amplitude will be increased towards the maximum to increase SNR.

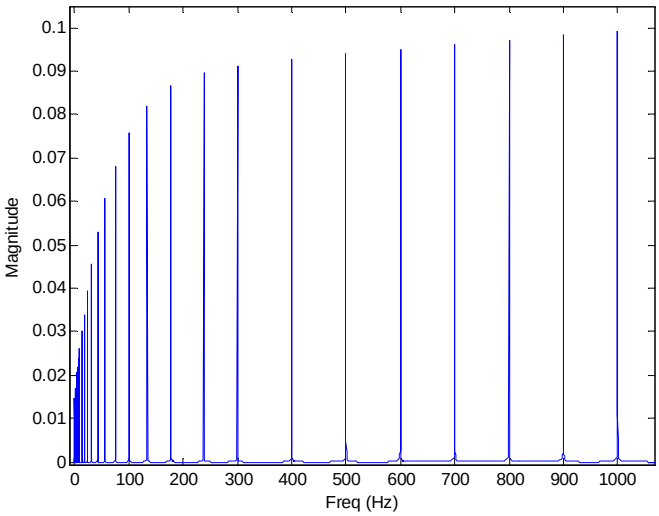

Figure 7.5. Typical inverse magnitude response spectrum.

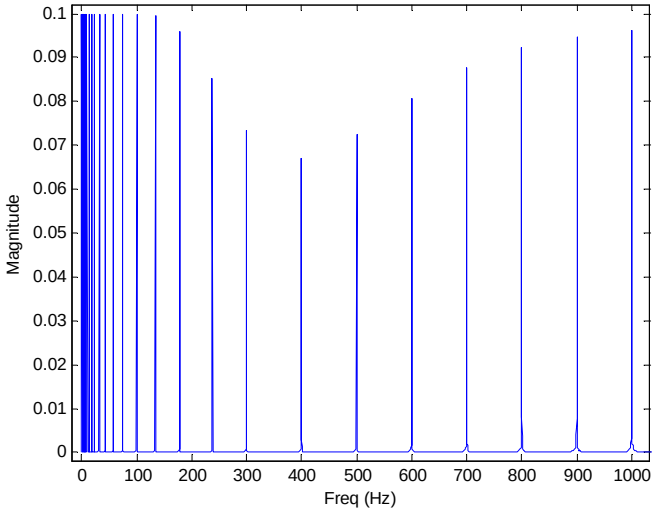

Figure 7.6. Proposed Wald magnitude spectrum.

A properly designed signal will ensure that the energy of the signal is concentrated around the maximum amplitudes. This can be evaluated by the crest factor (CF) of a signal. A large CF indicates that the signal is spread too widely between the maximum amplitudes and will result in a larger peak to peak value for a given magnitude spectrum. The variation of the crest factor for a flat magnitude and the Wald spectrum is shown in Fig. 7.7. For a small number of frequencies, there is little variation between the two distributions. At higher numbers, the difference starts to increase exponentially. The Wald spectrum enables greater energy concentration around the critical frequency bands and delivered the best results for higher harmonic numbers, as will be shown in the experimental results.

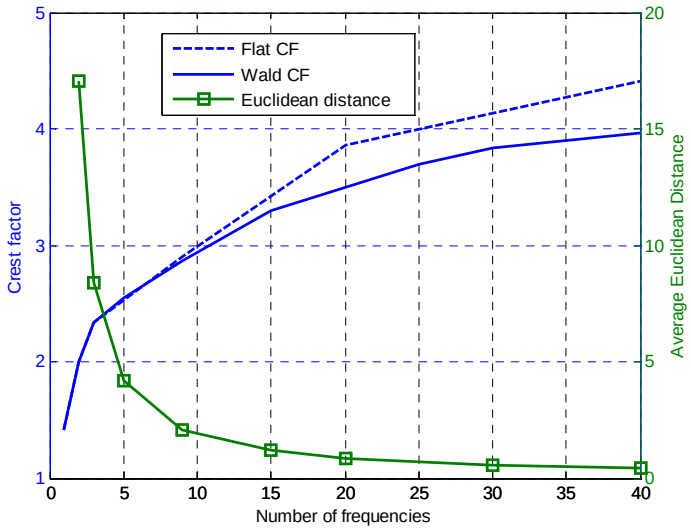

Figure 7.7. Crest factor and Impedance resolution vs. number of frequencies.

7.3.3 Selecting the Number of Frequencies

As discussed, the difference in CF between the standard flat and proposed Wald magnitude distributions will increase for increased numbers of frequencies in the final signal. The Wald distribution will, however, always produce a lower CF than the standard flat distribution but will continue to increase, as shown in Fig. 7.7. For a typical single cell, the average Euclidean distance of the impedance response versus the number of frequencies used for the lin-log-lin frequency distribution is presented along with the evolution of the CF in Fig. 7.7. This determines the dispersion of the impedance response and influences the resolution of the Nyquist plot. The greatest change occurs below a total of 20 individual frequencies in the signal. Similar trends for different cell types or stacks can be produced if *a-priori* impedance information is available. Selecting a total number of frequencies where the change in resolution of the impedance is small while CF is minimized will produce the optimal results. From the plots in Fig. 7.7, a total of 29 frequencies was selected to design the final OBIS signal and delivered acceptable performance.

7.3.4 Time Domain Optimization

By minimizing the CF, signal power is maximized thereby increasing the SNR and

reducing the peak amplitude of the signal. For the Nyquist spectrum of the impedance to be acceptable, the Kramers-Kronig relations require that the system be stable and kept within a linear operating region for the duration of the measurement. By reducing the CF of the signal, the fuel cell will be subjected to a smaller disturbance thereby remaining close to the linear region of operation. For the designed multisine, the CF can be calculated as follows [16]:

$$CF = \frac{\sqrt{2}max|u(t)|}{\sqrt{\sum_{n=0}^{N-1} a_n^2}}, \quad t \in [0, T] \tag{7.7}$$

By using the CF as the minimization function and the phase vector as the controlled parameters, the signal can be optimized using any non-linear optimization algorithm. The continuous time signal with a linear-logarithmic-linear frequency and Wald magnitude spectrum is presented in Fig. 7.8a for a random phase vector. This signal has a CF of 3.812 indicating poor energy concentration around the maximum amplitude. The peak to peak amplitude of the signal is 2.662. Time domain optimization was then performed in MATLAB using the optimization toolbox in order to minimize the CF and the peak to peak magnitude of the signal by using the phase vector. The continuous time signal using the optimized phase vector obtained from the optimization procedure is presented in Fig. 7.8b. The new CF is 2.8 and the peak to peak amplitude is 2.03. The improvements in these values lead to a greater concentration of energy at the peak magnitudes of the signal. This will lead to a smaller disturbance when it is introduced into the fuel cell as a current perturbation. It is also possible to proportionally increase the magnitudes of the harmonic spectrum while keeping the system within an acceptable range to ensure that non-linearity is kept to a minimum in the system response.

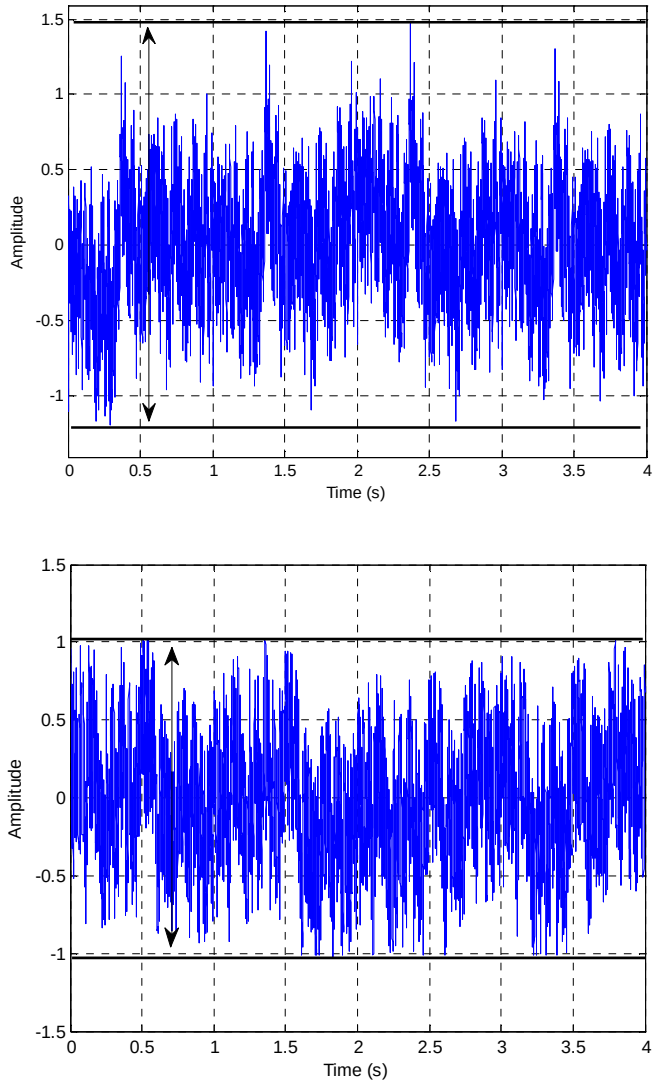

Figure 7.8(a). Un-optimized signal and (b) optimized signal in the time domain.

EIS on a fuel cell can be performed by introducing a stimulating waveform onto the DC current. The measured voltage response is then captured and the impedance calculated. To ensure that the system stays within an acceptable region that can be assumed as linear, the voltage response must be maintained within a predetermined value. This voltage value, known as the thermal voltage can be calculated as follows [4]:

$$V_T = \frac{RT}{F} \tag{7.8}$$

Where R is the gas constant, T the cell temperature and F is Faradays constant. For a cell temperature of 70°C this equates to 30mV. If the response magnitude is kept below this

value, it can be assumed that no additional harmonics at the excited frequencies will be introduced that may influence the measurements.

7.4 Hardware Implementation

In order to realize the OBIS technique on a functioning fuel cell, a low cost hardware platform was developed. The system was designed to operate at very low voltages, below 1V, in order to test not only single cells but also fuel cell stacks compared to other systems where only stack level voltages could be accommodated [6]. The signal processing and control was done on the embedded DSP of a DSpace DS1104 system that allowed for rapid prototyping and performance verification.

7.4.1 Control and Hardware Description

A schematic diagram of the implemented DSpace system and the connections to the input and output channels are shown in Fig. 7.9. Data acquisition was performed using the 16bit digital to analogue converters with a sampling frequency of 20kHz. Generating the broadband signal was accomplished using the predesigned signal vectors that are stored in the onboard memory of the system, as shown in Fig. 7.10. The multisine is computed after which it was scaled by a gain in order to generate the proper reference for the amplifier hardware. A DC offset is added to ensure that the signal does not zero.

The voltage and current feedback from the fuel cell, with impedance $Z(\omega)$, was measured using respective non-intrusive transducer circuits.

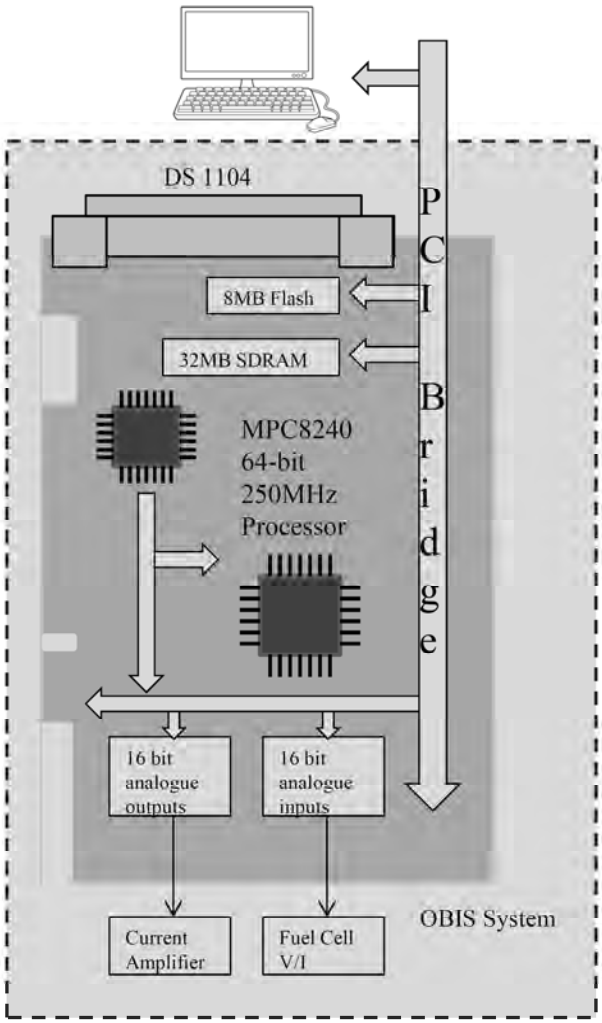

Figure 7.9. Schematic diagram of DSpace control and signal processing hardware.

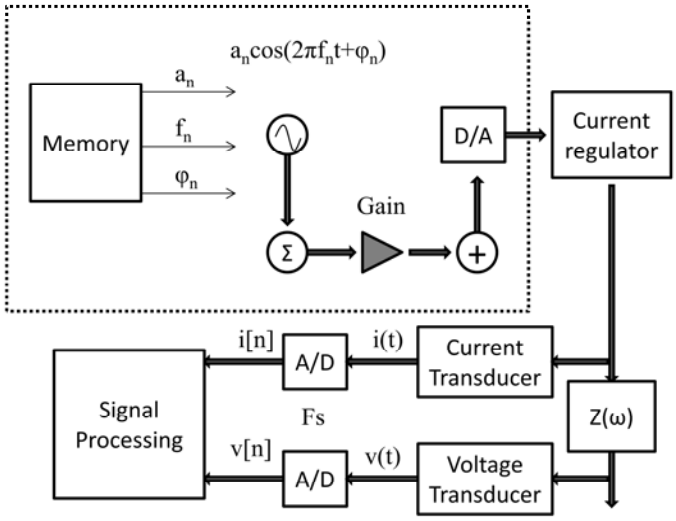

Figure 7.10. Schematic diagram of OBIS system implementation.

After the signals were digitized, the discrete signals were recorded for processing. A schematic diagram of the current regulator circuit used to superimpose the OBIS signal onto the DC current of the fuel cell is presented in Fig. 7.11. A high bandwidth low voltage audio amplifier was used to generate the gate drive signal to the semiconductor SW1. In order to realize low voltage high frequency operation, a high performance MOSFET was used with a total on resistance of 1.2mΩ. The analogue output of the audio amplifier drives the MOSFET through a gating resistor R1 in the active region. The minimum drain to source voltage allowed to ensure proper operation was 0.1V and the maximum 24V. This allowed the single semiconductor to operate on single cells and small stacks. With proper cooling, the current regulator is able to act as an electronic load and allows for a wide range of tests to be performed. The small resolution required by the gate drive of the MOSFET to accurately realize the OBIS signal was accomplished by properly matching the gain of the audio amplifier to the MOSFET gate charge and the resistor R1. Fine adjustments were made in the control system by varying the gain in the software as shown in Fig. 7.10. Despite some non-linearities, the system performed with acceptable error, as will be shown in the following sections.

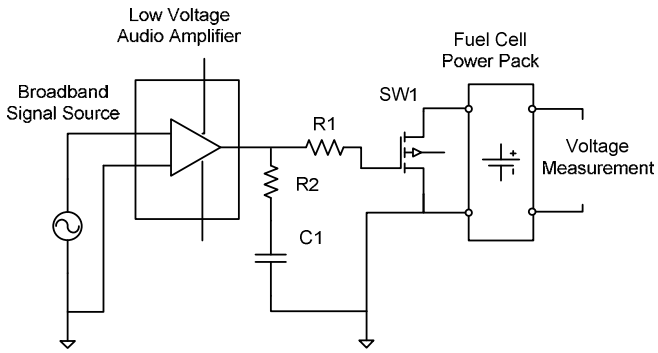

Figure 7.11. Signal generation hardware and connections to fuel cell.

7.4.2 Calibration

The initial calibration of the hardware was done on a simple Randles equivalent circuit, as shown in Fig. 7.12. The component values for the test circuit are presented in Table 7.1. The system was tested using the standard EIS procedure and an un-optimized multisine signal for a frequency range of 1Hz to 1kHz. The multisine signal comprised a flat

magnitude spectrum and a log odd frequency distribution. The total signal length was limited by the lower frequency limit to 1s. The impedance results for both tests along with the theoretical Nyquist plot are presented in Fig. 7.13. It is clear that both the EIS and broadband signals produce acceptable results with minimal error. The distinct advantage of the broadband signal is the measurement time of 1s compared to EIS time of about 2 minutes. The signal was not optimized for the circuit and demonstrates the loss of resolution.

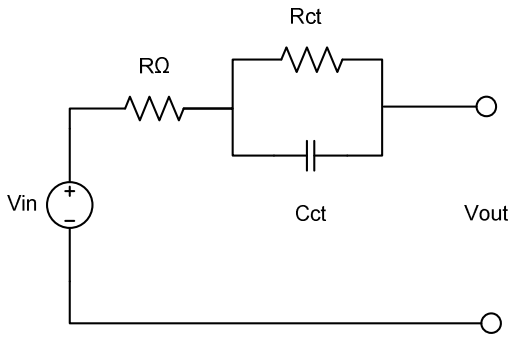

Figure 7.12. Randles equivalent test circuit.

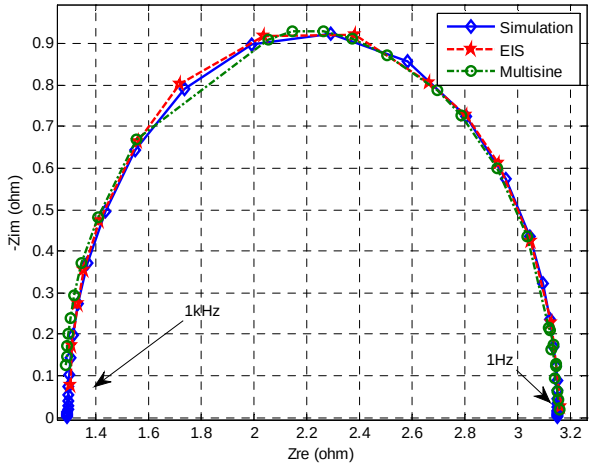

Figure 7.13. Comparison of experimental and simulated Nyquist plots.

TABLE 7.1
TEST CIRCUIT PARAMETERS

Circuit Parameter	*Symbol*	*Value*
Input Voltage	Vin	5V
Charge Transfer Resistance	Rct	1.85Ω
Double Layer Capacitance	Cct	1mF
Ohmic Resistance	RΩ	1.3Ω

7.5 Fuel Cell Experimental Test Procedure

7.5.1 Test Setup

The system was tested on a commercial FuelCon test station with a Baltic fuel cell test assembly. The experimental test setup used in this work is presented in Fig. 7.14. The assembly housed the MEA, graphite bipolar plates and current collectors. The total surface area of the MEA was 25cm^2 and comprised of a Nafion XL membrane with carbon supported Platinum catalyst. The gas diffusion layers used were Sigracet type 25 BC and compressed onto the MEA during assembly.

Unless otherwise stated, the cell was fed with air on the cathode side and research grade hydrogen on the anode side at 1 atm. Run-in was conducted using voltage cycling between 0.8V and 0.3V for a total of 12 cycles each lasting one hour. The stoichiometry of the anode and cathode were 1.5 and 2 respectively. The membrane was humidified using the inline humidification system with an initial relative humidity of 100%. To avoid unwanted flooding, the gas transfer lines were heated to 120°C while the cell temperature was varied between 60°C and 80°C. During initial testing, the flows of the anode and cathode were kept at 0.45SLPM and 1SLPM respectively to avoid interference that may be caused by the mass flow controllers during transients.

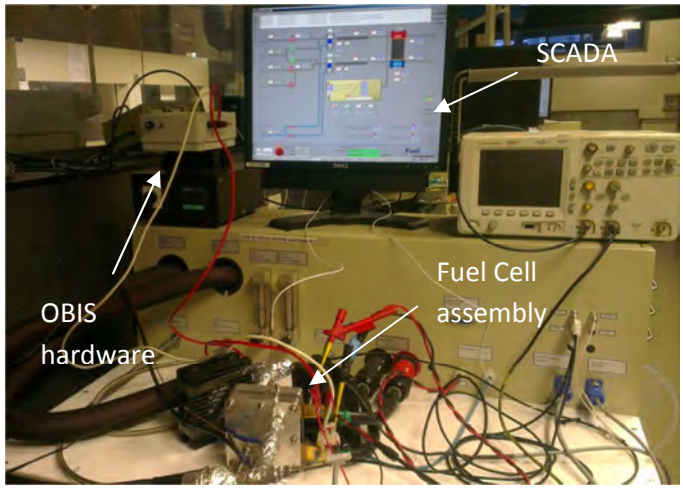

Figure 7.14. Experimental Fuel Cell test bench

7.5.2 Flooding and Drying Procedures

To validate system performance during fault conditions, the cell was subjected to flooding and drying. The drying was performed by running the fuel cell at a low current density for a predetermined period of time to minimize water production in the cathode. The humidification was lowered by dropping the temperature of the humidifiers below that of the fuel cell. By varying the humidifier temperatures, the relative humidity (RH) of the gas streams can be controlled. Flooding can be enforced by increasing the humidifier temperatures to above that of the cell thereby running at a RH of above 100%. At high current densities where the cell will produce significant amounts of water, flooding of the GDL and catalyst layer will occur. Liquid water formation in the flow fields will contribute to the drop in performance as well as performance instability as gas transport to the catalyst is blocked.

7.5.3 Measurement Procedures

The performance of the fuel cell was analyzed by measuring polarization curves and EIS data at healthy and faulted conditions. The polarization curves were conducted by varying the load current between 0 and 1A/cm^2 with a lower voltage limit of 0.3V. The cell was allowed to stabilize for 10 minutes at each measurement interval before the data point was captured. In the activation region, the current was stepped in 0.05A/cm^2 increments to produce better accuracy. In the ohmic region, the step size was increased to 0.1A/cm^2. Where possible, EIS was conducted using the commercial FRA that forms part of the FuelCon test stations. The system lower and upper frequency limits were set to 0.1Hz and 10kHz respectively. The amplitude, number of cycles and repeat measurements were set to the manufacturer standard for the impedance measurement range of a single cell.

7.6 Experimental Results and Discussion

The operation and performance of a PEM fuel cell is strongly influenced by the water content. The ionic conductivity of the membrane is dependent on the both the humidification and the internal water generation and requires proper management of the

humidifiers and the gas flow rates. When the cell is operated under low RH and current densities, insufficient levels of water will be present to enable proper membrane conductivity, resulting in an increase in ohmic resistances. By monitoring this high frequency resistance, it is possible to diagnose the drying condition, which can be done by evaluating the ripple voltage and current generated by the power electronic converters connected to the fuel cell terminals [20]. Under high RH and current densities, there will be too much water present and will cause flooding of the GDL and the catalyst layers. This will cause restriction of the catalyst and the diffusion pathways required by the gasses to facilitate the electrochemical reaction. Oversaturation of water will cause liquid water formation in the flow fields that can block reactant delivery to large portions of the cell active surface area. This can lead to permanent damage of the MEA materials and cause system instability [21], [22].

For proper fault classification, monitoring the impedance for a small number of frequencies, by using converter ripple, becomes insufficient as flooding and fuel starvation have similar features. A proper full spectrum Nyquist plot is thus required for online condition monitoring and can be produced by the OBIS system.

7.6.1 Drying Results

The humidifier temperatures were reduced, after which the cell was allowed to reach stable conditions before testing commenced. The polarization curves for fully humidified conditions and increased levels of drying are presented in Fig. 7.15. The loss of membrane conductivity on performance is evident and mainly increases the ohmic losses in the cell. The experimental Nyquist plots for the three conditions are presented in Fig. 7.16. The current density of the cell was set to 400mA/cm^2 corresponding to the centre of the polarization curves or the linear ohmic region. The results for the commercial FRA utilizing standard EIS are plotted overlapping the results captured by the OBIS system. The FRA required about 5 min to complete each measurement cycle compared to the 4 second OBIS measurement. The results indicate very good agreement between the two methods while the OBIS produced superior resolution. Small differences between the two techniques in the ohmic resistance or high frequency intercept can be observed. During testing, the EIS was performed and the OBIS performed thereafter. The time lapse between

the tests caused minor variations in the membrane water content as water is continuously generated by the reaction and is the most probable cause of the differences observed.

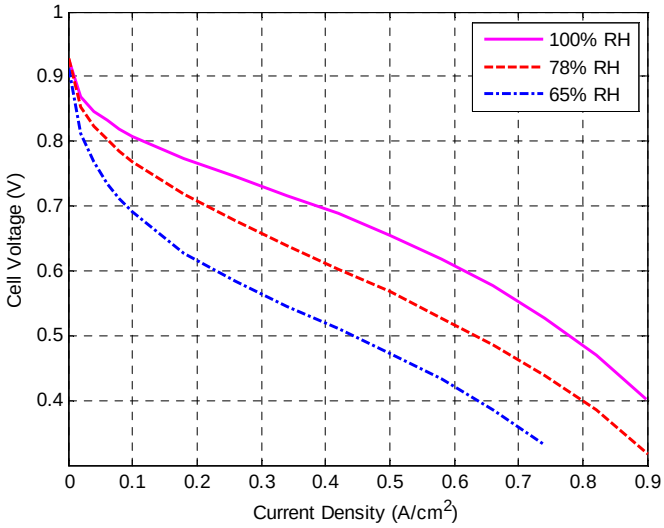

Figure 7.15. Experimental polarization curves for drying mechanism.

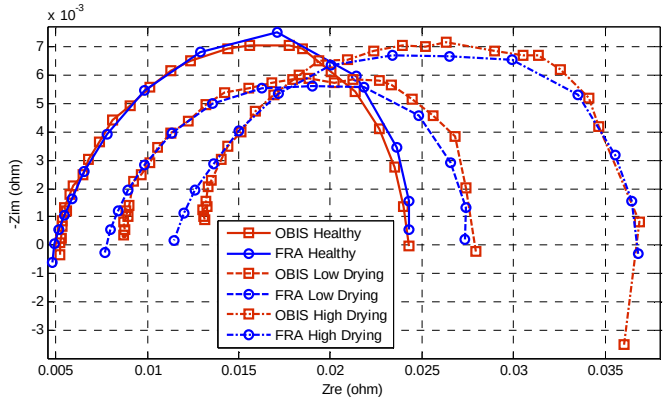

Figure 7.16. Experimental Nyquist plots for drying mechanism.

The magnitude spectrum of the OBIS voltage signal is presented in Fig. 7.17. The low frequency region produced the largest magnitudes due to the impedance magnitude and the employed Wald distribution of the applied current signal. Lowering the low frequency band magnitude resulted in measurement errors as the energy introduced into the fuel cell was not sufficient to drive the gas transport mechanism for the small signal analysis.

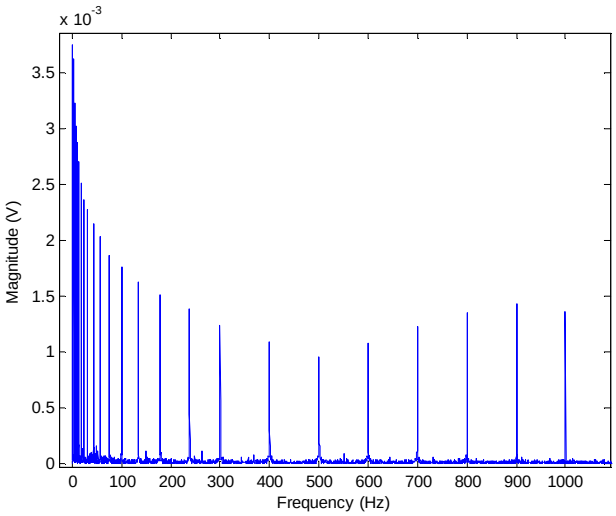

Figure 7.17. Experimental magnitude spectrum of voltage response for OBIS.

7.6.2 Flooding Results

Flooding in the fuel cell was enforced by increasing the RH to well above 100%. The resulting drop in performance is clear from the polarization curves in Fig. 7.18. Higher degrees of flooding resulted in unstable measurements and could not produce valid EIS measurements. Unlike the drying results, where the activation losses were also increased, flooding will produce increased losses as the current density is increased and more water is produced. The liquid water can block diffusion pathways to the active catalyst sites. The experimental Nyquist plots are presented in Fig. 7.19 for the commercial FRA and OBIS for different current densities. Accounting for the small variation in measurements caused by water generation taking place between the FRA EIS and OBIS, the results are in very good agreement. It should be noted that small changes in the impedance take place during the time required to perform the EIS. This effect is increased under fault conditions such as flooding of drying. By employing a system such as the proposed OBIS, where the impedance data can be acquired within a very short period of time, these variations can be minimized. The measured data produced is thus enhanced in terms of the Kramers-Kronig relations for stability and linearity in the fuel cell system.

To demonstrate the ability of the system to perform under extreme non-linear conditions, the fuel cell was run until droplet formation in the flow fields was severely accelerated. For this condition, polarization curves and EIS could not be recorded as the

system was unable to reach steady state for a long enough period of time to acquire viable data. The current density was increased to 720mA/cm2 to enforce internal water production while the gas transfer line temperature was lowered to 60°C to enforce condensation. The voltage profile during this test and the OBIS signal injection is presented in Fig. 7.20. The non-linear behaviour of the flooding is evident and indicated in the profile. As the liquid water blocks a portion of either the gas channels or the GDL, the voltage will drop dramatically. Due to pressure build-up, the water droplet will eventually be forced out thereby freeing the channel to transport gas to the reaction layer. This will result in a slower rise towards the initial steady state voltage.

The OBIS signal is introduced at the 10s mark where the cell voltage was close to the initial steady state value. The time duration of the measurement was 4 seconds and is indicated in the voltage profile. It is clear that long measurement times to acquire the EIS data will not result in usable data as the intervals between the flooding non-linearities will cause inconsistencies in the measurements. In general, the measurement time of the impedance response should be made as short as possible. This is dependent on the lower frequency limit of interest. In this work, this was not lowered below 0.25Hz. The resulting Nyquist plot is presented in Fig. 7.21. The drastic increase in the diameter is evident. The resolution of the arc in the low frequency region is reduced due to the influence of the flooding mechanism on the gas transport kinetics. The ability to generate the Nyquist diagrams under these types of extreme conditions gives unique insight into the impedance response of the fuel cell and can be related to the electrochemistry using applicable modelling methods [10].

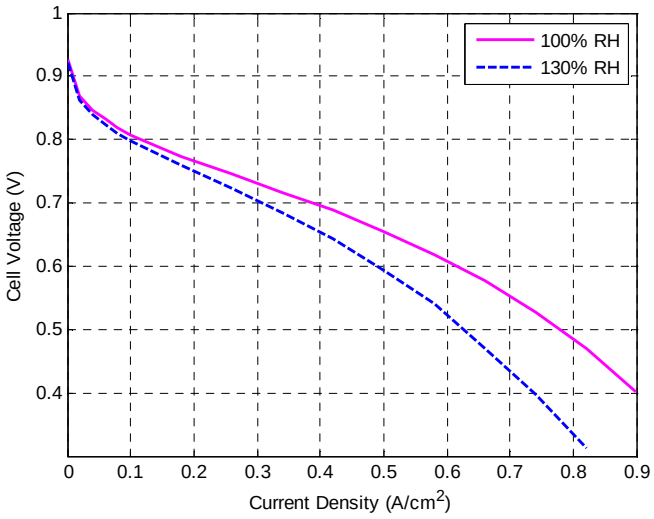

Figure 7.18. Experimental polarization curves for flooding.

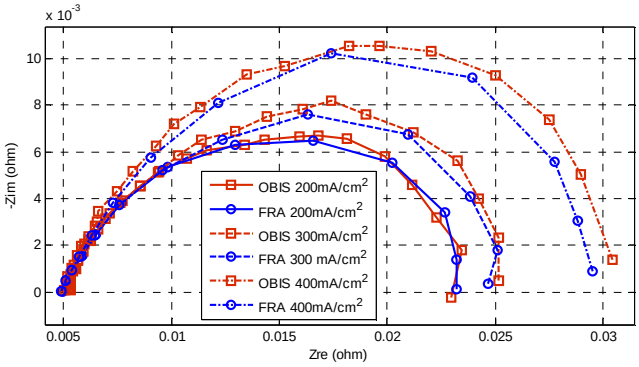

Figure 7.19. Experimental Nyquist plots for flooding.

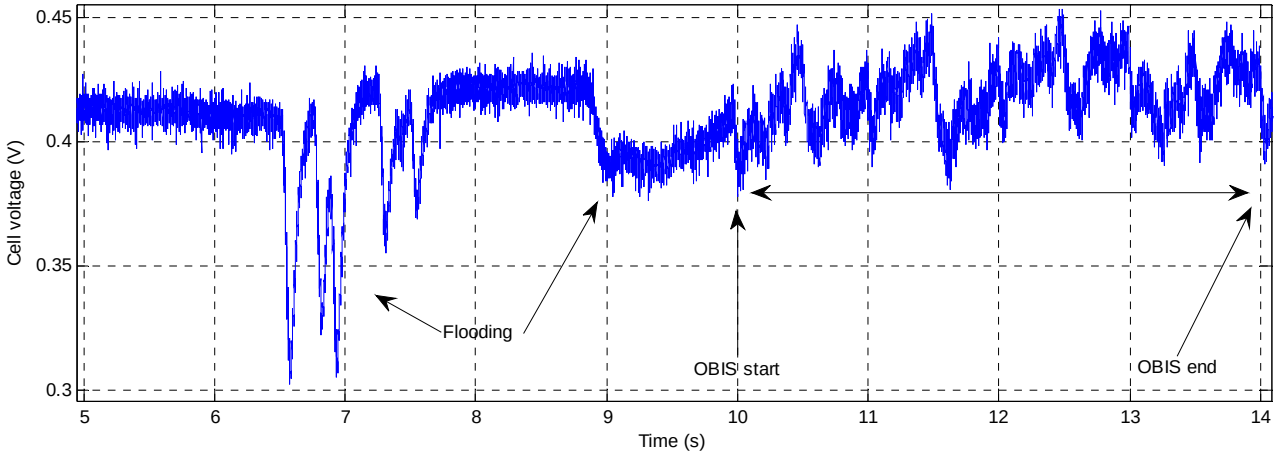

Figure 7.20. Voltage profile during extreme flooding and OBIS signal injection.

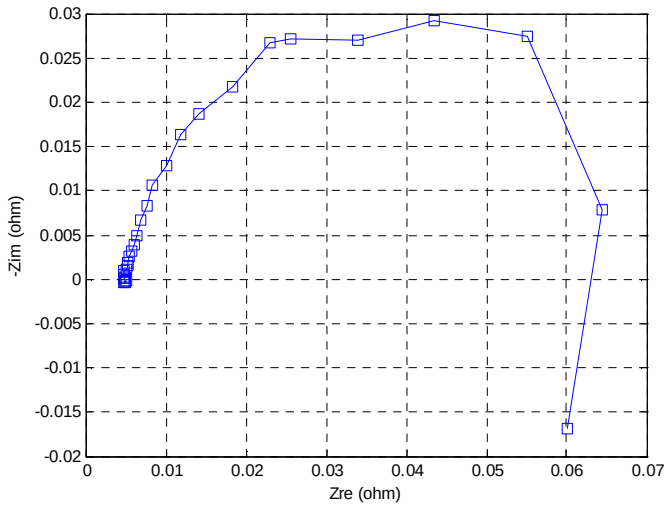

Figure 7.21. Generated Nyquist plot during extreme flooding using OBIS.

7.6.3 Oxygen Starvation Results

In an operational fuel cell, the oxygen is typically supplied through air via a compressor. Failure in the flow control or the compressor subsystems can cause a drop in reactant flow leading to performance loss. Long term operation under oxygen starvation can lead to permanent degradation of the membrane and effective catalyst surface area [23]. Since the reaction rate of oxygen at the cathode occurs at a much slower rate than the hydrogen reaction, transient load conditions must be actively monitored and the air flow properly controlled. The development of systems and models that can estimate the oxygen excess ratio allows the system to compensate for load changes and delays in the flow control at a much faster rate [24], [25]. These methods, however, either require complex hardware or algorithms to execute. Rapid impedance data acquisition provides a method to overcome these limitations by monitoring the gas transport resistances.

To simulate the oxygen starvation phenomenon, the flow rate of the cathode gas stream was sequentially reduced until a characteristic change in the polarization curves could be observed. Reducing the flow rate causes increased mass transport losses in the cell, as shown in Fig. 7.22. A secondary change in gradient in the mass transport region can be related to a change in the Tafel slope, indicating that starvation has commenced [26]. This can be observed in Fig. 7.22 for the polarization curve recorded at the lowest cathode flow rate of 0.4SLPM. The impedance of the fuel cell was recorded using the commercial FRA

and the OBIS system and presented in Fig. 7.23. It should be noted that under these conditions the cell starts becoming unstable to variations and load. The FRA failed to measure data at certain frequency set-points and caused a reduction in the Nyquist plot resolution and variance. The OBIS system produced better results with the reduction in measurement time and the designed magnitude and frequency distributions. The increase in diameter is clearly visible for both data sets when compared to the healthy condition.

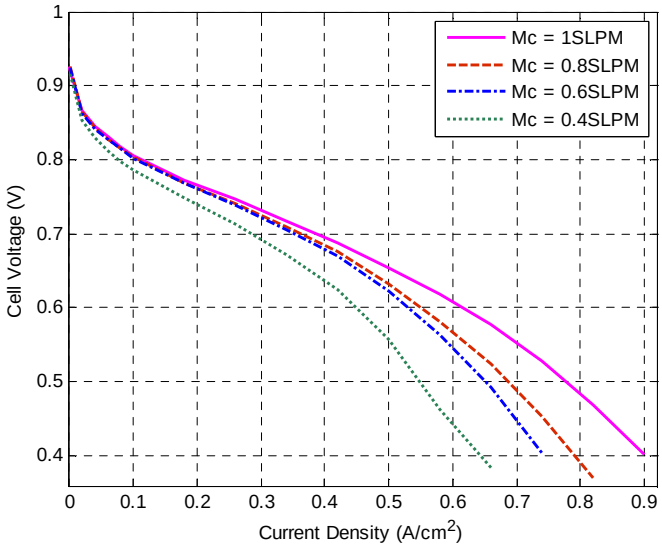

Figure 7.22. Experimental polarization curves for Oxygen starvation.

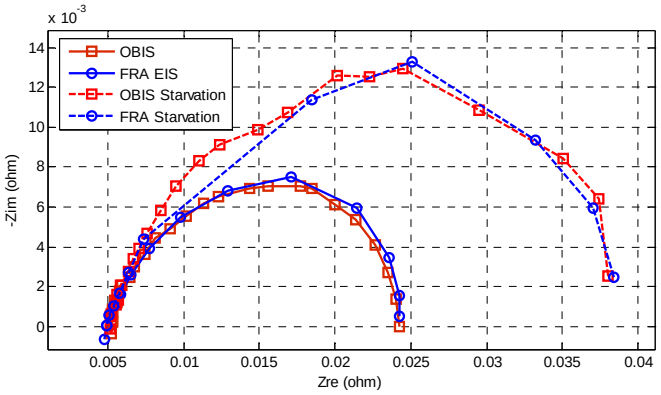

Figure 7.23. Experimental Nyquist plots for Oxygen starvation.

To compare the variation in the Nyquist plots for all the possible faults investigated in this work, an impedance signature map is presented in Fig. 7.24. The drying fault is clearly identifiable as the ohmic resistance is increased and the Nyquist plot shifts away from the origin to the right. Extreme values of flooding will result in the drastic changes in the

diameter while lower flooding levels are more difficult to distinguish from faults such as starvation.

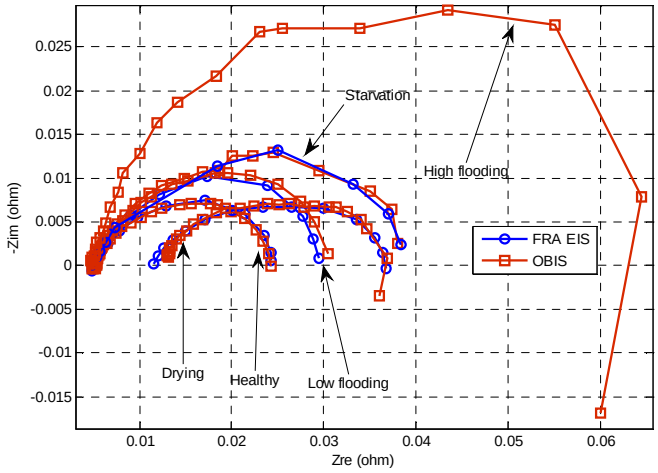

Figure 7.24. Impedance signature map of fault mechanisms.

Conclusion

This chapter presents the development of an online condition monitoring system using Optimized Broadband Impedance Spectroscopy. The design and optimization procedure for the signal in the time and frequency domain is performed by proper selection of the frequency and magnitude distributions. It is shown how the crest factor of the signal can be reduced by optimizing the phase vector of the signal allowing for increased SNR. The development of a low cost hardware platform that can perform OBIS on single cells and stacks is presented. In particular, the system is designed to accommodate voltages below one volt and measure at milliohm scale resolutions required for single cell diagnostics. The system is tested under a range of healthy and possible fault scenarios and compared with the results generated by a commercial FRA utilizing standard EIS. From the results, the system is proven to produce measurements under extreme conditions where normal EIS fails. The results from the proposed OBIS technique compares well with that of the commercial system with good accuracy and resolution while also allowing for rapid condition monitoring.

References

[1] J. Wu, X. Z. Yuan, H. Wang, M. Blanco, J. J. Martin, and J. Zhang, "Diagnostic tools in PEM fuel cell research: Part I Electrochemical techniques," *International Journal of Hydrogen Energy*, vol. 33, no. 6, pp. 1735–1746, 2008.

[2] Barbir F. PEM fuel cells: theory and practice. New York: Elsevier/Academic Press; 2005.

[3] Page, S.C.; Anbuky, A.H.; Krumdieck, S.P.; Brouwer, J., "Test Method and Equivalent Circuit Modeling of a PEM Fuel Cell in a Passive State," *Energy Conversion, IEEE Transactions on* , vol.22, no.3, pp.764-773, Sept. 2007

[4] Dotelli, G.; Ferrero, R.; Stampino, P.G.; Latorrata, S., "Analysis and Compensation of PEM Fuel Cell Instabilities in Low-Frequency EIS Measurements," *Instrumentation and Measurement, IEEE Transactions on,* IEEE Xplore early access.

[5] Carmelo Brunetto, Antonino Moschetto, Giuseppe Tina, "PEM fuel cell testing by electrochemical impedance spectroscopy*", Electric Power Systems Research*, Vol. 79, Issue 1, pp. 17-26, January 2009.

[6] Ordonez, M.; Sonnaillon, M.O.; Quaicoe, J.E.; Iqbal, M.T., "An Embedded Frequency Response Analyzer for Fuel Cell Monitoring and Characterization," *Industrial Electronics, IEEE Transactions on* , vol.57, no.6, pp.1925-1934, June 2010.

[7] Dhirde, A.M.; Dale, N.V.; Salehfar, H.; Mann, M.D.; Han, T.H., "Equivalent Electric Circuit Modeling and Performance Analysis of a PEM Fuel Cell Stack Using Impedance Spectroscopy*," Energy Conversion, IEEE Transactions on* , vol.25, no.3, pp.778,786, Sept. 2010.

[8] Andrej Debenjak, Pavle Boškoski, Bojan Musizza, Janko Petrovčič, Đani Juričić, "Fast measurement of proton exchange membrane fuel cell impedance based on pseudo-random binary sequence perturbation signals and continuous wavelet transform", *Journal of Power Sources*, Vol. 254, pp. 112-118, 15 May 2014.

[9] Al Nazer, R.; Cattin, V.; Granjon, P.; Montaru, M.; Ranieri, M., "Broadband Identification of Battery Electrical Impedance for HEVs," *Vehicular Technology, IEEE Transactions on* , vol.62, no.7, pp. 2896-2905, Sept. 2013.

[10] S. Tant, S. Rosini, P.-X. Thivel, F. Druart, A. Rakotondrainibe, T. Geneston, Y. Bultel, "An algorithm for diagnosis of proton exchange membrane fuel cells by electrochemical impedance spectroscopy", *Electrochimica Acta*, Available online 30 April 2014, ISSN 0013-4686, http://dx.doi.org/10.1016/j.electacta.2014.04.108.

[11] Michael A. Danzer, Eberhard P. Hofer, "Electrochemical parameter identification—An efficient method for fuel cell impedance characterisation", *Journal of Power Sources*, Vol. 183, Issue 1, pp. 55-61, 15 August 2008.

[12] Nahvi, M.; Hoyle, B.S., "Electrical Impedance Spectroscopy Sensing for Industrial Processes," *Sensors Journal, IEEE* , vol.9, no.12, pp.1808-1816, Dec. 2009.

[13] M.A. Rubio, A. Urquia, R. Kuhn, S. Dormido, "Electrochemical parameter estimation in operating proton exchange membrane fuel cells", *Journal of Power Sources*, Vol. 183, Issue 1, pp. 118-125, 15 August 2008.

[14] Lindahl, P.A.; Cornachione, M.A.; Shaw, S.R., "A Time-Domain Least Squares Approach to Electrochemical Impedance Spectroscopy," *Instrumentation and Measurement, IEEE Transactions on* , vol.61, no.12, pp.3303-3311, Dec. 2012.

[15] B Sanchez, G Vandersteen, R Bragos and J Schoukens, "Optimal multisine excitation design for broadband electrical impedance spectroscopy*", Meas. Sci. Technol*, Vol. 22, 115601 (11pp), 2011.

[16] B Sanchez, G Vandersteen, R Bragos and J Schoukens, Basics of broadband impedance spectroscopy measurements using periodic excitations, *Meas. Sci. Technol.* Vol. 23, 105501, 2012.

[17] Hui Li et al., "A review of water flooding issues in the proton exchange membrane fuel cell", *Journal of Power Sources*, Vol. 178, Jan 2008.

[18] N. Yousfi-Steiner et al., "A review on PEM voltage degradation associated with water management: Impacts, influent factors and characterization", *Journal of Power Sources,* Vol. 183, April 2008.

[19] Mirna Urquidi-Macdonald, Silvia Real And Digby D. Macdonald, “Applications Of Kramers-Kronig Transforms in the Analysis Of Electrochemical Impedance Data-III. Stability and Linearity”, *Electrochimica Acta*, Vol. 35, No. 10, pp. 1559-1566, 1990.

[20] M. Hinaje, I. Sadli, J.-P. Martin, P. Thounthong, S. Raël, B. Davat, “Online humidification diagnosis of a PEMFC using a static DC–DC converter”, *International Journal of Hydrogen Energy*, Vol. 34, Issue 6, pp. 2718-2723, March 2009.

[21] Denise A. McKay, Jason B. Siegel, William Ott, Anna G. Stefanopoulou,” Parameterization and prediction of temporal fuel cell voltage behavior during flooding and drying conditions”, *Journal of Power Sources*, Vol. 178, Issue 1, pp. 207-222, 15 March 2008.

[22] Loo, K. H.; Wong, K. H.; Lai, Y.M.; Tan, S.C.; Tse, C.K., "Derivation of a Fast Mathematical Model of PEM Fuel Cell With Two-Phase Water Transport," *Energy Conversion, IEEE Transactions on* , vol.26, no.1, pp.216-226, March 2011.

[23] Mathias Gerard, Jean-Philippe Poirot-Crouvezier, Daniel Hissel, Marie-Cécile Pera, “Oxygen starvation analysis during air feeding faults in PEMFC”, *International Journal of Hydrogen Energy*, Volume 35, Issue 22, pp. 12295-1230, 7 November 2010.

[24] Marignetti, F.; Minutillo, M.; Perna, A.; Jannelli, E., "Assessment of Fuel Cell Performance Under Different Air Stoichiometries and Fuel Composition," *Industrial Electronics, IEEE Transactions on* , vol.58, no.6, pp.2420-2426, June 2011.

[25] Restrepo, C.; Konjedic, T.; Guarnizo, C.; Avino-Salvado, O.; Calvente, J.; Romero, A.; Giral, R., "Simplified Mathematical Model for Calculating the Oxygen Excess Ratio of a PEM Fuel Cell System in Real-Time Applications," *Industrial Electronics, IEEE Transactions on* , vol.61, no.6, pp.2816-2825, June 2014.

[26] Nada Zamel, Richard Hanke-Rauschenbach, Sebastian Kirsch, Arjun Bhattarai, Dietmar Gerteisen, “Relating the N-shaped polarization curve of a PEM fuel cell to local oxygen starvation and hydrogen evolution*”, International Journal of Hydrogen Energy*, Vol. 38, Issue 35, pp. 15318-15327, 22 November 2013.

Chapter 8

Conclusion and Final Remarks

8.1 Overview of the Thesis

The findings from this thesis provide valuable insight into the condition monitoring of fuel cell systems. The contributions made are numerous and disseminated in each chapter of the thesis. Specific attention was given to online system development by improving core aspects in the identified methodologies. This was achieved by conducting detailed analysis on the key fault mechanisms that can occur in operational systems and developing methods that can perform identification and classification. To assist with evaluation, various models were developed that can be implemented in real time emulators and diagnostic systems. The models were tailored to accommodate healthy and faulted conditions while minimizing complexity and prediction error. Further developments were made in the area of rapid diagnostic systems by focusing on natural and synthetic load profiles. Implementation of advanced signal processing techniques, genetic algorithms and reduced order models facilitated accurate fault parameter estimation. It is shown that proper broadband signal design can significantly improve measurement time when compared to classic EIS systems leading to real time parameter tracking and fault prognosis in operational fuel cells.

8.2 Conclusions

Based on the results and analyses presented, the following conclusions are drawn:

In chapter 2 the current trends in fuel cell diagnostics, prognostics and investigation of degradation mechanisms are identified. The global condition monitoring strategy is presented along with a step-wise approach towards implementation. In each stage, the available methods are presented and the applications and limitations are identified. The physical structure of PEM fuel cells along with the causes and effects of component degradation are investigated. HT-PEM fuel cells are introduced and the operational advantages discussed. For data acquisition, the primary electrochemical methods used to quantify performance loss and identify degradation are presented. These include polarization curve analysis, EIS, current interrupt, cyclic voltammetry and others. For each method, the principle and operational requirements are discussed while identifying the limitations of each. It is shown that measurement time and the ability to perform measurements while the system is operational are critical paths for further development.

Fault marker identification and classification can be performed using model and non-model based techniques. In each category, the most prevalent methods used in fuel cell based technologies are discussed. In particular, semi-empirical models and reduced order circuit models were shown to be most promising by providing alternatives to highly complex analytical or statistical methods. Complex electrochemical relationships are replaced by either empirical formulations, determined from experimental analysis, or by equivalent circuit elements.

Chapter 3 presents the evaluation of HT-PEM fuel cell degradation mechanisms for the purpose of fault classification. Two experimental setups were developed to conduct the degradation and fault studies. The experimental setups used for the investigation are described along with the testing procedures. The performance variation is studied using polarization curve analysis and EIS for variation in normal operating conditions. Changes to cell temperature and reactant concentration are shown to generate specific characteristics in the experimental data. The principal fault and degradation mechanisms that can occur in HT-PEM fuel cells were separately introduced into the system. A new

method that can accelerate the acid leaching phenomenon was proposed and the results presented. The changes to the internal structure of the MEA is discussed and related to the variations of the proposed equivalent circuit model. The other fault mechanisms introduced include reactant starvation, catalyst degradation and CO poisoning. Changes to the equivalent circuit are introduced as additional circuit elements and it was found that these are unique and distinct. From the findings, a fault classification matrix is proposed that enables the use of the identified EEC parameter variations to perform fault differentiation.

A semi-empirical model that incorporates the main fault mechanisms in HT-PEM fuel cells is proposed in chapter 4. The model is tailored to accommodate the steady state and transient characteristics associated with temperature, load and flow variations. A lumped parameter approach is followed to model the reversible open circuit voltage and the loss mechanisms. These include the activation, influenced by the active catalytic surface area, ohmic and concentration losses. The electrochemical parameters associated with the possible degradation mechanisms are identified. It is shown how the catalyst surface area in the exchange current density formulation is influenced by time based degradation, load ripple and CO poisoning using empirical formulations based on experimental data. The loss of phosphoric acid, leading to increased membrane resistance is included in the model development. Other resistances influenced by the acid migration are modelled accordingly in order to accurately capture the total cell resistance.

It is shown how the model can be related to a dynamic equivalent circuit model that can be implemented in real time. This was proven by developing a new low cost single cell emulator that successfully reproduced the voltage and current profiles for the different fault scenarios. The developed model and emulator was used to estimate fuel cell performance under a variety of fault conditions leading to life time estimation and performance optimization.

A detailed investigation of CO poisoning in HT-PEM fuel cells is presented in chapter 5. The developed system is subjected to a wide range of operational variations in temperature, flow and CO concentration to evaluate the effect on system performance. This leads to the development of simple equivalent circuit models with dedicated fault elements that

provide methods for determining the extent of the poisoning condition and possible CO concentration estimation. The models are fitted to the experimental data and trends were determined for changes in the circuit parameters that can be implemented in observer based diagnostic systems. The voltage loss for a step changes in CO concentration were evaluated and the temperature dependence of CO absorption is demonstrated. To mitigate the effect of CO poisoning, active current control is proposed that enforces electro-oxidation and catalyst surface area recovery. It is shown how a natural sinusoidal current profile produces smaller overvoltages that enforce catalyst degradation, while improving power recovery when compared to existing hard switched methods.

In chapter 6 a new two stage approach for online diagnostics using small load transients is presented. The method makes use of the voltage responses obtained for small amplitude current steps that can be generated by the power conditioning hardware. Specific consideration is given to the implementation at single cell level where voltages are below 1V. Proper design of the power electronics is required to ensure that voltage collapse does not occur. From the experimental results it is shown how the transient response can evolve from overdamped to underdamped behaviour. This is used to develop the equivalent circuit model that incorporates the surface relaxation effects associated with the gas transport dynamics.

The first stage of the system calculates fault markers from the transient response for the CO poisoning condition. This was accomplished by using the S-transform for time-frequency resolution of the voltage transients. The raw data from the transform is evaluated by calculating the standard deviation of the frequency components. The maximum STD is related to the low frequency intercept that provides a first fault marker in the system. The second stage develops a system identification method by using the equivalent circuit and a population based incremental learning algorithm. The circuit parameters are calculated by the algorithm for increased levels of CO poisoning to estimate the severity of the fault condition. The results are used to generate Nyquist plots of the impedance and compared with classical EIS. The system demonstrated the ability to extract valuable markers and parameter information by using small amounts of data while minimizing system disturbance.

Chapter 7 presents the development of a novel rapid condition monitoring system using **O**ptimized **B**roadband **I**mpedance **S**pectroscopy. The system was developed to meet the needs of both single cell and stack level integration. System performance was verified on a LT-PEM fuel cell setup as the technology is widely commercialized when compared to HT-PEM fuel cell systems. The water transport internal to the fuel cell structure is discussed and the water management faults known as flooding and drying are selected as possible fault conditions. The design and optimization procedure for the broadband signal is presented and it is shown how the measurement time can be minimized. The hardware is developed to be low cost and scalable while providing good SNR and analogue reference to output signal integrity. The system is tested for healthy and faulted conditions that include flooding drying and oxygen starvation. The obtained experimental results are compared with that obtained from a commercial FRA and demonstrated acceptable accuracy, superior resolutions and a substantial decrease in measurement time. The system was tested under extreme non-linear conditions where the FRA failed to capture results demonstrating the viability for real time online diagnostics.

8.3 Recommendations and Future Work

The experimental work conducted throughout this thesis was done across a wide range of operating conditions in order to cover possible scenarios that can occur during commercial implementation. It is, however, possible to further the research by extending these ranges in future work and improve our understanding under more severe conditions. The concepts presented were verified and tested in single cells to provide a basis at a fundamental level without incorporating possible complications that can occur during stack level implementation. Some further work might be required to apply the proposed methods for integration with fuel cell stacks and demonstrate performance.

In this work, the evaluated fault mechanisms were introduced individually into the system. As discussed throughout the thesis, faults such as CO poisoning, reactant starvation and severe acid leaching can occur very quickly under certain conditions. Since it is unlikely that multiple of these fault conditions can occur simultaneously, the fault mechanism can be identified rapidly online using the methods developed in this thesis. For

substantial variations in operating conditions, such as temperature and flow, and the introduction of simultaneous faults, the resolution of the mechanisms become more complex to execute. Under these circumstances, it is suggested to employ a parallel approach by using the presented model in chapter 4 and the developed analysis protocols developed in chapters 6 and 7 and should be verified in future work.

It is known that electrochemical methods such as EIS and current interrupt can be used in other electrochemical devices, such as batteries and photovoltaic cells. It is thus recommended that the developed methods and systems presented in this thesis, pertaining to rapid online degradation and fault detection, be extended for application in the other electrochemical devices.

8.4 Closing Remarks

The condition monitoring and fault prediction of fuel cell systems have become a primary aspect as the technology gains greater commercialization. The development of these systems and associated models provide a basis for prognostics and state of health estimation that allow for system optimization and life cycle extension.

Even though current models have focused on LT-PEM fuel cells the development of newer HT-PEM fuel cell systems, which alleviate some of the operational problems, have produced new models that predict behaviour. The changes in materials and higher operating temperature resulted in altered fault aspects that can be detected and mitigated in the power electronic subsystems.

The findings in this thesis epitomize the need for new rapid online fault detection systems in fuel cells. This provided an avenue for the development of new fault classifying models, marker detection strategies and advanced signal generation and analysis methodologies for application in fuel cell condition monitoring systems.

Appendix A

Emulation of LT-PEM Fuel Cell Flooding

A.1 Modelling of Liquid Water Mass Build-up

Both the HT-PEM and the LT-PEM fuel cells are modelled using a lumped parameter semi-empirical approach in order to reduce complexity and processing hardware requirements. This allows the complete emulator system to be integrated on a single development platform.

The LT-PEM fuel cell system is modelled at stack level, with the terminal voltage calculated as in (4.33). The cell potential, E_{cell}, is calculated as in chapter 4 using (4.1) while adjusting for the temperature range of interest. The activation loss for a system using pure hydrogen is calculated using the standard Butler-Volmer relationship described in (4.7). Humidification of the membrane is now required to enable proton conduction and must be accounted for in the model. The resistance of the membrane is dependent of the water content and modelled as in (7.1). Water is transported across the membrane through electro osmotic drag and back diffusion [1], [2] as was shown in Fig. 7.1.

In the anode, the water mass is modelled as follows [3]:

$$\frac{dm_{w,an}}{dt} = W_{v,an,in} - W_{v,an,out} - W_{v,mem} - W_{l,an,out} \quad (a.1)$$

Where $m_{w,an}$ represents the water mass in the anode, $W_{v,an,in}$ the mass flow rate of water vapor entering the anode, $W_{v,an,out}$ the mass flow rate of water vapour leaving the anode, $W_{v,mem}$ the mass flow rate of water across the membrane and $W_{l,an,out}$ the mass flow rate of liquid water leaving the anode.

The mass flow rate of water vapour entering the anode is calculated as follows:

$$W_{v,an,in} = W_{an,in} - W_{H2,an,in} \quad (a.2)$$

Where $W_{an,in}$ is the total flow entering the anode. The mass flow rate of hydrogen entering the anode is calculated as follows:

$$W_{H2,an,in} = W_{an,in} \frac{1}{1 + \omega_{an,in}} \quad (a.3)$$

Where $\omega_{an,in}$ is the anode humidity ratio and is dependent on the relative humidity that is controlled by the temperature of the humidifiers.

The rate of liquid water leaving the anode is set to 0 as the anode channel is assumed to be dead ended. For model simplicity, the water flow rate across the membrane is assumed to be negligible compared to the accumulation resulting from the gas stream humidification. If the formation of liquid water in the anode is related to the restriction of the active area, the apparent fuel cell active area is approximated as follows [4]:

$$S_{app} = S_{fc} - \frac{2m_{l,an}}{\rho_l t_w} \quad (a.4)$$

Where ρ_l is the liquid water density and t_w is a tunable parameter that represents the thickness of the water layer.

The temperature rise of the fuel cell due to the internal heat generation rate is caused by the inherent exothermal chemical reaction. The main mechanisms that transfer thermal energy to and from the stack are conduction, convection and to a lesser extent, radiation. Under steady state conditions the fuel cell will operate at a constant temperature. Under transient conditions the fuel cell will either heat up or cool down depending on the operating point. The temperature rise/fall of the fuel cell can be approximated by

calculating the electrical losses using (4.32). The values of the input parameters for the model used during testing are given in table A1.

TABLE A1
LT-PEM STACK MODEL CONSTANTS

Coefficient	*Symbol*	*Value*	*Unit*
Charge double layer capacitance	C_{cdl}	0.8	F
Active area of cells	A_{fc}	100	cm^2
Thickness of water layer	t_w	0.7	µm
Thermal capacitance	C_t	0.035	J/K
Coolant temperature	$T_{coolant}$	65	°C
Limiting current density	i_{lim}	1.4	A/cm^2
Anode input flow rate	$W_{an,in}$	8	slpm (max)
Cathode input flow rate	$W_{ca,in}$	31.8	slpm (max)
Anode flow delay	τ_a	0.03	s
Cathode flow delay	τ_c	0.03	s
Hydrogen pressure	P_{H2}	1.2	atm
Air pressure	P_{air}	1.05	atm

A.2 Emulator Platform

For stack level emulation, a new topology was developed in [5] and will briefly be discussed. The developed emulator topology is presented in Fig. A.1. The hardware is divided into two stages where the first stage is known as the power stage converter and will function as a controllable power supply. The output of the power stage converter is connected to the second part of the emulator system that replicates the fast dynamic responses of the fuel cell as predicted by the model. This part of the system is referred to as the control stage converter of the emulator system.

The salient performance criteria for the control stage converter are response time for transients and output ripple cancellation. To achieve this, a multiphase interleaved buck converter was selected as the control stage topology. The phase shifting principle used by the multiphase systems introduces a ripple cancellation factor as shown in Fig. A.2 [6], [7]. Under steady state conditions the control stage converter operates at a critical duty ratio to ensure that there is a complete cancellation of output voltage ripple as shown. To ensure maximum control effort can be executed by the control system via a change in duty ratio

for both an upward and downward change in reference during transient conditions, a critical duty ratio of 50% is required. From Fig. A.2 it can be seen that both the double and four phase interleaved topologies can be used. As a four phase system requires a large amount of active devices and control hardware, the double phase system was selected. A reduced number of phases will also reduce the effect of phase unbalance that can occur in the system.

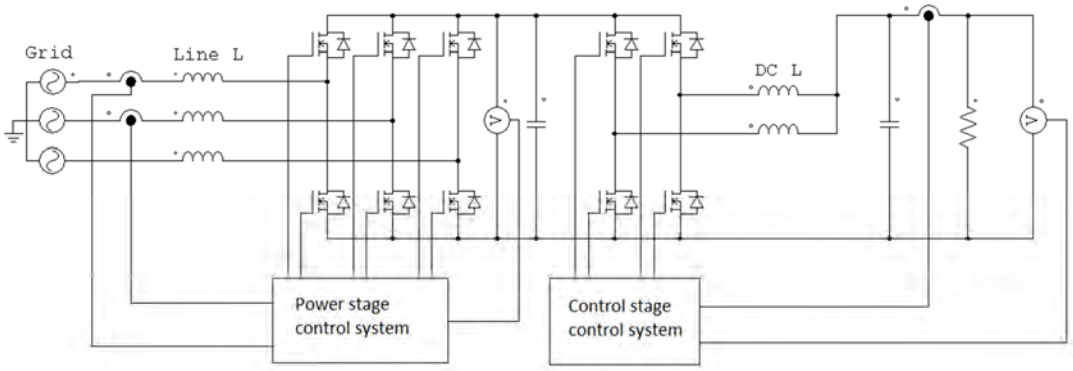

Figure A.1. Schematic of the fuel cell stack emulator.

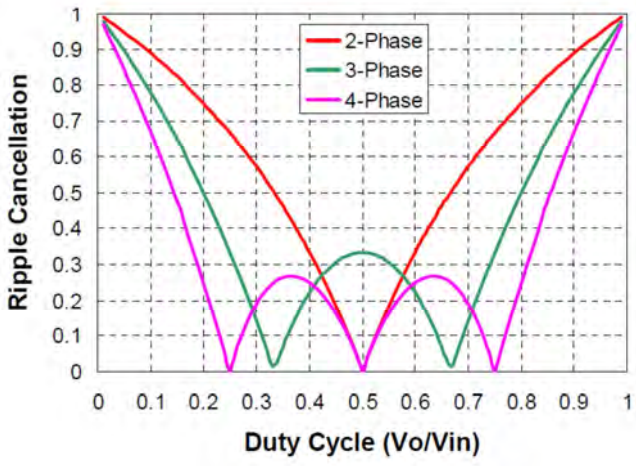

Figure A.2. Ripple cancellation in the multiphase interleaved buck [7].

The power stage converter ensures that the DC link is kept constant at twice the output voltage to ensure that the control stage converter is operating at 50% duty ratio during steady state conditions.

Since the size of the output filter components determine the transient response, the components were designed to be as small as possible to ensure rapid dynamics and to meet

the system specifications. By making use of the ripple cancelation factor of the multiphase converter, the size of the output filter components can be reduced without compromising the quality of the output. This reduction in filter size reduces losses, cost, and improves the ability to emulate transient behaviour.

A.3 Experimental Setup

The experimental setup of the grid tied stack level emulator is shown in Fig. A.3. The model and control systems were loaded onto the DSP of the dSpace 1104 system for real time implementation. Further detail regarding the implementation of the experimental setup, control systems and system performance can be found in [5].

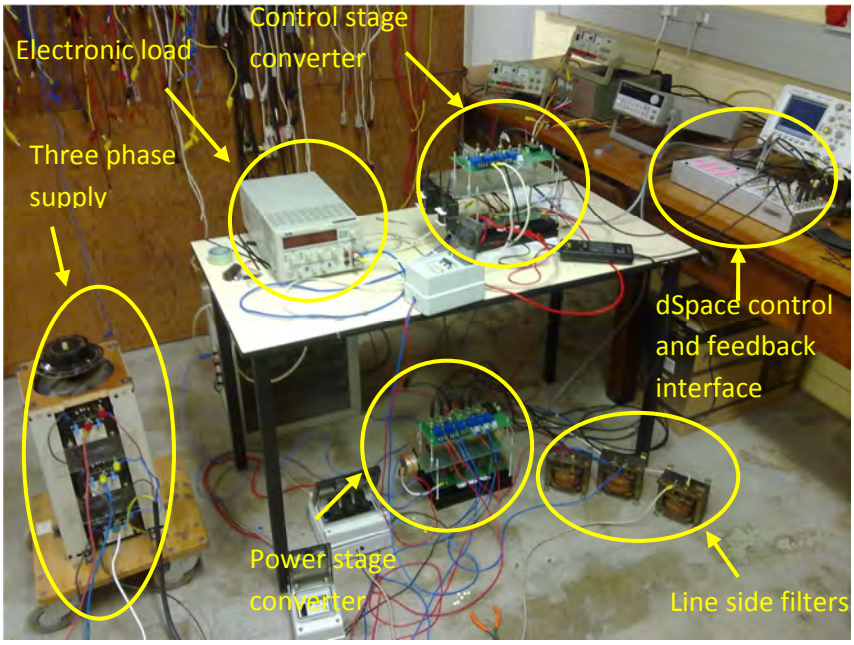

Figure A.3. Experimental setup of the stack emulator system.

A.4 Results and Discussion

The stack emulator was used to reproduce the steady state and transient responses of the LT-PEM fuel cell model. Good correlation between the model and the emulator response were obtained. The difference between the captured output voltage and the model is due to small parameter variations that occurred during testing.

As discussed in section 7.2, formation of liquid water and the resulting flooding effect

can have a large impact on cell performance. Fig. A.4 presents the emulated polarization curves, normalized to single cell level, with variable degrees of flooding compared to a curve where the stack is operating normally. It can be seen that the system performance is affected at high current densities where the internal water generation rate is much greater [1]. At very high current densities the reactant transport rate is greatly reduced as a result of the flooding where the generation of water exceeds the removal.

If the polarization curve is recorded for both increasing and decreasing current densities, a hysteresis effect can sometimes be observed. This may be as a result of flooding or drying of the membrane at either the cathode or the anode side [8]. As can be seen from Fig. A.5, polarization curve hysteresis was obtained for the flooding of the anode for both the model and the emulator and corresponds well with the experimental curve presented in Fig. 7.2.

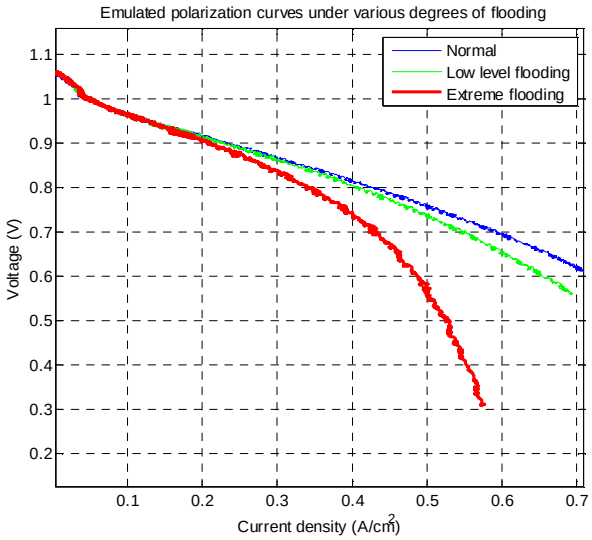

Figure A.4. Polarization curves with variable degrees of flooding.

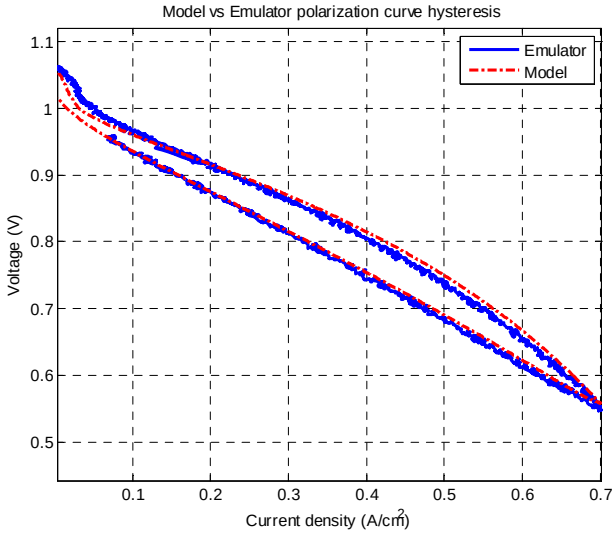

Figure A.5. Polarization curve hysteresis.

The fuel cell behaviour was simulated for a constant load of 30A or 300mA/cm^2. The actual and apparent cell current densities are shown in Fig. A.6. The anode purge events and water mass accumulation are indicated in the figure. The current density of the cells will increase as the liquid water starts to restrict the active area. The relationship between the liquid water mass and fuel cell active area is described by (a.4). It is assumed that the formation of the water layer is linear. The purge events effectively clears the water mass build-up in the channel and results in the apparent and actual cell current densities to be equal in magnitude.

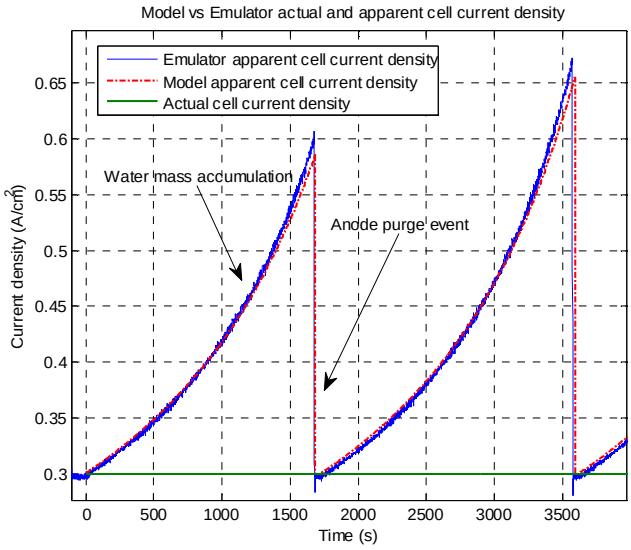

Figure A.6. Actual and apparent cell current.

The resulting output voltage response of a single cell for the constant load current is shown in Fig. A.7. The non-linear voltage decay is clearly visible. The purging event results in a recovery of the cell output voltage that will correspond to the specific operating point on the polarization curve of a healthy cell. The voltage is, however, not maintained as flooding in the anode starts to occur again, resulting in the voltage decay. The results obtained from the model and emulator corresponds to that obtained from experimental systems in literature [1]-[4], and confirms the accuracy of the simplified model when compared to those that are more complex. The temperature of the coolant leaving the fuel cell is shown in Fig. A.8. The flooding of the cell results in an increase in temperature and thermal losses. Once the anode is purged, the temperature drops where after it will start to increase as flooding occurs again.

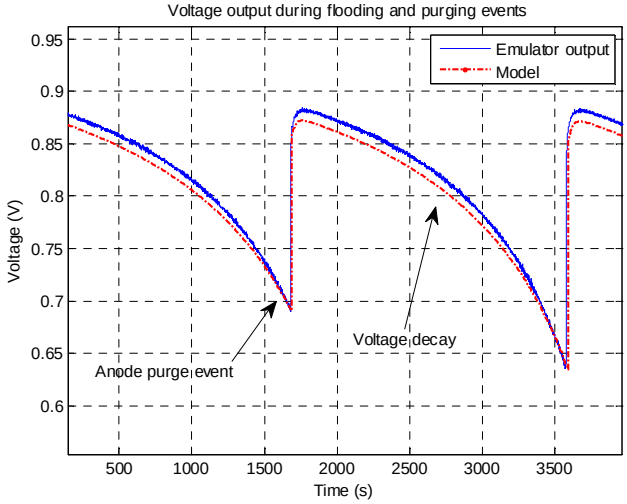

Figure A.7. Output voltage during anode flooding and purging.

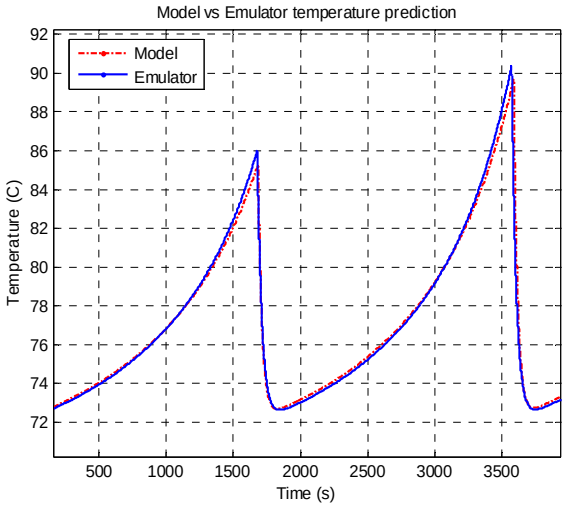

Figure A.8. Coolant temperature.

Conclusion

It is the objective of this appendix to present an approach for emulation of fuel cell characteristics under both normal and fault conditions with specific attention to flooding behaviour. The polarization curves under different degrees of flooding, voltage degradation during liquid water mass build-up as well as the resulting coolant temperature changes is presented. An emulator platform is briefly described that was able to emulate the behaviour of the fuel cell as predicted by the model. The experimental results obtained from the emulator during validation and testing for fuel cell flooding is presented and corresponds well to the results in literature for experimental fuel cells under flooding conditions. The voltage decay during water mass build-up and the recovery during purging were successfully reproduced by using input parameters for the model that correspond to the actual operating conditions of a flooding fuel cell. This system will contribute to the development of control philosophies and power conditioning hardware, which will be able to mitigate the fuel cell fault conditions, without the use of the actual fuel cell systems.

References

[1] Hui Li et al., "A review of water flooding issues in the proton exchange membrane fuel cell", *Journal of Power Sources*, Vol. 178, Jan 2008.

[2] N. Yousfi-Steiner et al., "A review on PEM voltage degradation associated with water management: Impacts, influent factors and characterization", *Journal of Power Sources,* Vol. 183, April 2008.

[3] J.T. Pukrushpan, Modeling and control of fuel cell systems and fuel processors, Ph.D. Thesis, University of Michigan, 2003.

[4] D.A. McKay, J.B. Siegel, W. Ott and A.G. Stefanopoulou, "Parameterization and prediction of temporal fuel cell voltage behavior during flooding and drying conditions" *Journal of Power Sources*, Vol. 178, Jan 2008.

[5] C. de Beer, P.S. Barendse and M.A. Khan, "Development of an HT PEM Fuel Cell Emulator Using a Multiphase Interleaved DC–DC Converter Topology," Power Electronics, IEEE Transactions on, vol.28, no.3, pp.1120-1131, March 2013.

[6] Yi-Chung Wang and Ying-Yu Tzou, Design and Realization of a Digital Multiphase-Interleaved VRM Controller Using FPGA, *The 33rd Annual Conference of the IEEE Industrial Electronics Society (IECON),* Nov. 5-8, 2007, Taipei, Taiwan.

[7] Yang Qiu, High-Frequency Modeling and Analyses for Buck and Multiphase Buck Converters, Ph.D. Thesis, Virginia Polytechnic Institute and State University, 2005.

[8] F. Barbir, PEM Fuel Cells – Theory and Practice, Elsevier Academic Press, 2004.